PLANAR STRUCTURES FOR TWO-COLOR, SINGLE-BEAM MAGNETO-OPTICAL TRAPS

Von der Quest-Leibniz-Forschungsschule
der Gottfried Wilhelm Leibniz Universität Hannover
zur Erlangung des Grades

DOKTOR DER NATURWISSENSCHAFTEN
DR. RER. NAT.

Genehmigte Dissertation

M. SC. SASKIA BONDZA

2023

Saskia Bondza: *Planar Structures for Two-color, Single-Beam Magneto-Optical Traps*

REFERENT:
PD Dr. rer. nat. Christian Lisdat
KORREFERENT:
Prof. Dr. rer. nat. Piet Schmidt
Prof. Stephan Schiller, PhD

ORT:
Hannover

TAG DER PROMOTION:
24.02.2023

To my parents.

ACKNOWLEDGEMENTS

I would not be writing this thesis without the support and guidance of a number of people throughout the years.

Firstly, I would like to thank the Hector-Seminar e.V. for the great opportunity to get to know science outside of the classroom at my high school and gain first insights into research. These experiences as well as the opportunity to participate in the National Youth Science Forum in Canberra in 2013 is what initially got me excited about research and curious about science.

Throughout my university studies I was then fortunate to have a number of great teachers and I would particularly like to thank Lars Rippe for encouraging me, teaching me and always taking the time to discuss physics with me with an enthusiasm that was truly infectious. I probably would not have started a PhD without your guidance.

Which brings me to this thesis itself and all the people that supported me along the way at PTB. I would like to thank Christian Lisdat for his guidance and his support, especially during the last year of my thesis, and Tobias for teaching me patiently when I had just started and everything was new to me, and Sören for proofreading my thesis.

Special thanks also to my desk neighbors Ben, Roman, Kilian and Sören for your support and making work as fun as it was. A big thank you also to Sofia for your advice and support, Ingo for answering many of my questions as well as the rest of the 4.32 group and the HITec group - it was a pleasure working with all of you.

I would further like to thank Stephan Metschke and his team, Stefanie Kroker and Kathrin Störr and the rest of the clean room team for the great collaboration.

Lastly, I would like to thank my family for always being my biggest support, especially my parents and my partner.

ABSTRACT

The exploration of quantum physics has heralded a new era of quantum sensors with improved measurement precision compared to conventional systems. Quantum sensors based on alkaline-earth atoms offer a particular high accuracy and improvement in comparison to classic sensors. Laboratory based experiments are rapidly transitioning to field applicable quantum sensors and have also seen a beginning commercialization. To facilitate this transition, a reduction of size, weight and power consumption in the form of miniaturization of key components such as the magneto-optical trap is necessary.

In this work, I present design and characterization of two planar structures for cooling on a broad-line and a narrow-line transition at two different wavelengths with a single, incident bi-chromatic beam.

The first is a two-color grating magneto-optical trap (GMOT) optimized for cooling and trapping of ^{88}Sr atoms on the first and second cooling transition. Secondly, a quasi-planar, achromatic Fresnel structure for magneto-optical trapping combining the advantages of achromaticity of the tetrahedral MOT with robustness, small size and ample optical access of the GMOT is presented.

In the GMOT, 10^6 ^{88}Sr atoms are initially cooled on the $^1S_0 \rightarrow {}^1P_1$ transition at 461 nm to few mK and subsequently transferred to the second cooling stage on the narrow line $^1S_0 \rightarrow {}^3P_1$ transition at 689 nm where they are further cooled to a temperature of $< 5\,\mu$K. A transfer efficiency of 25% is reached. I outline general design considerations for two-color cooling with a GMOT on a broad and narrow transition transferable to other atom species.

In the so-called Fresnel MOT a comparable number of ^{88}Sr were precooled on the $^1S_0 \rightarrow {}^1P_1$ transition and subsequently cooled on the $^1S_0 \rightarrow {}^3P_1$ transition with a transfer efficiency of 50%. Here, they were further cooled in the so-called broadband MOT to temperatures of $20\,\mu\text{K} - 40\,\mu\text{K}$. Fermionic strontium was also successfully captured in the first stage MOT. Due to its achromaticity, the Fresnel MOT can be used for laser cooling of any atom where materials with suitable reflectivity are available and can further be used for even multi-species traps.

Furthermore, I analyze MOT dynamics in micro-gravity applications regarding their temperature and number density and consequences for trap design for space-borne applications.

These results enable compact, robust set-ups for multi-color MOTs paving the way for largely miniaturized physics packages in quantum sensing.

Keywords:

- cold atoms
- laser cooling, magneto-optical trap, two-color laser cooling
- transportable quantum sensors, grating MOT

CONTENTS

LIST OF FIGURES

LIST OF TABLES

ABBREVIATIONS

BB MOT	broadband magneto-optical trap
BEC	Bose-Einstein condensate
DPMA	Deutsches Patent- und Markenamt
ECDL	extended cavity diode laser
GMOT	grating magneto-optical trap
FWHM	full width at half maximum
MMOT	mirror magneto-optical trap
MOT	magneto-optical trap
NEG	nonevaporable getter pump
NIST	National Institute of Standards and Technology
PBS	polarizing beam splitter
PDH	Pound-Drever-Hall
PMOT	pyramidal magneto-optical trap
PMT	photo-multiplier tube
PTB	Physikalisch-Technische Bundesanstalt
SF MOT	single-frequency magneto-optical trap
SNR	signal to noise ratio
SWaP	size, weight, and power consumption
TOF	time of flight
TRL	technology readiness level

1

INTRODUCTION

1.1 MOTIVATION

The discovery of quantum mechanics in the early 20th century has changed the way we understand physics fundamentally, introducing concepts and ideas that were counter intuitive to our understanding of the universe. With the development of the laser in the 1960s [60] we then gained access to advanced manipulation of quantum systems such as neutral atoms. The development of laser cooling techniques soon followed the invention of the laser, providing the base for the preparation of cold atom ensembles [3, 40, 86] and already since the middle of the last century, frequency standards based on cold atoms have been developed. Typically, atoms are (initially) cooled to a temperature in the μK range corresponding to a mean velocity of few cm/s in so-called magneto-optical traps (MOTs). Due to their small kinetic energy, cold atom ensembles allow longer interrogation times and an improvement of metrological measurements by several orders of magnitude [1, 64]. This high precision along with the sensitivity of quantum systems to their external environment has opened up the field of quantum sensing [22] pushing the limits of metrology in many areas and revolutionizing the way we "se(ns)e" the world. This field has seen tremendous growth in recent years and offers exciting prospects.

At the time, the laser was referred to as "a solution seeking a problem" [23] by one of its inventors, a statement now hard to imagine as lasers have become a key tool in many areas of research and daily life

While ions are likewise widely used in the quantum sensing community and offer similar potential [22], this work focuses solely on neutral atoms

For instance, interferometry with cold atom ensembles has been employed in gravimetry [44, 82], inertial sensing with applications in navigation [34] as well as accelometry. Cold atom clouds have also been used for the detection of magnetic fields on the microscale in so-called quantum magnetometers [77, 111, 113] with applications in medical imaging. In metrology, the SI second is currently defined as the frequency separation of the ground levels in cesium with a frequency of 9192631770 Hz [9]. The representation of the SI second thus relies on accurate measurements of this frequency separation which only becomes possible with cold atoms.

Neutral atoms are also of interest in the quantum computing community. Quantum computers based on neutral atoms are also being developed, where individual atoms isolated in optical lattices to their lattice site are used as quantum gates [41, 45, 83, 94].

New generations of atomic clocks employ transitions in the visible spectral range and are therefore referred to as optical clocks using atoms like ytterbium or strontium. State-of-the art optical clocks using neutral atoms offer a systematic uncertainty in the $< 2 \times 10^{-18}$ range [15, 18, 69, 74]. As a result, a possible redefinition of the SI second is expected to base upon optical transitions [69, 90]. These clocks also find applications in geodesy where a systematic uncertainty below the 10^{-18} level enables a resolution of the potential difference equal to a geometric height difference of $< 1\,\mathrm{cm}$ [39, 68, 104]. Furthermore, a new vacuum standard based on quantum sensing with cold atoms has been proposed [24, 96].

Due to their high precision and this vast range of applications, cold-atom-based quantum sensors have seen a beginning transition from the lab to field-based applications [30, 39, 54, 79] and early stages of commercialization [70] – a transition necessary for quantum sensors to reach their full potential to revolutionize sensing. However, these systems traditionally struggle with physics package size, weight and power consumption (SWaP) as well as complexity [64]. A large effort has thus been placed on the development of new technology to tackle these issues and the development of compact cold-neutral-atom based quantum sensors [14, 63, 64, 70, 93].

Commonly, quantum sensors use alkaline atoms with one valence electron or alkaline-earth-like atoms with two valence electrons. Alkaline atoms have an S ground state ($L = 0$) and several allowed transitions including the well-known D lines. Typically, all relevant states are spin doublet states ($S = 1/2$) so that sub-Doppler cooling mechanisms are present and temperatures in the μK range are typically reached with cooling on a single broad transition. This, among other things, makes them easy to handle experimentally. As a result, tremendous progress has been made in recent years for alkaline atom based sensors regarding compact, transportable set-ups. To highlight a few examples, quantum gravimeters and accelerometers based on rubidium are now commercially available. In 2016, the Bouyer group demonstrated first inertial measurements with a cold atom sensor on board an airplane [6]. In 2017, the first space-borne atom interferometry experiments with ^{87}Rb Bose-Einstein-Condenstates (BEC) were conducted on board a sounding rocket as part of the MAIUS-1 mission [8]. Atom interferometry experiments are based on atoms in free-fall with very cold BEC atom ensembles. Due to their very low expansion rate, the sensitivity of atom interferometers is limited by the free-fall time under normal gravitation. Micro-gravity environments support largely extended free-fall times so that one can fully profit from the low expansion rate allowing an immensely improved sensitivity to e.g. inertial forces [47]. Follow-up missions to MAIUS-1 [5] as well as the ISS mission BECCAL for a multi-purpose user facility [7] are in preparation. Vast progress has also been made in reducing the SWaP of optical clocks, and first demonstrators of rubidium clocks for satellite missions have been developed [63].

Alkaline atoms however lack the ultra-narrow transition present in alkaline-earth-like atoms thanks to their more complex level structure. The total spin number of alkaline-earth-like atoms can be $S{=}0, 1$ and an ultra-narrow transition is present between the singlet ($S{=}0$) and triplet ($S{=}1$) state offering the potential to further improve accuracy [43, 59]. Unlike in alkaline-atoms, the ground state is spin-less so that no sub-Doppler cooling processes are available for isotopes with no nuclear spin. To reach temperatures in the low μK range, a cooling scheme with two cooling stages is thus commonly employed where atoms are initially captured and pre-cooled on the strong dipole-allowed $^1S_0 \rightarrow {}^1P_1$ transition providing a good capture velocity and then further cooled with the narrow intercombination transition $^1S_0 \rightarrow {}^3P_1$. Consequently, an increased experimental effort and more complex set-ups are necessary to cool alkaline-earth-like atoms. Additional an increased effort is also necessary in order to take full advantage of the accuracy the ultra-narrow transition offers e.g in the form of ultra-stable interrogation lasers. Thus, increased accuracy does come at a price. As a result, the technology readiness level (TRL) of such sensors lags behind their alkaline-atom counterparts. Thus, an increased, continued effort in technology development and miniaturization has been made in order to make quantum sensors based on cold alkaline-earth-like atoms readily available for real-world applications. Correspondingly, a lot of progress has been made in this field in recent years as well. For instance, several transportable optical lattice clocks based on strontium atoms have been developed by the Physikalisch-Technische Bundesanstalt (PTB) and Prof. Katori's group at the RIKEN institute in Japan. Furthermore, a first demonstrator of an optical lattice clock for space-borne applications has been developed [13, 80]. The Ludlow group at the National Institute of Standards and Technology (NIST) has made significant progress towards a transportable optical lattice clock based on ytterbium [31].

Energy levels are denoted in the notation $^{2S+1}L_J$ [33]

Miniaturization of integral parts of quantum sensing experiments such as the MOT is vital for further progress in the development of compact quantum sensors. A single-beam trap with one incident beam and a planar optical element producing the additional beams necessary for trapping constitutes the highest level of miniaturization. Such a set-up reduces complexity significantly and combines robustness and enhanced optical access. One solution, first introduced by McGilligan et al. [66, 67], has proven particularly successful and shown great potential: Here, a nano-structured chip generates multiple diffracted beams from a single incoming beam, all of which then form a so-called grating magneto-optical trap (GMOT) [4, 67, 75, 110]. To date, however, this technology has been limited to the use of one cooling stage on a relatively broad transition as common for alkaline atoms. For alkali-atoms, sub-Doppler cooling in GMOTs to μK temperature has been demonstrated. In contrast, alkaline-earth-like-atom-based quantum sensors require GMOT chips that allow dual-wavelength operation to reach μK temperatures. The design of such GMOT chips has several inherent challenges and is not trivial.

In this work, I discuss the challenges of a two-color grating magneto-optical trap and present the design and characterization of such a trap. I further present a second achromatic design which is based on a periodic mirror structure. We have patented this design [11] and commonly refer to it as Fresnel MOT. The work is structured as follows: Firstly, I briefly introduce the relevant properties of strontium, the element I worked with, in the context of quantum sensing. Next, I discuss magneto-optical trapping in different geometries. In chapter 2 I review key characteristics of magneto-optical trapping in a single-beam geometries in comparison to the standard six-beam geometry with an emphasis on narrow-line cooling in non-trivial geometries. Chapter 3 introduces the test set-up used for trap characterization. With these consideration I will then discuss the design and the characterization of the Fresnel MOT in chapter 4. This is contrasted by the design and characterization of a grating for two-color magneto-optical trapping in chapter 5. Lastly, magneto-optical trapping in micro-gravity applications is discussed in chapter 6.

1.2 STRONTIUM AS QUANTUM SENSING ATOM

Out of the alkaline-earth-like atoms, strontium offers a particularly beneficial level structure with 1st and 2nd stage cooling transitions and an ultra-narrow clock transition all in the visible range that can be accessed by relatively cheap, commercially available diode laser systems. This allows for compact set-ups with a low power consumption. Additionally, the intercombination transition has an almost ideal linewidth as it is broad enough to counteract gravity and narrow enough to cool to temperatures of $< 1\,\mu\mathrm{K}$.

Strontium has four stable, naturally occurring isotopes. Due to its large abundance, ^{88}Sr is the bosonic isotope most commonly used in laser cooling experiments. An overview of the relevant transitions for ^{88}Sr is given in Fig. 1. The properties of key transitions for ^{88}Sr are listed in Tab. 1. The $^1S_0 \rightarrow {}^1P_1$ transition used for initial capturing and cooling of the atoms lies in the blue at a wavelength of $461\,\mathrm{nm}$ and a linewidth of $30.5\,\mathrm{MHz}$. Typical capture velocities are $50 - 100\,\mathrm{m/s}$. The transition rate of the $^1S_0 \rightarrow {}^3P_1$ is $7.4\,\mathrm{kHz}$ and the transition lies at a wavelength of $689\,\mathrm{nm}$. As temperatures reached after first stage cooling are typically $\approx 1\,\mathrm{mK}$ corresponding to a Doppler shift on the scale of MHz. The laser for 2nd stage cooling is thus commonly modulated and broadened initially to several MHz in order to ensure a good transfer efficiency. This is referred to as the broadband MOT (BB MOT). In the single-frequency, narrow-line MOT (SF MOT) the atoms are then cooled to $< 1\,\mu\mathrm{K}$.

The transition from the ground state $^1S_0$ to the $^3P_0$ state is known as the clock transition in strontium. For bosonic isotopes, single-photon transitions are completely forbidden by angular momentum conservation as it is a $J = 0 \rightarrow J = 0$ transition. Instead, the transition is only allowed via an E1M1 two-photon process with a lifetime of

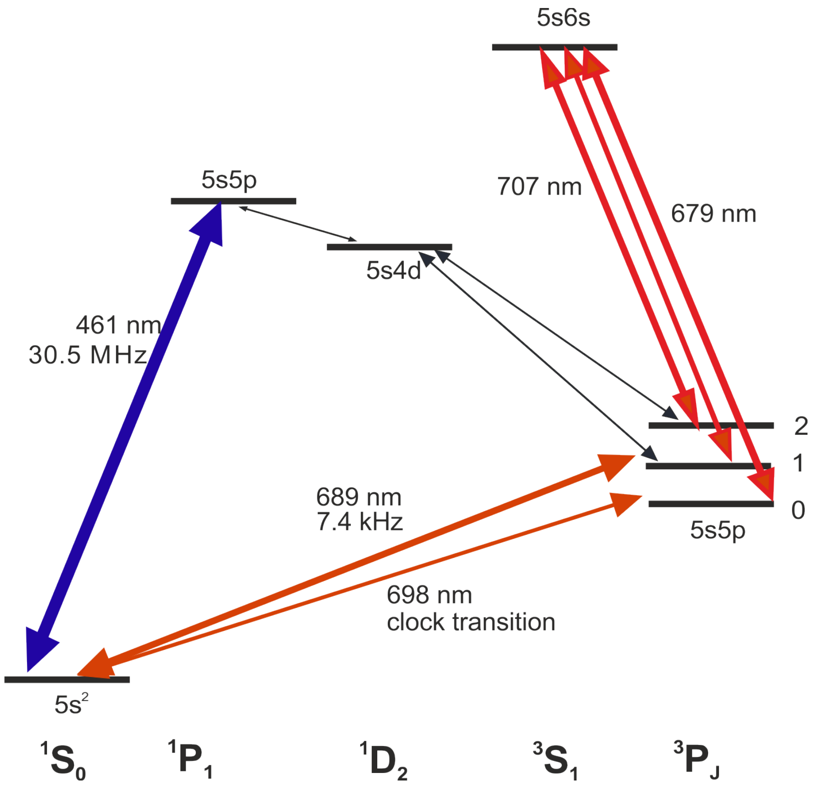

Figure 1: Energy level diagram of atomic strontium showing relevant transitions for laser cooling for this work. Wavelength and linewidth of the transitions is given. An overview of relevant properties is also given in Table 1.

PROPERTY	1^{st} STAGE COOLING TRANSITION	2^{nd} STAGE COOLING TRANSITION
Transition	$^1S_0 \rightarrow {}^1P_1$	$^1S_0 \rightarrow {}^3P_1$
Frequency ν	650.503226 THz	434.8289942 THz
Wavelength λ	461 nm	689 nm
Linewidth $\Gamma/2\pi$	30.5 MHz	7.4 kHz
Saturation Intensity I_{sat}	$41\,\mathrm{mW} \cdot \mathrm{cm}^{-2}$	$2.95\,\mu\mathrm{W} \cdot \mathrm{cm}^{-2}$
Maximal acceleration a_{max}	$9.44 \cdot 10^5\,\mathrm{m/s^2}$	$153\,\mathrm{m/s^2}$

Table 1: Properties of the commonly used broad-line 1^{st} and narrow-line 2^{nd} cooling stage transitions in ^{88}Sr.

$\approx$ 1000 years [95]. However, the transition can be enabled by applying a strong magnetic field [81, 102]. For the fermionic isotope with nuclear spin $I = 9/2$, hyperfine interaction results in an additional state mixing of the clock state with the $^3P_1$, $^3P_2$ and $^1P_1$ state [17]. As a result, electrons can decay from the clock state to the ground state by a weak electric dipole transition. The clock transition has a transition rate in the mHz range for fermionic strontium and lies at a wavelength of 698 nm. The fermionic isotope ^{87}Sr is thus also of large interest for quantum sensing. While sub-Doppler cooling has been demonstrated for fermionic strontium, the resulting temperature was still two order of magnitude above temperatures reached with two-stage cooling [115]. Consequently, two-stage cooling is commonly applied for all Sr isotopes to reach temperatures in the low µK range.

As the name suggests, the so-called clock transition exhibits properties making it ideal for the operation of an optical clock on this transition. Two important criteria of suitability of an atomic transition as optical frequency standard are a narrow linewidth and a low sensitivity to external perturbations. The clock transition in fermionic strontium is ultra-narrow while not being too narrow and has a relatively low sensitivity to most of the relevant perturbations like optical radiation and magnetic fields [58]. The two main criteria for the evaluation of the performance of an optical clock are instability and uncertainty. The most precise optical lattice clocks to date are based on ytterbium or strontium atoms. Several high-performing strontium optical lattice clocks have been demonstrated around the world with state-of-the-art clocks reaching uncertainties of 10^{-18} and instabilities of $< 10^{-16}/\sqrt{\tau}$ [78, 98, 99]. Strontium clocks so far have the edge

when it comes to compact, transportable neutral-atom-based systems. The transportable clocks based on strontium by the PTB group and Katori group [38, 103] are both have successfully completed measurement campaigns outside the lab environment [39, 79, 84].
Beyond the use in optical lattice clocks, strontium also shows great potential as quantum sensing atom in atom interferometers. For tests of gravity with cold atom interferometers, ^{88}Sr offers a combination of features that are beneficial such as a ground state with no magnetic momentum and a small collisional cross-section as well as efficient and fast cooling down to a BEC [105]. Furthermore, atom interferometers based on strontium show immense potential due to the virtual infinite lifetime of the $^3P_0$ state in bosonic Strontium [43]. They have been proposed for gravitational wave detection [37, 119], test of fundamental physics at the border of quantum mechanics and general relativity [62], tests of the weak equivalence principle [92], and search for dark matter [35].
With its proven track record as excellent candidate for quantum sensing and its convenient level structure, strontium is thus a good choice for our quest for a two-color, planar, magneto-optical trap. This work focuses on trap design for ^{88}Sr. However, many considerations are transferable to other atom species. Furthermore, special considerations for fermionic strontium will also be discussed.

1.3 EVOLUTION OF MAGNETO-OPTICAL TRAPS

To give a frame of reference for this work, I will detail the developments preceding the research presented here and discuss the different MOT designs developed through the years.

SIX-BEAM MOT Magneto-optical trapping was pioneered in 1987 by Raab et al. [86] using three pairs of counter-propagating beams in combination with a quadropole field produced by a pair of coils in anti-Helmholtz configuration to confine and cool sodium atoms. Here, the beams propagate along the symmetry axis of the quadropole field and atoms are trapped and cooled at the magnetic field minimum. The beam pair propagating perpendicular to the magnetic field coils has the opposite handedness as the beams in the plane parallel to the magnetic field coils. This geometry is depicted in Fig. 2 Commonly, the six-beam MOT is realized with three incident beams that are retro-reflected where a quarter waveplate is placed in front of the mirror to ensure correct polarization.

MIRROR MOT The so-called mirror MOT (MMOT) is a design beneficial for applications that benefit from trapped atoms close to a substrate surface [32, 112]. Here, the number of incident beams is re-

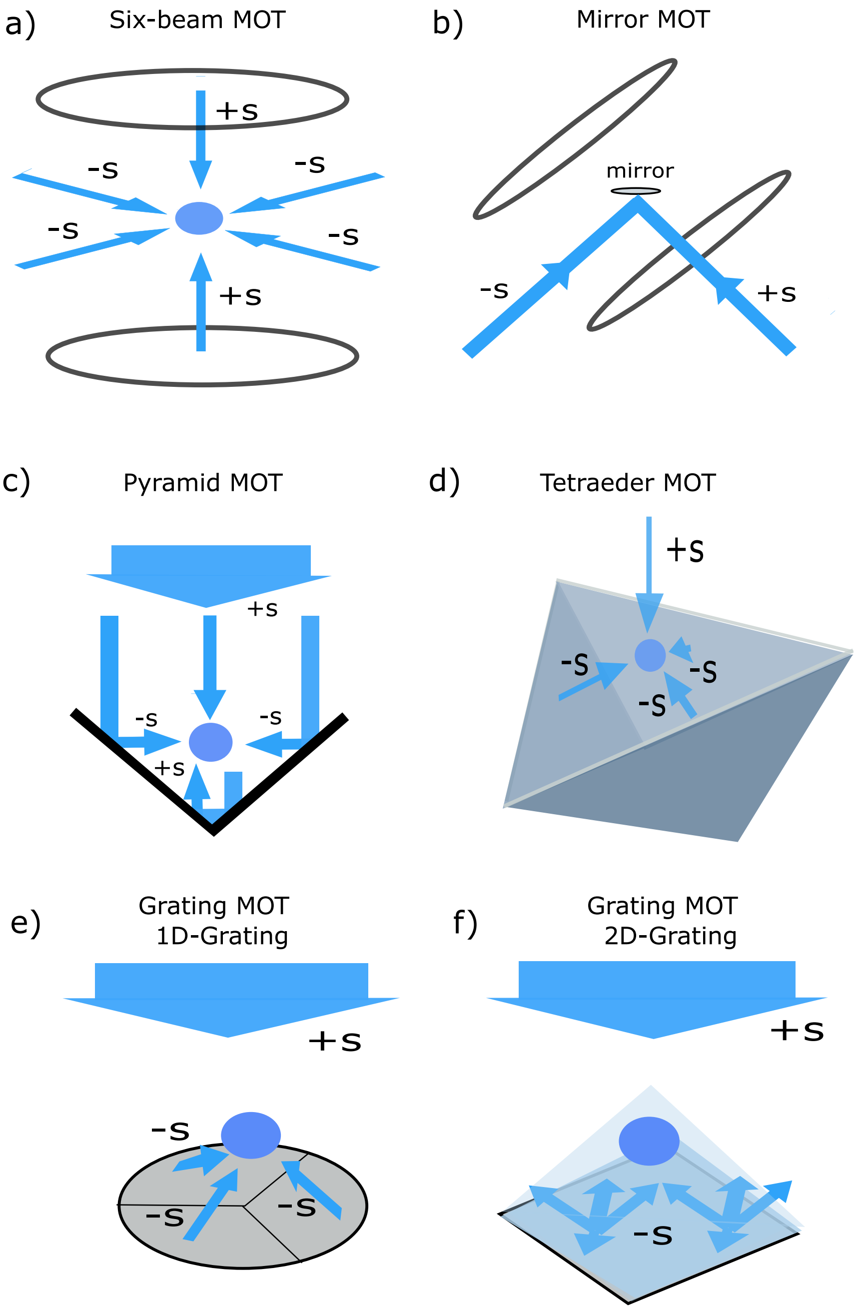

Figure 2: Different MOT geometries for trapping and cooling of neutral atoms. MOT coils are ommitted for clarity in c), d), e) and f). a) Standard 6-beam geometry b) Mirror MOT consisting of four laser beams. Two laser beams are reflected by an in-vacuum mirror with an additional pair of couterpropagating beams intersecting the overlap volume to allow trapping in three dimensions. Handedness is equivalent to the standard six-beam geometry. c) Pyramid MOT where a single incident beam is used and secondary beams are reflected in a 90° angle. Handedness is equivalent to the standard six-beam geometry. d) Tetraeder MOT designed by Vangeleyn et. al. [109] with part of the overlap volume outside the mirror volume. Four instead of six beams form the MOT with the secondary beams forming an oblique angle with the symmetry axis of the magnetic field. e) Planar, nanofabricated grating magneto-optical trap with diffraction in one dimension f) GMOT where light is diffracted in two directions forming a pyramidal overlap volume above the chip.

duced to four with two of the incident beams reflected by a reflecting substrate surface under a 45° angle. The quadropole field is then typically oriented along one of the reflected beams to ensure handedness of the beams corresponding to the standard six-beam configuration [88] as depicted in Fig. 2 b). Compared to the latter, the MMOT has a reduced overlap volume (i.e. the volume where light from all beams is present and the intensity-weighted wave-vectors add to zero) by 1/2 given beams with the same beam diameter [64]. It further forms few mm from the substrate surface. While the quadropole field can be produced by a U-wire etched on the substrate surface instead of standard magnetic field coils [88], the MMOT overall offers little potential for a reduced SWaP as the geometry of the laser beams limits possible miniaturization. Its main purpose is thus for applications where cold atoms near a substrate surface are required.

PYRAMID MOT A design that offers a significant improvement in SWaP is the pyramid MOT (PMOT) first demonstrated by Lee et al. in 1996 [50]. Here, a hollow PMOT configuration consisting of a combination of mirror pairs into pyramidal shape is employed. Each pair of mirrors reflects the incident beam in a right angle each thus replacing the quarter wave-plate and retro-reflecting mirror used in the six-beam configuration. The combination of such mirrors into a pyramidal shape allowed to produce three sets of counter-propagating beams in a new way using a single incident beam. This geometry is depicted in Fig. 2 c). An additional advantage is that given a circular polarized input beam with the correct handedness, all other beams will also have the right polarization and wave-vectors necessary for MOT formation – a feat that can be more challenging to achieve in the standard six-beam configuration with more tedious alignment.
However, the PMOT also has its disadvantages. The overlap volume V is six times smaller than in a standard six-beam MOT with the same incident beam waists. Furthermore, the overlap volume within the hollow pyramid offers no optical access in the radial plane thus making further manipulation as well as detection and imaging challenging. This is further complicated by scattered light from the mirror structures and reflected MOT images. A hexagonal design with a central MOT retro-reflector using the principle of total internal reflection improves upon this and was demonstrated in 2019 by Bowden et al. [16]. While optical access is still limited in this design, there are three radial axes that offer optical access to the atom cloud. Their set-up further combined the pyramidal MOT with a cavity to form an optical lattice thus providing a platform for the operation of an optical lattice clock. Indeed, the PMOT has been implemented in a number of cold atom experiments including atom interferometers for gravimetry measurements [10] and cold atom flux sources [87] in addition to optical clocks.

Micro-fabricated PMOTs etched on a silicon wafer have further been demonstrated for use as integrated optics on an atom chip and present another significant step in reduction of SWaP [85, 107]. However, the number of atoms captured is limited due to the small overlap volume with $N \propto V^2$ and only a few thousand atoms are captured [85], which is not sufficient for many applications. Additionally, imaging and detection becomes challenging with the problems from the macroscopic PMOT enhanced in the micro-fabricated PMOT [85] and the manufacturing process is complex and costly with limitations on apex angle.

TETRAEDER MOT In 2009 Vangeleyn et al. demonstrated their so-called tetrahedral MOT where trapping is achieved with four laser beams, the minimum number of beams necessary for confinement in three dimensions [109]. Here, three mirrors are used to produce three reflected beams with tetrahedral angle to one another as well as the incident beam as depicted in Fig. 2 d). This approach extends the overlap volume of the beams above the mirrors offering improved optical access and easier manipulation. As a result, the mirrors can be placed outside of the vacuum chamber to facilitate alignment. However, careful assembly of the mirrors and alignment is still necessary. While the tetraeder geometry offers particularly beneficial properties due to its inherent symmetry [108], generally an inclination angle ϕ of the mirrors deviating from tetraeder geometry can also be chosen. The condition to achieve a balanced radiation pressure for optical molasses i.e. intensity balance is then given for a reflectivity $R = \frac{1}{3\cos(2\phi)}$. In the tetraeder geometry, with $\phi = 35.3°$, the condition for intensity balance yields a reflectivity of 1.
As the reflected beams form an oblique angle with the symmetry axis of the quadropole field, the physics of magneto-optical trapping is changed drastically. We will examine this in the following sections and discuss the theory of such non-trivial single-beam geometries in detail.

GRATING MOT Aided by the advances in nanotechnology, non-trivial single beam geometries as in the tetraeder MOT were then realized with nano-fabricated grating chips. A key difference to the previous presented techniques is that the secondary beams are no longer produced via reflection. Instead, the grating chips diffract the incident light under the diffraction angle θ given by the Bragg condition $m\lambda = d\sin(\theta)$ where m denotes the diffraction order, λ the wavelength, d the grating period and θ the diffraction angle. Furthermore, diffracted light is compressed resulting in an effectively higher intensity so that $\frac{I_j}{I_0} = \epsilon\frac{1}{\cos\theta}$ where ϵ denotes the diffraction efficiency, I_0 the intensity of the incident beam and I_j the intensity of the diffracted beams. Thus, the condition for intensity balance becomes $\epsilon = \frac{1}{n}$ where n denotes the number of diffracted beams. Together with the incident beam they form the overlap volume where cooling takes place.

The first grating MOT was realized with three separate blazed grating chips each with a size of 12.7 mm × 12.7 mm [110]. The grating chips diffract the incident beam with a diameter of 23 mm under an angle of 69.4°, close to tetraeder configuration with an almost ideal diffraction efficiency $\epsilon = 32\%$. This initial implementation of a GMOT demonstrated sub-Doppler cooling of $^{87}\mathrm{Rb}$ atoms down to a temperature of 30 μK. In the standard six-beam configuration, temperatures of few μK can be reached.

Succeeding work used a single chip with three segments where the blazed grating structure is rotated by 120° between segments [21] yielding a monolithic trapping structure and further reducing the complexity and size of the set-up. Such a design is illustrated in Fig. 2 e). An alternate design uses a 2D-structure with a square array of cylindrical indentations [75] as depicted in Fig. 2 f). For such a grating the Bragg condition is given as $\sqrt{m_x^2 + m_y^2}\lambda = d\sin\theta$. It diffracts beams along the x- and y-axis of the square array. The resulting overlap volume is thus a pyramid whose footprint is given by the chip surface [75].

GMOTs are particularly appealing as they only need a single, monolithic, planar optical element and one incident laser beam to produce a configuration for atom confinement in three dimension. As such, they are particularly robust, compact and offer ample optical access. They have since been implemented in a number of experiments using alkaline atoms including atomic clocks [28], pressure sensors [4] and atom interferometers [49].

However, they have one downside: by moving from reflection to diffraction to generate the secondary beams, we give up achromaticity. As a result, use of diffraction gratings for more than one wavelength is challenging: The wavelength ratio of the broad and narrow cooling transitions in alkaline-earth-like atoms is typically about 1.5. Design of a 2D-grating providing 1st order diffraction for both wavelengths with no 2nd order diffraction present is not possible for this wavelength ratio. The large wavelength ratio further results in stark differences of the respective diffraction by a grating. As a result, intensity balance for both wavelengths is not trivially achieved. The difference in diffraction angles results in an axial shift of the overlap volume complicating transfer from the 1st to the 2nd cooling stage. Furthermore, the 0th order diffraction is typically suppressed by choosing a grating height of $\lambda/4$, a condition that can not be fulfilled for both wavelength. How these challenges can be overcome is discussed in chapter 5 of this thesis.

2

MAGNETO-OPTICAL TRAPPING IN A FOUR-BEAM GEOMETRY

Trapping in geometries with a single incident beam and secondary beams that form an oblique angle with the symmetry axis of the magnetic field is non-trivial and has surprising aspects. We will firstly review key aspects of “standard” Doppler cooling and magneto-optical trapping and establish nomenclature and terminology building a foundation for in-depth discussion of the physics at hand in more complex trapping geometries.

2.1 MAGNETO-OPTICAL TRAPPING REVISITED

2.1.1 *Doppler Cooling*

The basic idea in Doppler cooling is that momentum $\hbar\vec{k}$ is transferred from the incident laser beams to an atom in motion via photon absorption, where $\vec{k}$ is the wave vector. As a photon is absorbed, the velocity $\vec{v}$ of the atom becomes $\vec{v}+\hbar\vec{k}/M$ where M is the mass of the atom. In order for an atom to be cooled with this process, the acceleration due to absorption has to be velocity selective i.e. the atom needs to experience an overall negative acceleration for positive velocities and vice versa. An easy way to implement such velocity selectivity and break symmetry is to make use of the Doppler effect that causes a frequency shift $\vec{k}\cdot\vec{v}$ of the resonance frequency ω_r of the atomic transition used for cooling in the laboratory reference frame. Detuning the laser beams from the resonance frequency ω_r by a frequency Δ such that $\omega_r = \omega_L + \vec{k}\cdot\vec{v} = \omega_r + \Delta - kv$ results in the atom being on resonance with the laser beam that it is moving towards and being off resonance with laser beams it is moving away from. To cool the atom in three dimensions, one can then use three orthogonal pairs of counter-propagating laser beams. The total force by a single laser beam acting on an atom is given by [33]:

$$F = F_{abs} + \delta F_{abs} + F_{spont} + \delta F_{spont} \tag{1}$$

where F_{abs} denotes the force resulting from absorption of photons and F_{spont} denotes the force resulting from spontaneous emission of photons. The fluctuations of these forces are given as δF_{abs} and δF_{spont} respectively. The average of the force due to absorption corresponds to the scattering force F_{scat} and $F_{abs} = F_{scat}$. Momentum transfer due to spontaneous emission will average to zero over a sufficiently large number of scattering events as photons are emitted

isotropically in all spatial directions in a first order approximation (neglecting dipole radiation) such that $F_{spont} = 0$. For broad transitions and $|\vec{v}| >> 0$, the fluctuation can be neglected. The force acting on an atom is then given by the scattering force alone.
The scattering force $\vec{F}_{scat}$ acting on the atom by each laser beam j with intensity I_j is given as:

$$\vec{F}_{scat} = \hbar\vec{k_j}\frac{\Gamma}{2}\frac{s_j}{1 + s_{tot} + 4(\Delta - \vec{k_j} \cdot \vec{v})^2/\Gamma^2} \tag{2}$$

with $s_j = \frac{I_j}{I_{sat}}$ and $s_{tot} = \sum_{j=0}^{N} s_j$. I_{sat} denotes the saturation intensity of the transition and Γ denotes the linewidth. The resulting force of one pair of counter-propagating beams, so-called optical molasses, can then be written as:

$$F = -\alpha v \tag{3}$$

where α is the damping coefficient obtained by first order Taylor expansion of Eq. 2 for both laser beams in v around $v = 0$ which yields:

$$\alpha = 16\hbar k^2 \frac{\Delta s}{\Gamma^2(1 + s_{tot} + 4\Delta^2/\Gamma^2)^2} R \tag{4}$$

where $R = \frac{|\vec{F}_{scat}|}{|\hbar\vec{k}|}$ is the scattering rate.

2.1.2 *Doppler Temperature Limit*

The treatment above so far would allow deceleration to $v = 0$ corresponding to a temperature of 0 K as we have neglected the fluctuation terms in Eq. 1 that become important at low temperatures. Each scattering process is accompanied by a recoil kick to the atom in random direction due to the momentum transfer by spontaneous emission. We can think about this as a random walk of the velocity of the atom that leads to heating [33]. The resulting heating rate corresponds to 1/3 of the scattering rate for each spatial direction as we assume isotropic scattering. In the same way, a fluctuation in the number of photons absorbed per time interval leads to a heating rate proportional to the scattering rate for the direction of absorption - here the z-axis - near zero velocity. The temperature limit reachable with Doppler cooling in optical molasses along an axis z is given by the point where heating and cooling balances and we can write:

$$\frac{1}{2}Md\bar{v}_z^2/dt = (1 + 1/3)E_r(2R) - \alpha\bar{v}_z \overset{!}{=} 0 \tag{5}$$

where E_r denotes the recoil energy. The recoil energy is given by $1/2Mv_r^2$ where v_r is the recoil velocity which is in turn given by the change in the atom's velocity due to absorption of one photon at the transition wavelength, $v_r = \frac{\hbar k}{M}$. Using the equipartition theorem to relate temperature to kinetic energy, we obtain:

$$T_{lim} = \frac{\hbar\Gamma}{8k_B|\Delta|}\left(1 + s + 4\frac{\Delta^2}{\Gamma^2}\right) \tag{6}$$

which has a minimum at $\Delta = -\Gamma/2$ yielding the well-known Doppler cooling limit $T_D = \hbar\Gamma/2k_B$ for a pair of counter-propagating laser beams [53]. Note that this derivation relies explicitly on the geometry of the laser beams. Here namely a pair of counter-propagating laser beams.

2.1.3 *Magneto-optical Trapping*

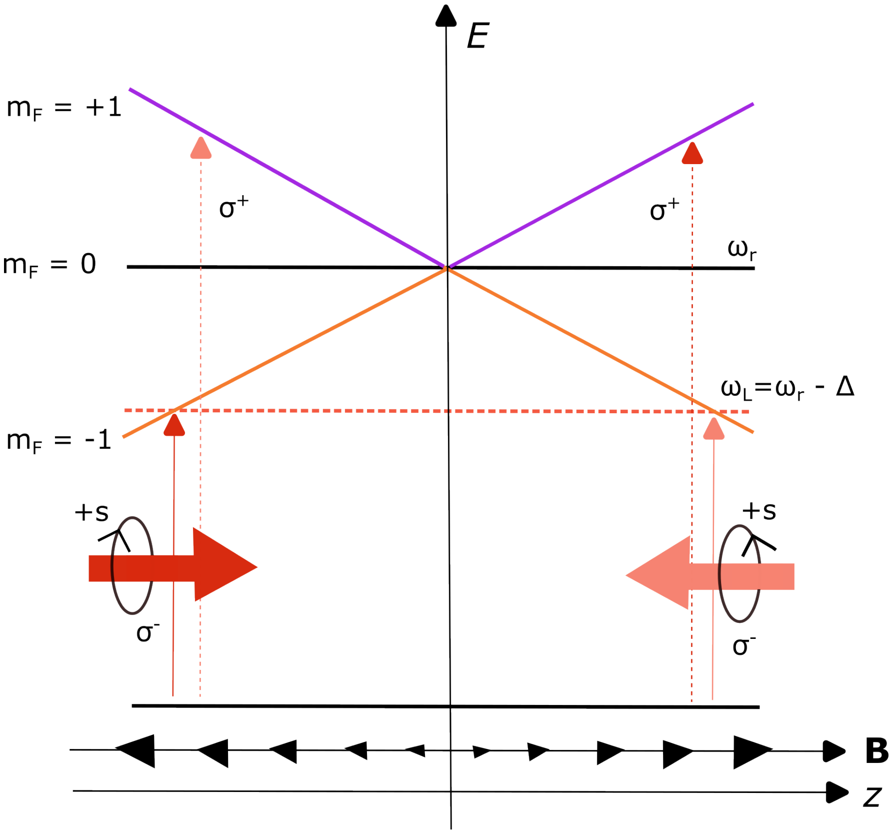

Figure 3: Principle of magneto-optical trapping in one dimension for a pair of counter-propagating beams with the frequency $\omega_L = \omega_r - \Delta$ along the z-axis where ω_r is the resonance frequency and Δ is the detuning. The k-vector of the laser beams and magnetic field vector are anti-parallel before the zero-crossing so that the +s polarization results in coupling to the σ^- ($\Delta m_F = -1$) transition. After crossing the magnetic field minimum, k-vector and magnetic field vector are aligned resulting in coupling to the off-resonant σ^+ ($\Delta m_F = +1$).

While Doppler cooling provides a velocity-dependent force cooling the atoms, optical molasses alone do not trap the atoms as they are still free to simply drift out of the optical molasses and are then lost. A position-dependent force is needed in order to confine the atoms in space. This is commonly achieved by making use of the Zeeman effect.

Let us look at the first cooling stage transition in ^{88}Sr from the $^1S_0$ state to the $^1P_1$ state that conveniently has a very simple level structure. In the presence of a magnetic field B the energy states of an atom are shifted by

$$\Delta E = g_F m_F \mu_B B \tag{7}$$

where g_F is the Landé factor, μ_B the Bohr magneton and B the magnitude of the magnetic field and m_F indicates the Zeeman sublevel. The ground state $^1S_0$ has a total angular momentum of 0 and thus does not split while the excited state $^1P_1$ has three Zeeman sublevels with $m_F = \{-1, 0, 1\}$. A quadrupole field with

$$\vec{B} = b\{x, y, -2z\} \tag{8}$$

yields constant magnetic field gradients dB_j/dx_j near the magnetic field minimum and results in a Zeeman splitting along each symmetry axis of the quadrupole field as illustrated in Fig. 3. The $m_F = -1$ state is a high-field seeker as the projection of the precession of the total angular momentum around the magnetic field is aligned with the latter. The $m_F = +1$ state is anti-aligned with the magnetic field making it a low-field seeker. Meanwhile, the angular momentum of the $m_F = 0$ state is orthogonal to the magnetic field so that it does not experience an first order energy shift in the presence of a magnetic field.

The conservation of angular momentum imposes strict selection rules on the excitation of the different Zeeman transitions with regards to the polarization of the exciting photon. The $\sigma^{\pm}$ transition $m_F = 0 \rightarrow m_F = \pm 1$, $\Delta m_F = \pm 1$ can only be excited by a photon whose spin projection along the quantization axis yields $m_S = \pm 1$. The π transition with $m_F = 0 \rightarrow m_F = 0$, $\Delta m_F = 0$ can only be excited by a photon whose spin projection along the quantisation axis yields $m_S = 0$.

We want to emphasize here that, as pointed out by Vangeleyn, σ^-, σ^+ and π are the names of transitions and do not refer to polarization of the exciting photons [108]. The easy correspondence that can be made for light propagating along the symmetry axis of the magnetic field can lead to misleading nomenclature where σ^+ and σ^- is used to refer to the polarization of the exciting photons. In this simple case of the standard six-beam MOT, we find that right circular polarized light (+s) with a wave-vector parallel to the magnetic field vector will excite the σ^+ transition, left circular polarized light (-s) with a wave vector parallel to the magnetic field vector will excite the σ^- transition while excitation of the π transition is forbidden in this configuration as it would violate the conservation of total angular momentum. For light with a wave vector that is not parallel to the magnetic field vector, excitation of the π transition is allowed for light linearly polarized along the quantization axis given by the direction of the magnetic field.

Let us now go back to Fig. 3 and discuss the trapping dynamics in one dimension for two circular polarized, counter-propagating beams. We refer to the direction of the circular polarization with respect to the propagation direction as handedness. Both beams have the same handedness (+s) and are red-detuned. For $z < 0$ the beam incident from $-z$ (dark red) has a k-vector anti-parallel to the magnetic field vector before crossing the magnetic field minimum corresponding to a spin projection of $m_S = -1$ along the quantization axis and thus exciting the σ^- transition. It will be resonant with the $m_F = -1$ Zeeman sublevel at the position where the detuning Δ corresponds to the sum of Zeeman shift and Doppler shift providing a restoring force and pushing the atom back towards the magnetic field minimum. The beam incident from +z (light red) has a k-vector parallel to the magnetic field vector and thus a spin projection $m_S = +1$ coupling to the off-resonant σ^+ transition. For $z > 0$ symmetry is reversed and the beam incident from +z will now have a a spin projection of $m_S = -1$ and be resonant with the $m_F = -1$ Zeeman sublevel, again pushing the atom back to the trap center. As a result, atoms are trapped at the position of the magnetic field minimum where excitation from each laser beam has the same probability and radiation pressure is thus balanced.

The force resulting from a single laser beam j that acts on an atom in a magneto-optical trap is given by:

$$\vec{F_j} = \hbar\vec{k}\Gamma/2 \frac{s_j}{1 + s_{tot} + 4(\Delta - \vec{k_j} \cdot v - \mu_B dB/dz\, z)^2/\Gamma^2} \tag{9}$$

One can show that cooling and trapping of an atom in a 1D MOT can be modeled by a damped harmonic oscillator and the total force is of the form [33]

$$F_{MOT} = -\alpha v - \underbrace{\frac{\alpha\beta}{k}}_{\kappa} z \tag{10}$$

with the previously derived damping coefficient α and $\beta = g_f \mu_B/\hbar dB/dz$. The first is known as cooling coefficient and is a measure how effectively atoms are slowed in the trap while κ is referred to as trapping constant and is a measure of how strongly an atom is spatially constrained. These are two key parameters in describing a magneto-optical trap.

2.2 POLARIZATION PROJECTION

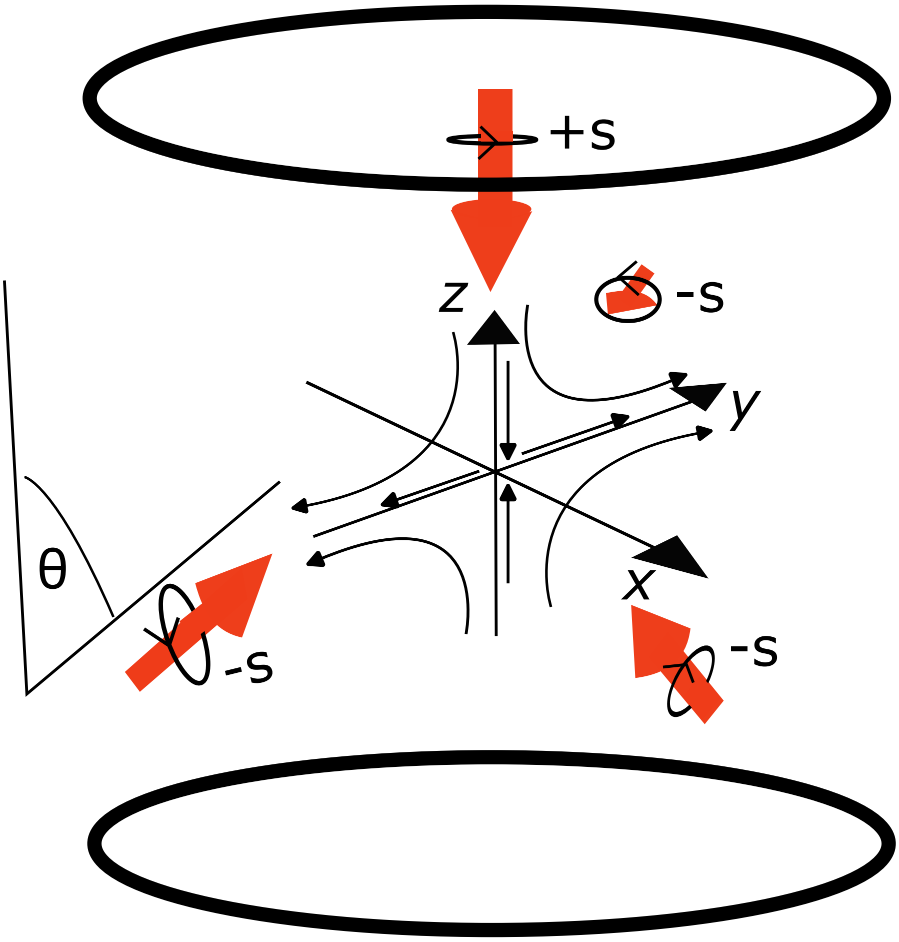

Figure 4: Illustration of the four-beam MOT configuration. A single laser beam incident along the z-axis (vertical to the magnetic field coils generating the quadrupole field) generates all laser beams necessary for cooling and trapping. The secondary beams are generated via diffraction or reflection form an oblique angle with the symmetry axis of the quadrupole field.

As we have seen previously, other beam geometries than the aforementioned beam geometry are also possible. At minimum, four beams are required to trap in three dimensions leading to non-trivial single beam-geometries. Let us consider a beam incident along the z-axis of the quadrupole field and three secondary beams intersecting the incident beam and the symmetry axis of the quadrupole field at an oblique angle θ as depicted in Fig. 4 as the case for the tetraeder MOT and gMOT. For such a secondary beam with the polarization defined along the k-vector no easy correspondence can be made with regards to excitation of the different transitions. Instead, we need to rotate the polarization vector with a Wigner-rotation matrix to the quantization axis that we have defined by the local magnetic field. For a photon with angular momentum $j = 1$ and polarization given in polar coordinates such that $[1, 0, 0]$ ($[0, 0, 1]$) defines left (right) circular polarization along the k-vector, the Wigner rotation matrix is given as:

$$\mathscr{D} = \left\{ \begin{array}{ccc} \frac{1+\cos\theta}{2} e^{-i\gamma+i\delta} & \frac{\sin\theta}{\sqrt{2}} e^{-i\gamma} & \frac{1-\cos\theta}{2} e^{-i\gamma-i\delta} \\ -\frac{\sin\theta}{\sqrt{2}} e^{i\delta} & \cos\theta & -\frac{\sin\theta}{\sqrt{2}} e^{-i\delta} \\ \frac{1-\cos\theta}{2} e^{i\gamma+i\delta} & \frac{\sin\theta}{\sqrt{2}} & \frac{1+\cos\theta}{2} e^{i\gamma-i\delta} \end{array} \right\}$$

where γ, θ, δ are the Euler angles in XYZ convention [25]. For a left circular polarized beam with $pol = [1, 0, 0]$ and intensity I_j propagating along the vector $\frac{1}{\sin^2\theta}[\sin\theta, sin\theta, cos\theta]$ with $\cos\theta = \frac{\vec{k}\cdot\vec{B_z}}{|k\cdot B|}$ and $\gamma = 0, \delta = 0$, applying the Wigner rotation matrix yields the following coupling to the $\Delta m_F = \{+1, 0, -1\}$ transitions:

$$I_{+1} = \left(\frac{1+\cos\theta}{2}\right)^2 I_j \tag{11}$$

$$I_0 = \left(\frac{\sin\theta}{\sqrt{2}}\right)^2 I_j \tag{12}$$

$$I_{-1} = \left(\frac{1-\cos\theta}{2}\right)^2 I_j \tag{13}$$

An alternative derivation that allows a more intuitive understanding was presented by Vangeleyn [108] and is illustrated in the following for completeness. Let us consider a laser beam with intensity I_j propagating along the z-axis with circular polarisation and handedness $s = \{+1, -1\}$. We can then write the normalized electric field vector of such a laser beam as

$$\vec{E_j}(z, t) = E_j \frac{1}{\sqrt{2}} \begin{bmatrix} 1 \\ e^{is\pi/2} \\ 0 \end{bmatrix} \tag{14}$$

If we now consider a beam whose k-vector forms an angle θ with the z-axis, we obtain the electric field by applying a rotation matrix:

$$\vec{E_{rot}} = \begin{bmatrix} 1 & 0 & 0 \\ 0 & \cos\theta & -\sin\theta \\ 0 & \sin\theta & \cos\theta \end{bmatrix} \tag{15}$$

The matrix multiplication $\vec{E_{rot}} \cdot \vec{E_j}(z, t)$ then yields:

$$\frac{E_j}{\sqrt{2}} \begin{bmatrix} 1 \\ e^{is\pi/2} \cos\theta \\ e^{is\pi/2} \sin\theta \end{bmatrix} \tag{16}$$

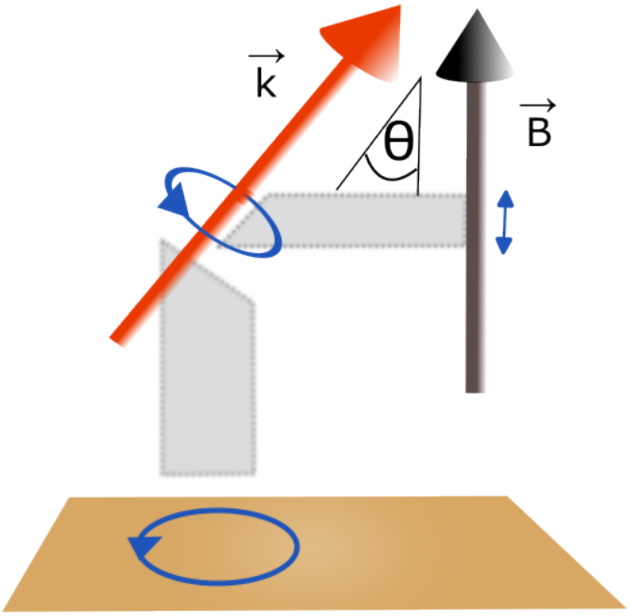

Figure 5: Illustration of polarisation projection. For photons propagating along a k-vector forming an angle with the symmetry axis of the magnetic field, the polarization projection onto the quantization axis has to be calculated which then yields coupling coefficients to the σ^+, σ^-, and π transition.

This electric field vector can now be split into a projection in the x-y-plane, orthogonal to the magnetic field vector we are considering, and a projection onto the z-axis as depicted in Fig. 5. The latter yields the coupling to the π transition where we recover equation 12. To obtain the σ^+ and σ^- coupling we need to solve the following equation:

$$E_{xy} = \frac{E_{\sigma^+}}{2} \begin{bmatrix} 1 \\ e^{i(s=1)\pi/2} \\ 0 \end{bmatrix} + \frac{E_{\sigma^-}}{2} \begin{bmatrix} 1 \\ e^{i(s=-1)\pi/2} \\ 0 \end{bmatrix} = \frac{E_j}{2} \begin{bmatrix} 1 \\ e^{is\pi/2} \cos\theta \\ 0 \end{bmatrix} \tag{17}$$

which yields $E_{\sigma^-} = \frac{1+s\cos\theta}{2} E_j$ and $E_{\sigma^+} = \frac{1-s\cos\theta}{2} E_j$, thus giving the same result as Eq. 11 and 13.

2.3 BROAD-LINE MOT

With the above derivations on coupling of circular polarized beams forming an angle with the x-, y- and z-axis of the quadrupole field, we can now express the force contribution from one such beam in a magneto-optical trap as follows:

$$\bar{F}_j = \hbar \bar{k}_j \Gamma / 2 s_j \sum_{n=-1,0,1} \frac{I_n / I_j}{1 + s_{tot} + 4 \frac{(\Delta - \bar{k}_j \cdot \bar{v} - n g_F \mu_B B)^2}{\Gamma^2}} \tag{18}$$

With this we can now calculate the forces in a non-trivial single-beam geometry and develop an understanding of the trapping dynamics. Indeed, the fact that trapping along the z-axis is possible is not obvious as the secondary beams have the exact opposite handedness than the counter-propagating beam in a standard six-beam MOT. As a result, we expect an anti-trapping force to originate.

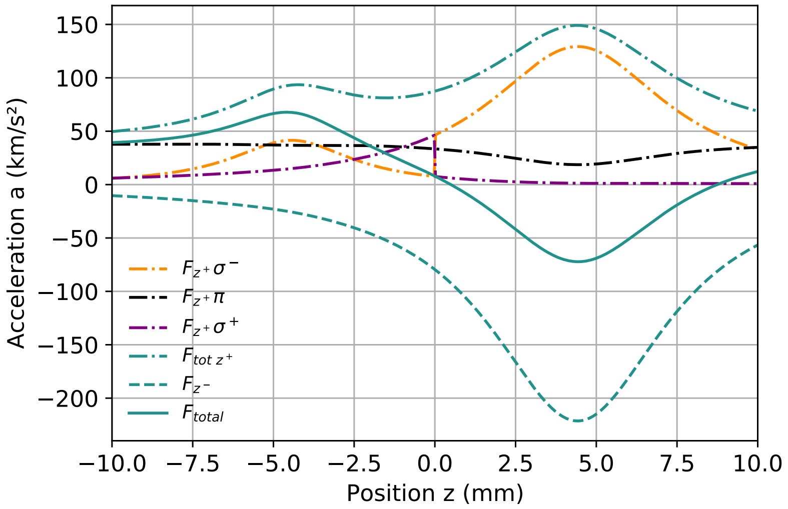

Figure 6: Illustration of axial acceleration acting on an atom at rest along the z-axis of the quadrupole field. The acceleration resulting from the incident beam with intensity $I_0 = 0.5\, I_{sat}$ is illustrated with the turqoise, dashed line and results from coupling to the σ^- transition only. The acceleration resulting from the secondary beams is indicated with the turqoise dot-dashed line. Also indicated are the contributions from coupling to the σ^- transition (orange), the π transition (black), and the σ^+ transition (purple). The total force is indicated with the turqoise, solid line. The magnetic field gradient is chosen as $dB/dz = 5\,\mathrm{mT/cm}$ and the detuning as $\Delta = -\Gamma$.

AXIAL TRAPPING Let us consider a system where an incident beam propagates along the z-axis of the quadrupole field with intensity I_0 and handedness $+s$. Three secondary beams form an angle $\theta = \arccos\left(\frac{1}{3}\right) = 70.53°$ with the incident beam. In order to balance the intensity I_0 of the incident beam, the intenisity of the secondary beams

I_j needs to fulfill $I_j = \frac{1}{N\cos\theta} I_0$ where N is the number of secondary beams. Intensity balance is characterized by the intensity-weighted wave vectors summing to 0 and a resulting zero net force in the absence of a magnetic field. This yields a symmetric beam configuration in tetraeder shape and thus proves convenient for an initial discussion. In Fig. 6, a full-force calculation for the acceleration acting on an atom at rest along the z-axis are plotted. The acceleration from the circular polarized incident beam (indicated by the turquoise, dashed line) propagating along the magnetic field direction results from coupling to the σ^- transition - as the case in the standard six-beam configuration. The forces generated by the secondary beams are split up into coupling to the σ^-, π, and σ^+ transition. As we expect, the largest contribution to the overall force from the secondary beams results from coupling to the σ^- transition for positive z-values yielding a positive acceleration pushing atoms further away from the trap center. For negative z-values, a small acceleration from excitation of the σ^- transition is still generated and is on a similar scale as the acceleration resulting from coupling to the σ^+ transition. While the latter transition is favored when we look at the polarization projection (with $I_{+1} = 0.44 I_j$), the larger detuning due to the Zeeman shifts prevents stronger coupling. The force contribution due to coupling to the π transition turns out to be vital for MOT operation. It is the dominant contribution to the overall force generated by the secondary beams for negative-values. As the $m_F = 0$ transition is not shifted in the presence of a magnetic field, coupling to this transition is constant, only reduced due to saturation effects.

The overall force shows a much reduced acceleration with a maximal acceleration of $70\,\mathrm{km/s^2}$ compared to a standard six-beam MOT with same intensity, detuning and magnetic field gradient where the maximal acceleration is given as $220\,\mathrm{km/s^2}$. However, trapping remains feasible given a zero-crossing with a net positive acceleration for smaller z-values and a net negative acceleration for larger z-values. The gradient at the zero-crossing is the trapping constant κ.

This geometry is characterized by major differences from theory for the standard six-beam configuration and we will explore the consequences in the following sections.

RADIAL TRAPPING Let us now consider trapping along a radial symmetry axis y in the four-beam geometry. One of the secondary beams' projection in the x-y-plane is chosen to be aligned with the y-axis. The remaining two secondary beams' projection in the x-y-plane will form an angle of 19.47° with the y-axis. The resulting acceleration of the latter on an atom at rest is presented with dash-dotted lines in Fig. 7, while the resulting acceleration of the secondary beam propagating along y is presented with a dashed line. For clarity, the different distributions of coupling to the σ^-, π and σ^+ transitions are only displayed for the beams whose projection in the x-y-plane forms an angle with the y-axis. The handedness of the secondary beams does correspond to the handedness of the radial beams in the standard six-beam MOT so that the trapping dynamics show a lot more similarity to that case, and coupling to the σ^- transition provides the restoring force.

The overall force is not symmetric with respect to y for the given configuration with three secondary beams - the exact geometry of the beams in the radial plane has a minor influence on the overall force along the x- and y- axis. A configuration with four secondary beams restores symmetry.

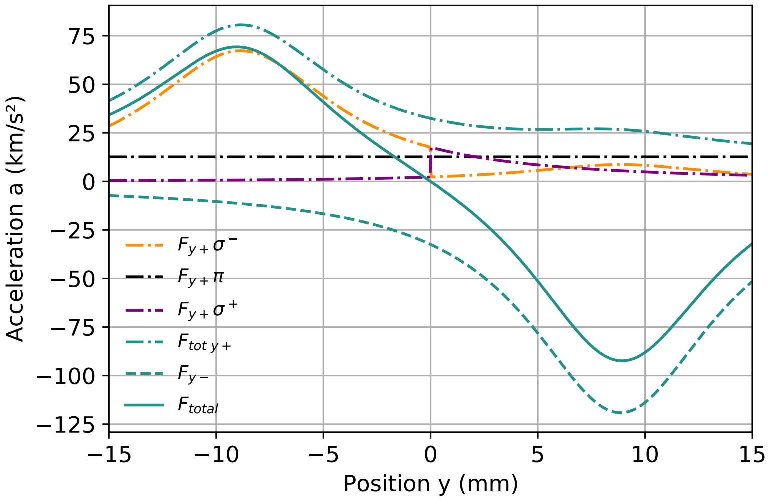

Figure 7: Illustration of radial acceleration acting on an atom at rest along the y-axis of the quadrupole field. The acceleration resulting from the beam whose projection in the x-y-plane is aligned with the y-axis is illustrated with the turqoise, dashed line and results from coupling to the σ^- transition only. The acceleration resulting from the two other secondary beams is indicated with the turqoise dot-dashed line. For these beams the indicate the contributions from coupling to the σ^- transition (orange), the π transition (black), and the σ^+ transition (purple) are also indicated. The total force is indicated with the turqoise, solid line. The magnetic field gradient is chosen as $dB/dz = 5\,\mathrm{mT/cm}$ and the detuning as $\Delta = -\Gamma$, the intensity of the incident beam is $I_0 = 0.5\,I_{sat}$.

2.3.1 *Angle Dependency*

As we have seen in Eq. 11–13, the intensity distribution on the different Zeeman transitions varies with the angle θ so that for an intensity balanced MOT, the axial trapping force will depend strongly on the angle θ the secondary beams form with the z-axis. The anti-trapping induced by the secondary beams is maximal for a vertical beam with $\theta = 0°$ where the beams counter-propagate the incident beam and no trapping is possible. The axial restoring force accelerating the atom to the trap center then steadily increases with increasing angle as depicted in Fig. 8. Assuming intensity balance, optimal coupling along this direction is reached for almost horizontal beams. However, as the required intensity for intensity balance is given by $I_j = \frac{1}{N\cos\theta} I_0$, amplification is needed for angles larger than $\theta = \arccos(1/N)$ as this yields $I_j > I_0$. For a compact, planar structure this is not feasible. For $N = 3$ and $N = 4$, this critical angle is given as 70.53° and 75.52°, respectively. The exception are grating chips, as diffracted light is compressed with $\frac{I_j}{I_0} = \epsilon\frac{1}{\cos\theta}$ where ϵ is the diffraction efficiency as discussed previously. As a result, the required diffraction efficiency for a balanced radiation pressure in a grating MOT is independent of the angle and solely depends on the number of diffracted beams.
For a 90° angle with the z-axis, no axial trapping can be achieved, as the secondary k-vectors' projection onto the z-axis becomes 0. As cooling largely relies on the Doppler effect that, for atoms moving along the z-axis, is maximized for counter-propagating beams along this axis, we observe the opposite preference here as depicted in Fig. 9.

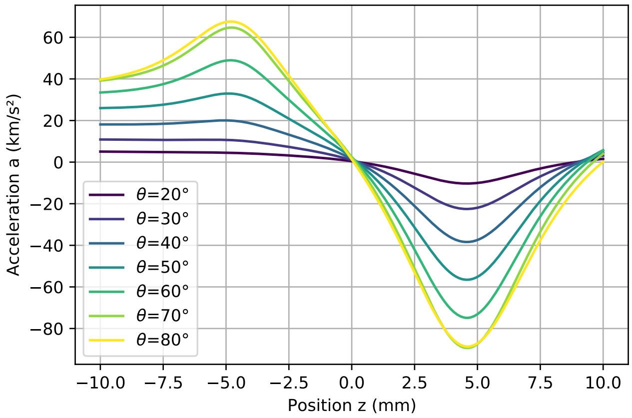

Figure 8: Total acceleration on an atom at rest along the z-axis as a function of the angle θ the secondary beams form with the incident beam.

The behavior of radial trapping and cooling is trivial and optimized for beams propagating along the radial symmetry axis with $\theta = 90°$ corresponding to the six-beam geometry for radial trapping and cool-

ing.
The analytical expressions for axial and radial trapping and cooling coefficients are derived by Taylor expansions of the total force $F = \sum_{j=1}^{N+1} \hbar\vec{k}R_j(\nu)$ where R_j is the scattering rate of the laser beam j. For the z-direction all beams are contributing. For the secondary beams we have $k_z^2 = \cos^2\theta$. The cooling coefficient for the axial direction then becomes [65]

$$\alpha_z = \left(1 + \frac{\cos^2\theta}{\cos\theta}\right) \frac{I_0}{I_{sat}} \cdot \frac{R8k^2\Delta}{\Gamma^2(1 + s_{tot} + 4\Delta^2/\Gamma^2)} \tag{19}$$

$$= \frac{(1+\cos\theta)}{2}\alpha \tag{20}$$

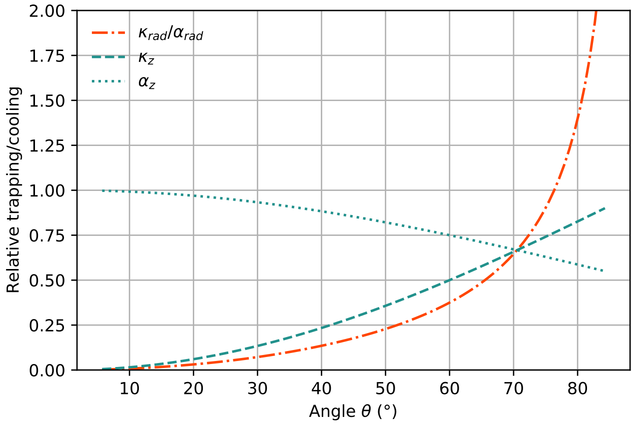

Figure 9: Angle dependency of trapping and cooling coefficients for axial and radial direction assuming balanced molasses.

For cooling in the radial direction, the incident beam is not contributing and $\sum_{j=1}^{N} \vec{k_i}^2 = \sin^2\theta/2$ for x and y direction as the diffracted/reflected beams are distributed symmetrically in the x-y plane by design. We then obtain [65]:

$$\alpha_{rad} = \frac{\sin^2\theta\, I_0}{2\cos\theta\, I_{sat}} \cdot \frac{R8k^2\Delta}{\Gamma^2(1 + s_{tot} + 4\Delta^2/\Gamma^2)} \tag{21}$$

$$= \frac{1}{4}\sin\theta\tan\theta\,\alpha \tag{22}$$

Note that these results only depend on the angle of the secondary beams formed with the z-axis and not on the number of secondary beams N.
By Taylor expanding the total force expression around $z = 0$, we obtain the trapping coefficients in the same way [65]:

$$\kappa_z = (1 - \cos\theta)\,\kappa \tag{23}$$

$$\kappa_{rad} = \frac{1}{4}\sin\theta\tan\theta\,\kappa \tag{24}$$

where κ is the trapping coefficient for the standard six-beam geometry (see Eq. 10. In Fig. 9 the radial and axial trapping and cooling coefficients are plotted as function of the angle θ, normalized with respect to trapping in a six-beam MOT with equivalent intensity.

2.3.2 *Intensity Imbalance Dependency*

So far, we have considered different configurations under the assumption of intensity balance. However, experimentally this can not always be achieved and understanding the trapping dynamics for different degrees of imbalance is thus vital for trap design. In order to study the influence of intensity imbalance, we introduce the intensity imbalance parameter η with $I_j = \frac{1}{N\cos(\theta)}\eta I_0$. In Fig. 10, the overall force is plotted for different values of η. For $\eta < 1$, the intensity of the secondary beams is reduced and as a result the restoring as well as the anti-trapping force from the secondary beams is reduced yielding a decreased acceleration for negative z-values and an increased absolute acceleration for positive z-values. Overall trapping weakens with the trapping constant κ decreasing as the zero-crossing is shifted to a point with a weaker slope. The MOT position, i.e. the point where the acceleration is 0, is shifted as depicted in Fig. 11 a). For $\eta < 0.4$ this shift increases rapidly and trapping eventually becomes impossible.

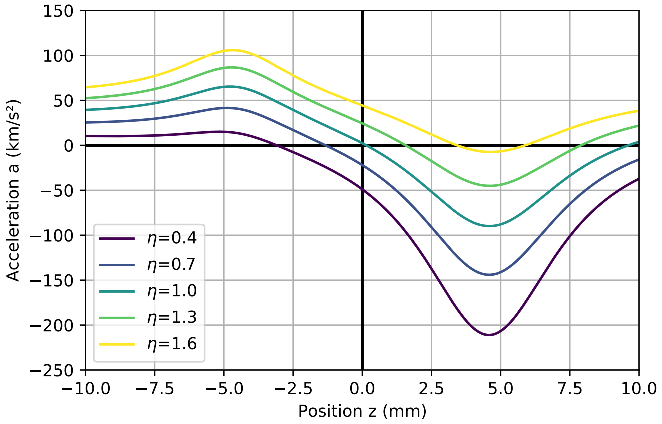

Figure 10: Total force on an atom at rest along the z-axis for different degrees of intensity imbalance. Y-axis and x-axis are indicated in black.

The case $\eta > 1$ again corresponds to $I_j > I_0$ and as previously mentioned needs amplification which is unrealistic for a compact, planar structure. The exception are diffraction gratings due to intensity compression so that $\eta > 1$ is mostly of concern for grating structures. For $\eta > 1$, the restoring as well as the anti-trapping force from the secondary beams increases yielding an increased acceleration for negative z-values and a decreased absolute acceleration for positive z-values. For large η, the anti-trapping force eventually becomes dom-

inant resulting in a positive acceleration for all z-values. The zero-crossing vanishes and atoms can no longer be trapped. Again, the overall trapping force decreases for $\eta > 1$.
Fig. 11 b) further shows the dependency of the cooling and trapping coefficients on intensity imbalance normalized with respect to a six-beam MOT with equivalent intensity and $\eta = 1$.

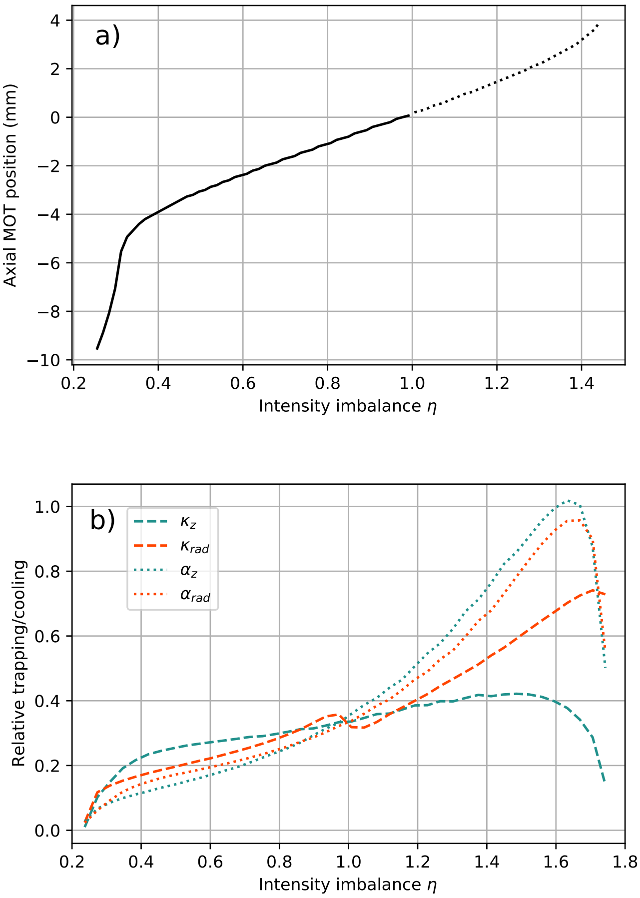

Figure 11: Axial position and traping and cooling coefficients as function of the intensity imbalance parameter η. a): Axial MOT position for different degrees of intensity imbalance η. b): Trapping and Cooling coefficients κ and α as a function of the intensity imbalance parameter η

2.3.3 *Temperature*

As previously, we assume that spontaneous emission is isotropic and neglect dipole radiation.

Generally, the Doppler temperature limit is given by the ratio of heating taking place due to absorption and subsequent emission and the the damping/cooling coefficient for velocity α [65]. We have already derived the damping coefficient as function of angle in Sec. 2.3.1. The heating rate is calculated from the number of scattering events due to absorption and spontaneous emission where the latter is assumed to be isotropic in order to simplify calculations. The contribution to the heating rate due to spontaneous emission is thus given as $\hbar^2 k^2 R_j/3$ for each spatial direction. Meanwhile, the contribution to the heating rate due to absorption in the x-,y-, and z-direction is proportional to the intensity in that direction/projection of the k-vector of each beam. The total heating rate D in each direction $x-, y-, z$ is then given by [65]:

$$D_x = \sum_{j=0}^{N} \hbar^2 s_i R \left(k_{jx}^2 + \frac{k_j^2}{3} \right) \tag{25}$$

$$= \hbar^2 s_0 R \left(\frac{1}{3} + \frac{1}{\cos\theta} \left(\frac{1}{2} \sin^2\theta + \frac{1}{3} \right) \right) \tag{26}$$

$$D_y = \sum_{j=0}^{N} \hbar^2 s_j R \left(k_{jy}^2 + \frac{k_i^2}{3} \right) \tag{27}$$

$$= \hbar^2 s_0 R \left(\frac{1}{3} + \frac{1}{\cos\theta} \left(\frac{1}{2} \sin^2\theta + \frac{1}{3} \right) \right) \tag{28}$$

$$D_z = \sum_{j=0}^{N} \hbar^2 s_j R \left(k_{jz}^2 + \frac{k_j^2}{3} \right) \tag{29}$$

$$= \hbar^2 s_0 R \left(\frac{4}{3} + \frac{1}{\cos\theta} \left(\cos^2\theta + \frac{1}{3} \right) \right) \tag{30}$$

We can now express the temperature in radial and axial direction for our geometry compared to the standard six-beam geometry and obtain [65]:

$$T_{\mathrm{radial}} = \frac{T_{\mathrm{lim}}}{6} \left(3 + \frac{1}{\sin^2(\theta/2)} \right) \tag{31}$$

$$T_{\mathrm{axial}} = \frac{T_{\mathrm{lim}}}{6} \left(3 + \frac{1}{\cos\theta} \right) \tag{32}$$

where T_{lim} is the previously derived Doppler temperature in optical molasses i.e. the standard six-beam configuration given in Eq. 6. This shows explicitly the dependence of the minimal temperature achievable with Doppler cooling in a magneto-optical trap on the angle the secondary beams form with the vertical axis. For typical values of θ, we find that the radial temperature lies above the Doppler cooling limit of the standard six-beam configuration and the axial temperature typically lies below this limit.

2.4 NARROW-LINE MOT

So far we have considered the $^1S_0 \rightarrow ^1 P_1$ transition with a linewidth of 32 MHz operated with a detuning of $\approx -\Gamma$. We will now venture into new territory and discuss narrow-line transitions in non-trivial single beam geometries. First, let us review some key characteristics of narrow-line transitions. For strong transitions, such as the 1st stage cooling transition in strontium, the maximum acceleration is typically several orders of magnitude larger than the gravitational acceleration on earth. For strontium, the maximum acceleration on the $^1S_0 \rightarrow ^1 P_1$ transition is five orders of magnitude larger than the gravitational acceleration $g = 9.81\,\mathrm{m/s^2}$ (see Tab. 1). However, as seen in Tab. 1, for the the $^1S_0 \rightarrow\ ^3P_1$ transition in ^{88}Sr, the ratio of the maximum acceleration by photon scattering to the gravitational acceleration is only a factor of 16 and 4000 times smaller than for the 1st stage cooling transition. Gravity thus plays a significant role for 2nd stage cooling and can no longer be neglected.

Indeed, the intercombination transition is so weak in some light alkaline earth atoms, that the gravitational acceleration dominates and no MOT can form

Similarly, the ratio of the transition linewidth to the photon recoil frequency $\Gamma/\omega_{\mathrm{recoil}}$ is much reduced in the narrow-line MOT. While this ratio is on the order of 10^3 for the broad-line transition, it is 1.6 for the narrow-line transition [17].

Furthermore, as the linewidth is more than a factor 4000 smaller for the narrow-line transition, the saturation intensity is much reduced. As a result, intensities of several thousand saturation intensities are feasible in experiments and are indeed used, resulting in a power-broadened transition linewidth with $\Gamma_E = \sqrt{1+s}\,\Gamma$. Generally, three different regimes are differentiated for narrow-line cooling [17, 56]:

Regime I: $s \gg 1$, $|\Delta| \gg \Gamma_E$

For intensities much larger than saturation intensity and a detuning significantly larger than the power-broadened linewidth, the dynamics of the narrow-line MOT differ significantly from the broad-line MOT and its friction-like force. Scattering from a single beam dominates and the atoms collect close the position where the beam counteracting gravity is resonant. As a result, so-called shell formation can be observed where the atoms occupy the lower boundary of an ellipsoid depending on detuning and magnetic field gradient [17]. The force resulting from each laser beam can be imagined as walls that the atoms are bounced off of.

Regime II: $s \gg 1$, $|\Delta| < \Gamma_E$

For large intensities and a detuning smaller than the power-broadened linewidth, the trapping dynamics resemble those of the 1st cooling stage. The effect of gravity plays a subordinate role.

Regime III: $s \approx 1$, $\Gamma \approx \omega_{\mathrm{recoil}}$

For intensities on the same scale as the saturation intensity, the photon recoil plays a significant role and a semi-classical treatment of MOT dynamics no longer accurately describes the light-atom interaction.

With these considerations in mind, we now shift our focus back to non-trivial single-beam configurations.

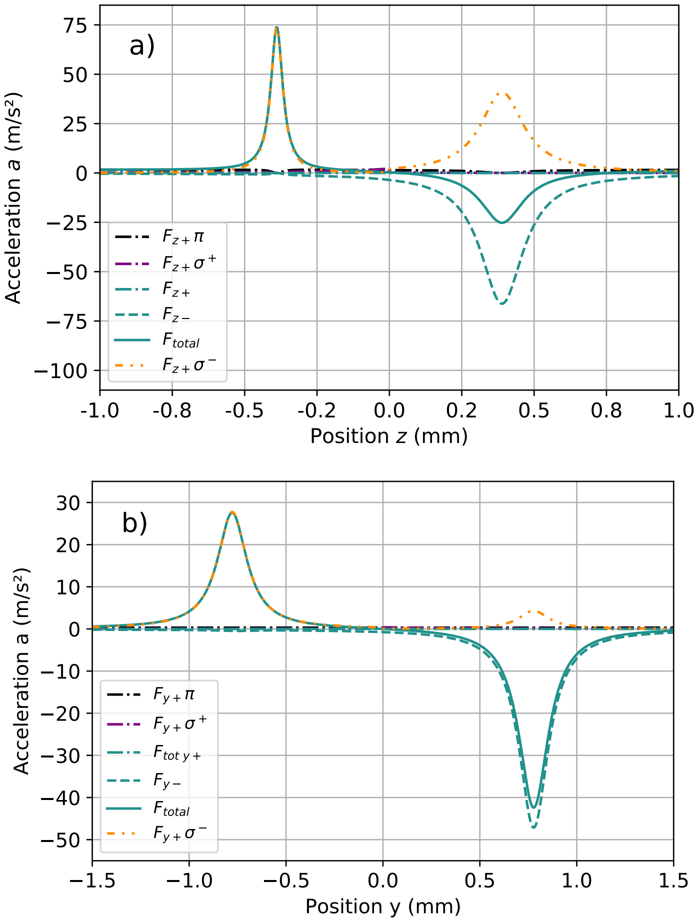

Figure 12: Acceleration on an atom at rest along the axial and radial direction in the narrow-line cooling stage for a single-beam, non-trivial geometry. a): Total axial acceleration for the narrow-line transition along the z-axis with contributions from coupling to the σ^+, π, and σ^- transition b): Total radial acceleration along the y-axis for the narrow-line transition along the y-axis with contributions from coupling to the σ^+, π and σ^- transition. The laser intensity of the incident beam is chosen as $s = 500$ with a detuning $\Delta = -70\Gamma$ and the magnetic field gradient is $dB/dz = 0.9\,\text{mT/cm}$

Fig. 12 a) and b) illustrate the contributions of the different transitions to the overall acceleration in axial and radial direction on an atom at rest on the narrow-line MOT respectively. Parameters chosen correspond to Regime I with $s = 500$, $\Delta = -70\Gamma$ and $dB/dz = 0.9\,\text{mT/cm}$. In contrast to the 1st cooling stage, we observe that coupling to the π, and σ^+ transition is negligible as MOTs in this regime are operated with large detunings. Indeed, trapping results from coupling to the σ^- transition as it is the case for the standard six-beam geometry. For a few hundred saturation intensities, the weak coupling to this transition by the secondary beams no longer decreases MOT performance as dramatically as for the strong transition. Due to the large intensity, coupling to the σ^- transition from the secondary beams results in a peak acceleration corresponding to $\approx \frac{\Gamma}{4}\frac{\hbar k}{M} \approx 75\,\mathrm{m/s^2}$.

For positive z-values the peak acceleration is $\approx \frac{\Gamma}{12}\frac{\hbar k}{M} \approx 25\,\mathrm{m/s^2}$. Again, we see that that the acceleration is reduced significantly by coupling to the σ^- transition from the secondary beams generating an anti-trapping contribution at this position.

Forces acting on an atom at rest along the radial axis results predominantly from coupling to the σ^- transition thus resembling the standard six-beam geometry as depicted in Fig. 12 b).

While a key characteristic of Regime I in standard six-beam MOTs is that atoms moving along the x-,y- or z-axis will only interact with one laser beam at a time in a first order approximation, this no longer holds for this geometry. Atoms moving along the z-axis will scatter photons from all secondary beams on one side of the magnetic minimum and from all beams on the other side of the magnetic minimum. This aspect as well as the asymmetry of the forces in the given geometry demands a careful choice of the orientation of the beams with respect to gravity. In any case, as the atoms collect at the beam(s) counteracting gravity, they will now also experience heating due to absorption orthogonal to the direction of gravitational acceleration. A question that immediately arises is the resulting consequences for the temperatures that can be achieved, which will be discussed in Sec. 2.4.4.

In Fig. 13, the resulting acceleration on an atom at rest along the y-axis, as well as the potential energy for an incident beam aligned (anti-)parallel to gravity is presented for different detunings. As the detuning is decreased, we transition from Regime I to Regime II. In this regime coupling to the π transition becomes significant again as the detuning approaches the power-broadened linewidth of the ${}^3P_1$ to ${}^1S_0$ transition. For a detuning of $-200\,\mathrm{kHz}$, a (in the area of interest) constant force is added (subtracted) to the slope which is given by the gravitational acceleration for larger detunings. For MOT operation in Regime II the asymmetry of the forces is particularly striking. However, Fig.13 b) and c) also illustrate the asymmetry for large detunings well. As a result, how structures are mounted with respect to gravity is one of consequence and an orientation where the secondary beams counteract gravity appears preferential.

Similarly, Fig. 14 shows the transition from Regime I to Regime II as the intensity increases and thus the linewidth is broadened reducing the relative detuning. Again, Fig. 14 b) and c) illustrate the asymmetry of the MOT forces. With increasing intensity and therefore transition to Regime II, the deviation of the slope from a slope given by the gravitation potential increases as well as the asymmetry in the "barrier" of the potential pot.

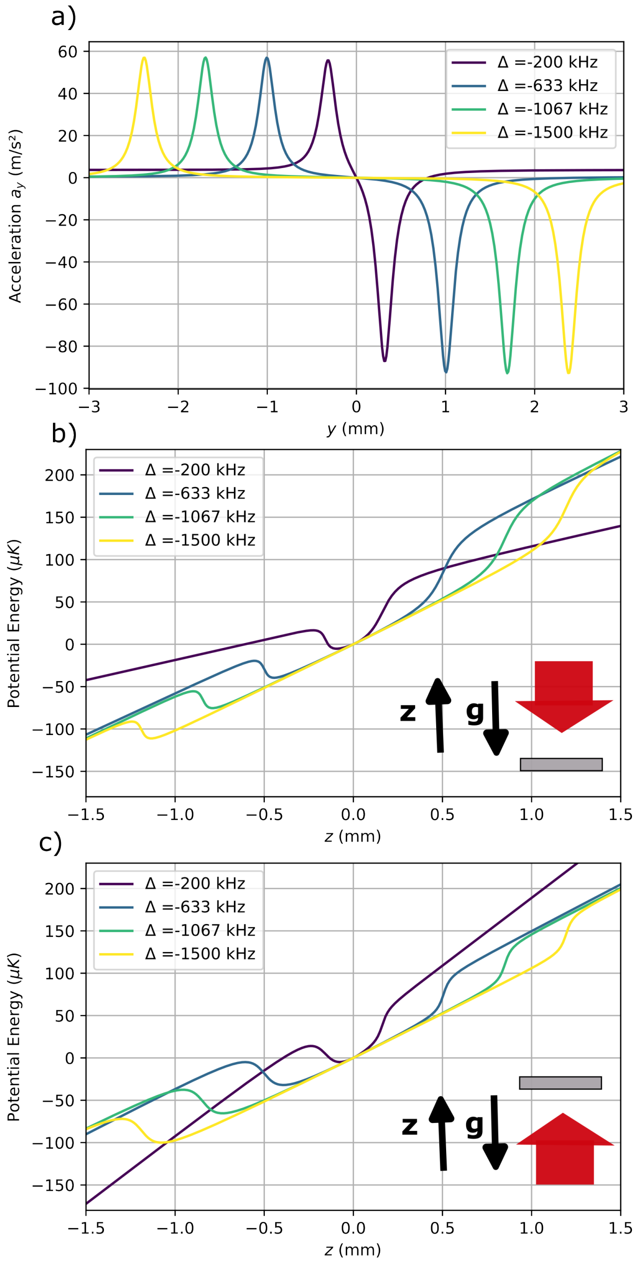

Figure 13: Detuning dependency of the trap dynamics a) Radial acceleration on an atom at rest along the y-axis. b) Potential for an atom at rest with the incident beam counteracting gravity c) Potential on an atom at rest with the secondary beams counteracting gravity

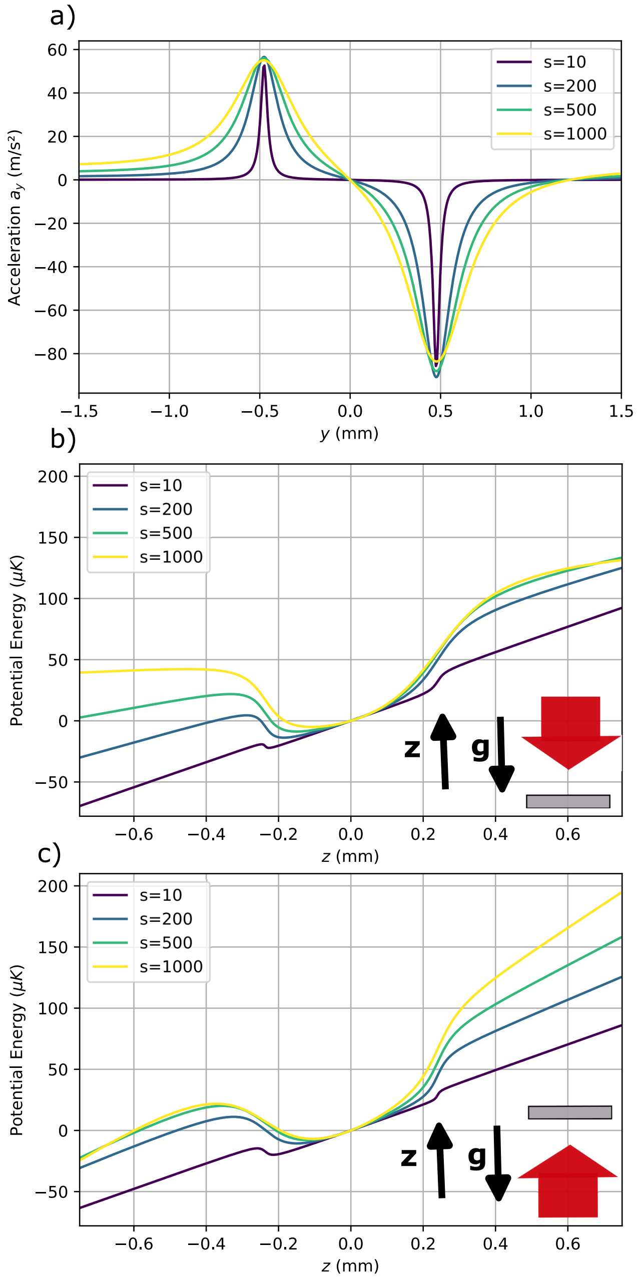

Figure 14: Intensity dependency of the trap dynamics a) Radial acceleration on an atom at rest along the y-axis. b) Potential for an atom at rest with the incident beam counteracting gravity c) Potential for an atom at rest with the secondary beams counteracting gravity

2.4.1 *Angle Dependency*

As for the 1st stage MOT previously, we again study the angle dependency of the forces in the MOT. Here, we consider a narrow-line MOT operated in regime I with the intensity of the incident laser chosen as $s = 200$, the magnetic field gradient is $dB/dz = 0.9\,\mathrm{mT/cm}$, and $\Delta = -400\,\mathrm{kHz}$. Fig. 15 depicts the total acceleration a acting on an atom at rest along the z-axis for different angles θ. The angle dependency of the overall acceleration on an atom at rest along the axial axis behaves similar to the strong transition. Again, we observe that for an increasing angle θ the overall trapping force improves as anti-trapping due to coupling to the σ^- transition for negative z decreases. However, while for the strong transition the total acceleration for even $\theta = 20°$ is still on the order of several $10^3\,\mathrm{m/s^2}$ due to the large linewidth of the transition, we find that $|a| < |g|$ for $z > 0$ for the narrow-line MOT. Here, this corresponds to a configuration where the incident beam counteracts gravitational acceleration and we conclude that in this configuration geometries with $\theta <\approx 40°$ do not provide stable operation at low intensities as the atoms can not be held against gravity.

Indeed, operation at low intensities remains a concern for $|a| > |g|$ for $z > 0$ as the atom only stays on resonance for a small number of scattering events and can be pushed out of the trap by coupling to the σ^- transition from the secondary beams quickly so that θ should be chosen as close to tetrahedral configuration as possible.

This further illustrates that a geometry where the secondary beams counteract gravity is preferential.

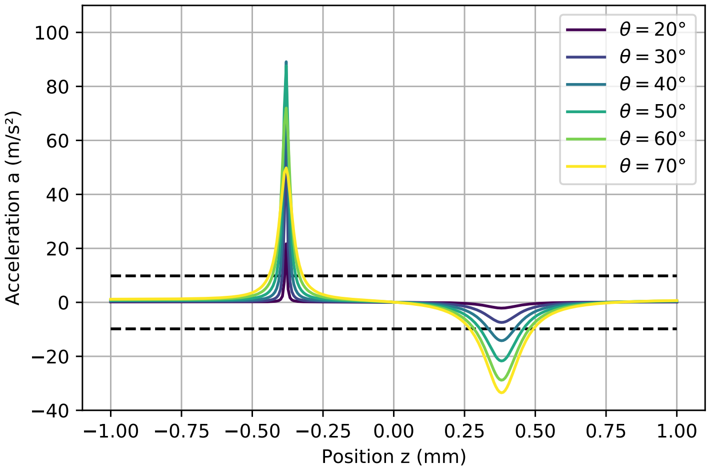

Figure 15: Total axial acceleration for the narrow-line transition on an atom at rest along the z-axis for different angles θ. The intensity of the incident beam is $s = 200$, the magnetic field gradient is $dB/dz = 0.9\,\mathrm{mT/cm}$ and the detuning is $\Delta = -400\,\mathrm{kHz}$, corresponding to regime I. The black dashed lines indicate gravitational accleration for an orientation of the trap where the incident beams counteract gravity (negative sign) and where the secondary beams counteract gravity (positive sign).

2.4.2 *Intensity Imbalance*

We have investigated the influence of intensity balance for the 1^{st} stage MOT extensively and found that a balanced radiation pressure is crucial. Again, we analyze the 2^{nd} stage MOT in a similar way.
Figure 16 shows the overall acceleration in the 2^{nd} stage MOT for an atom at rest along the z-axis for an intensity of $s = 10$ and $s = 1000$ of the incident beam and different values of the previously introduced intensity imbalance parameter η. As before, a reduced intensity in the secondary beams leads to a reduced anti-trapping force and significantly improves trapping for positive z-values. However, this effect no longer comes at the price of a much reduced trapping force for negative z or an overall negative impact on the trapping constant. The high saturation results in sufficient coupling to the σ^- transition so that the effect on the acceleration for $z < 0$ is only noticeable for low intensities with $s < 10$.

One does need to keep in mind though that typically atoms are initially transferred to a so-called broad-band MOT operating in Regime II where the laser is modulated and thus artificially broadened. This improves transfer efficiency from the first to the second cooling stage as atoms are still relatively hot with a temperature of 1 mK corresponding to a Doppler shift on the order of MHz. In this regime intensity imbalance will have a negative impact on the cooling process as previously analyzed for the first cooling stage.

Overall, while an approximate intensity balance is vital for the first cooling stage, small reductions in intensity of the secondary beams can be tolerated and even improve the overall force of the single-frequency narrow-line MOT.

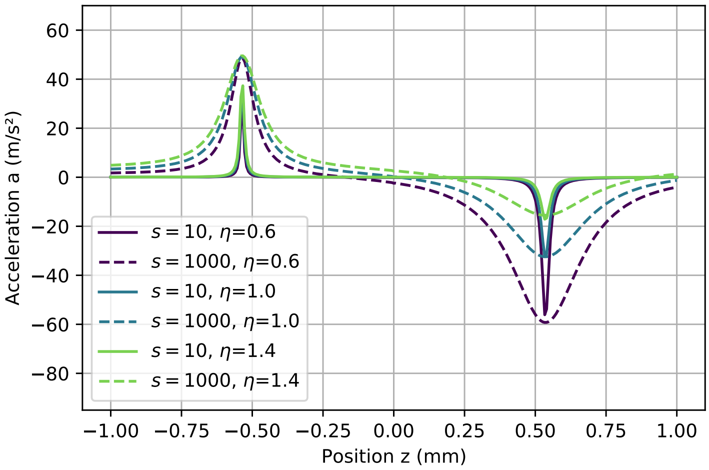

Figure 16: Total axial acceleration for the narrow-line transition on an atom at rest along the z-axis for laser intensities of $s = 10$ and $s = 1000$ of the incident beam and different degrees of intensity imbalance $\eta = 0.6, 1.0, 1.4$. The detuning is chosen as $\Delta = -75\Gamma$ and the magnetic field gradient is $dB/dz = 0.9\,\mathrm{mT/cm}$

2.4.3 *Acceleration in Phase-space*

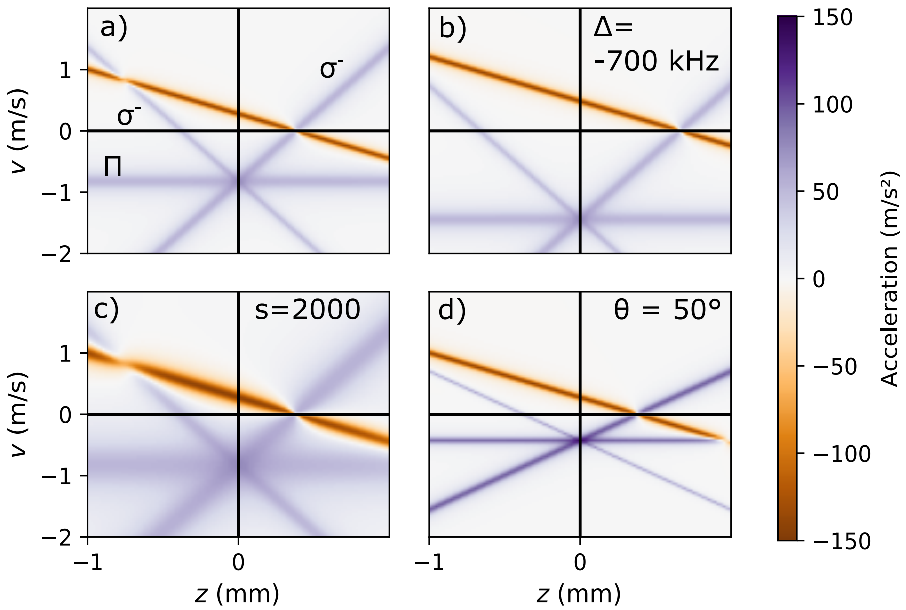

Figure 17: Phase Space diagram for the narrow line MOT along the z-axis. Different parameters are varied to illustrate their effect. a) Phase-space diagram with default parameters $s = 250$, $\Delta = -400\,\mathrm{kHz}$, $\theta = 70.53°$, $dB/dz = 0.9\,\mathrm{mT/cm}$ b) Phase-space diagram with $\Delta = -700\,\mathrm{kHz}$, all other parameters as in a). c) Phase-space diagram with $s = 2000$, all other parameters as in a). d) Phase-space diagram with $\theta = 50°$, all other parameters as in a).

So far we have limited ourselves to atoms at rest which limits our understanding of atomic motion in the trap. Phase-space diagrams, that show the acceleration acting on an atom for any given velocity along an axis, allow a deeper understanding of the trap dynamics. Figure 17 presents phase space diagrams for variation of detuning, laser intensity and angle θ the secondary beams form with the incident beam. We observe three distinct purple bands indicating positive acceleration resulting from the secondary beams as well as one distinct orange band indicating negative acceleration resulting from the incident beam. The orange band is readily understood as coupling to the $\sigma^{-/+}$ transition from the incident beam. As the beam becomes resonant when Doppler shift and Zeeman shift match the detuning of the beam, the resonance position depends on velocity and position. The three purple bands in the phase-space graph result from coupling to the π and $\sigma^{-/+}$ transition. As we have seen in Fig. 12, acceleration resulting from coupling to the σ^{+} transition is negligible for MOT operation in regime I and velocity near $0\,\mathrm{m/s}$. Excitation of the σ^{-} transition by the secondary beams results in two bands with axial symmetry corresponding to the symmetry of the Zeeman shift along the axis. The position where this transition is resonant is given

Phase-space diagram of a six-beam MOT with $\Delta = -300\,\mathrm{kHz}$ and $s = 2000$ for reference. Other parameters are kept as given in the text.

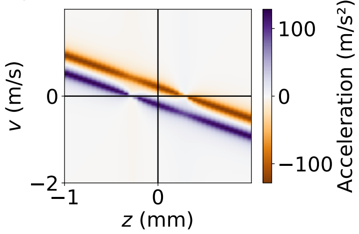

by the condition $\Delta = \vec{k} \cdot \vec{v} + \Delta E(z)$ so that the slope of the purple bands deviates from the slope of the orange band due to the oblique angle the secondary beams form with the z-axis.
The horizontal band results from coupling to the π transition as the $m_F = 0$ states do not experience a position-dependent Zeeman shift and thus the resulting force is independent of position.
An increase in detuning shifts all lines away from $v = 0$ as, now, a larger Doppler shift is needed for the atom to become resonant with the laser beams as seen by comparing Fig. 17 a) and b). In particular, the band resulting from excitation of the π transition is moved to higher velocities. This illustrates the increased coupling to the π transition with decreasing detuning as we e.g. move from Regime I to Regime II.
An increase in intensity from $s = 50$ to $s = 2000$ results in a broadened linewidth as seen in Fig. 17 c) where the bands are broadened. A decrease of the angle θ yields a higher acceleration from the secondary beams. Furthermore, the slope of the σ^- line is decreased as the frequency shift resulting from the Doppler effect depends on the angle between the wave vector and velocity vector of the atom.

2.4.4 *Temperature*

While a theoretical derivation of the Doppler cooling limit was feasible using a semi-classical model for the strong transition, the same considerations do not apply in the case of a narrow-line transition. For the strong transition, we considered an atom at the magnetic field minimum where the trap coefficient κ and the cooling coefficient α described confinement and cooling for the region of interest where we expect the atom cloud to form. The shape of the force in the SF phase differs significantly from the strong transition. We think of the atom as trapped between hard wall boundaries. The MOT will form at one of those walls where gravitational acceleration experienced by the atoms is balanced by the acceleration resulting from the MOT beams. The exact position is given by the detuning and for a narrow-line MOT operated in regime I it is no longer at the magnetic field minimum. The model of a restoring force and a friction force with a given coefficient is thus no longer a good model – both coefficients would depend strongly on the exact position and velocity of the atom. Furthermore, the photon recoil becomes significant, in particular for low intensities. The semi-classical model we have used thus no longer describes the dynamics of a narrow-line MOT accurately.

pyLCP is a powerful tool for modelling light-atom interaction with a optical Bloch equation model, a rate equation model, and a heuristiq model and was developed by Stephan Eckel et al. at the University of Maryland/NIST. [25]

A more realistic picture is given by a rate equation model provided by the Python package “pyLCP” focusing on the populations in the different states [25]. This model calculates the motion of an atom in the MOT using pumping and decay rates/probabilities for each time step considering transition strengths as well as the exact position and velocity of the atom. It further considers photon recoil effects from spontaneous emission. The motion of the atom is then given as [25]:

$$\ddot{r} = \sum_i \frac{\hbar k_i}{2M} \sum_{j,k,l,m} R^{k\to j}_{lm,i} \left(N^j_m - N^k_l\right) + g \tag{33}$$

where $R^{k\to j}_{lm,i}$ denotes the optical pumping rates due to laser beam i between states l and m in manifolds k and j and N^k_l denotes state l in manifold k. A detailed explanation can be found in Ref. [25]. Coherent processes given by the optical Bloch equations are neglected in this model.

For reference, we simulate the temperature in a ^{88}Sr MOT in a standard six-beam configuration with a detuning of $-650\,\mathrm{kHz}$ for different intensities. Results are in good agreement with the experimental data from Boyd [17] who further found that the data follows $T(s) = \hbar\Gamma\sqrt{1+s}/2k_B\hbar$ for $s > 10$.

We simulate the motion of a sample of 400 atoms in a single-beam MOT for different angles θ of the secondary beams, an intensity of the incident beam of $s = 200$, a detuning $\Delta = -650\,\mathrm{kHz}$, and a magnetic field gradient of $dB/dz = 0.9\,\mathrm{mT/cm}$. As we have seen that the potential in the narrow-line MOT is asymmetric, we separately consider a geometry with the incident beam parallel and anti-parallel to the gravitational acceleration.

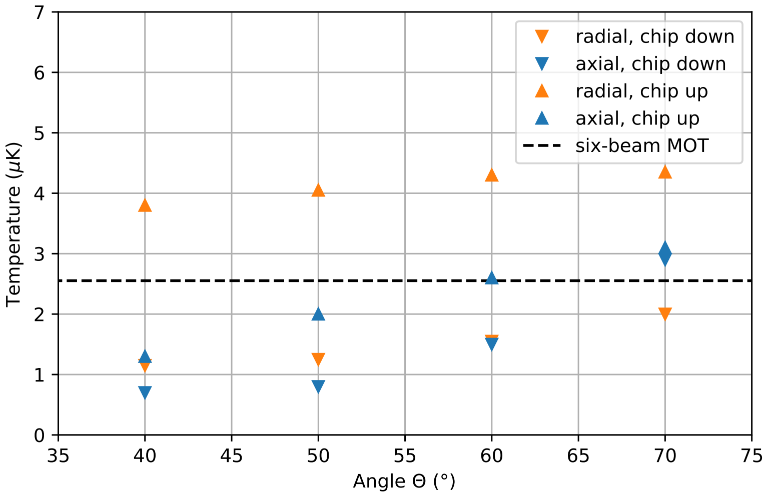

Figure 18: Simulated temperature of atoms in the narrow-line MOT for an intensity of the incident beam of $s = 200$, $\Delta = -650\,\mathrm{kHz}$ and $dB/dz = 0.9\,\mathrm{mT/cm}$ as function of angle θ. Radial temperatures are given in blue and axial temperatures in orange. Results are given for an incident beam parallel (chip down) and anti-parallel (chip up) to gravitational acceleration as indicated by the marker. The black dashed line indicates the Doppler cooling limit for a six-beam MOT with equivalent intensity.

For the case where gravitational acceleration is anti-parallel to the k-vector of the incident beam (chip up), we observe a higher temperature than for the case where gravitational acceleration is parallel to the k-vector of the incident beam (chip down) in both axial and radial direction. For radial direction, the difference is particularly large. This is readily explained by the large number of scattering events from the secondary beams in addition to scattering from the incident beam counteracting gravity. This results in excess heating. A larger angle θ results in an increased additional heating rate in radial direction and thus slightly higher temperatures, contrary to 1^{st} stage cooling where we obtain lower temperatures for increasing angle θ due to the higher cooling coefficient playing a dominant role. For axial temperatures, we also observe a clear increase in temperature with increasing angle θ, in agreement with the results for strong transition laser cooling where the dependency on angle however is small. With the gravitation acceleration on a similar scale as acceleration from scattering, efficient cooling plays an enhanced role. As we have seen previously, two counter-propagating beams (corresponding to $\theta = 0°$) are ideal for cooling so that a small angle θ is beneficial. Interestingly, for $\theta < 60°$ we obtain lower temperatures than in the standard six-beam MOT. Here, atoms scatter photons almost solely from the beam counter-acting gravitational acceleration. Adding beams accelerating the atom in the opposite direction and providing additional cooling is thus indeed beneficial and has a stronger impact than the additional heating rate for small angles θ. Of note is further a relatively large ratio of radial to axial temperature in this geometry. For $\theta = 40°$ this ratio is ≈ 3 and decreases to 1.5 for $\theta = 70°$.

For the orientation "chip down" with the secondary beams counter-acting gravity, cooling is more isotropic reaching similar temperatures in axial and radial direction. We observe the same qualitative dependence of radial and axial temperature on the angle θ. For the radial temperature a similar argument can be made as previously. As the atom in this configuration will almost exclusively experience scattering from the secondary beams all forming an angle with the z-axis, the angle dependence of the temperature is stronger. As this configuration provides isotropic cooling to $\approx 1\,\mu\text{K}$, it is the preferential choice in agreement with our considerations in Section 2.4.1.

2.5 CONSIDERATIONS FOR ISOTOPES WITH HYPERFINE STRUCTURE

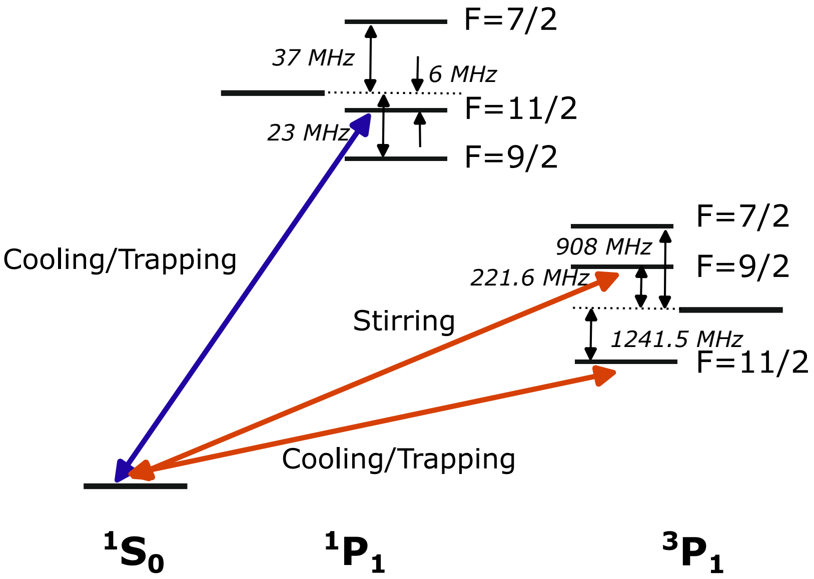

Figure 19: Hyperfine splitting of the 1st and 2nd cooling stage in ^{87}Sr. The excited states are split into $F = \{I - J, I, I + J\}$. Frequency shifts of the hyperfine states are indicated.

As ^{87}Sr possesses a non-zero nuclear spin $I = 9/2$, cooling and trapping dynamics become more complicated compared to the simple bosonic case. Coupling of the total orbital momentum J and the nuclear spin I to the quantum number F with $\vec{F} = \vec{I} + \vec{J}$ results in hyperfine splitting of each $^{2S+1}L_J$ state into $2J + 1$ levels with $I - J \leqslant F \leqslant I + J$. Each of these levels is frequency-shifted with the shift depending on the quantum numbers F, I, and J as well as the magnetic dipole and electric quadrupole interaction constants. The resulting hyperfine splitting for the 1st and 2nd cooling stage in strontium is illustrated in Fig. 19. In the presence of a magnetic field, each Zeeman sublevel m_F is shifted by $\Delta E \approx m_F g_F \mu_B B$. Due to the large nuclear spin, the $^1S_0$ ground state has 10 Zeeman sublevels. For cooling, an $F_g \to F_e = F_g + 1$ transition is advantageous as $\sigma^\pm$ and π transitions than exist for all m_F states including the stretched states, where pure $\sigma^\pm$ coupling provides a quasi-closed cooling transition. The excited states with $F = 11/2$ then possess 12 Zeeman sublevels.

This added complexity to the level structure has important consequences for laser cooling and trapping for both the first and second cooling stage.

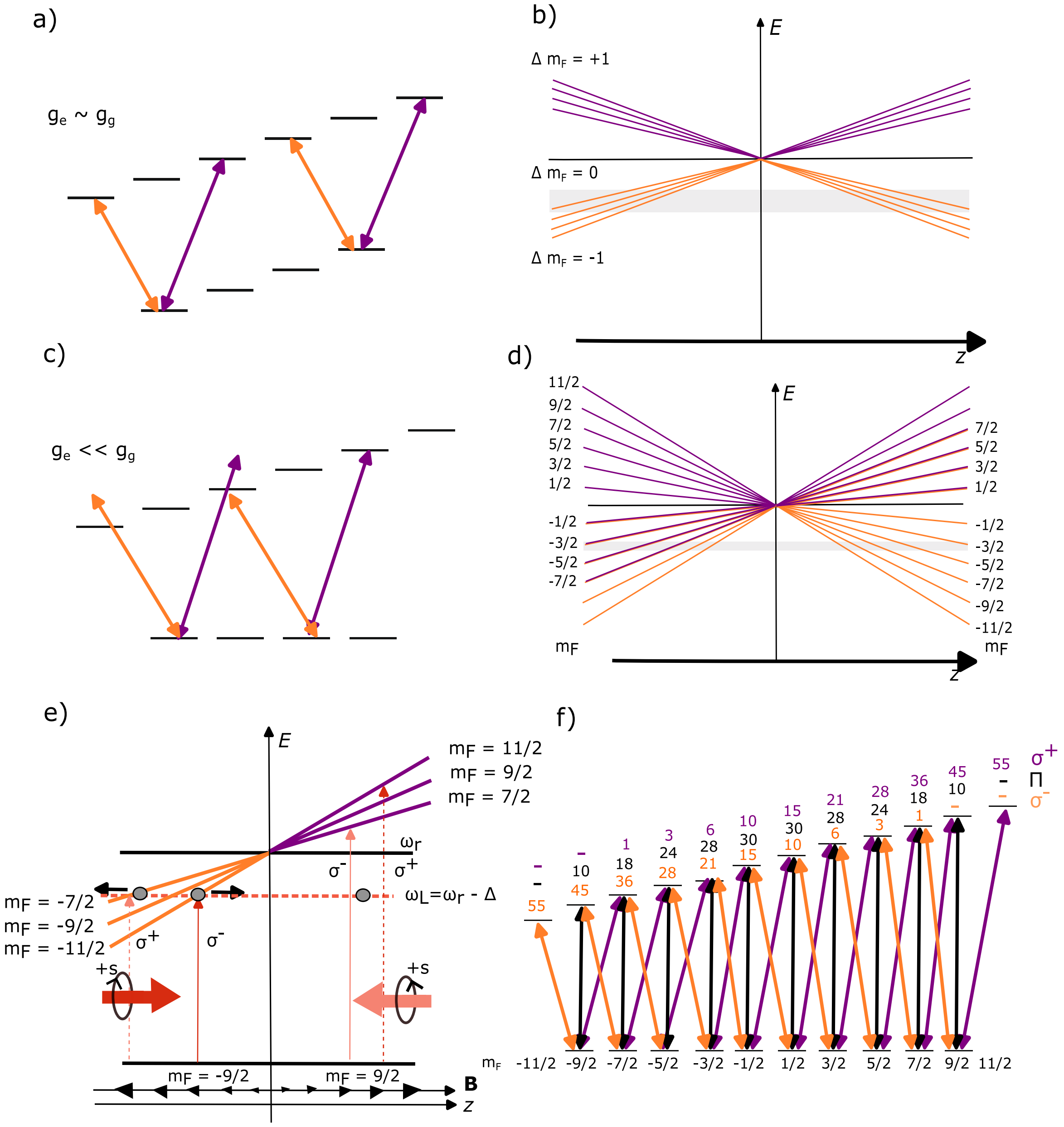

Figure 20: a)-d) Comparison of hyperfine splitting in alkaline and alkaline-earth atoms. e) Illustration of "untrappable" Zeeman sublevels. f) Relative transition strengths of the σ^-, π and σ^+ transitions for $F_g = 9/2, J_g = 0 \rightarrow F_e = 11/2, J_e = 1$ in ^{87}Sr. Adapted from [17, 72, 101]

2.5.1 *Broad-line MOT*

The ${}^1P_1$ state used for 1st stage laser cooling has three hyperfine states with $F = \{7/2, 9/2, 11/2\}$. To fulfill the condition $F_g \rightarrow F_e = F_g + 1$, the $F = 11/2$ state is used for laser cooling/trapping which is shifted by 6 MHz. However, the hyperfine structure is not resolved with the other two hyperfine states shifted by 37 MHz and 23 MHz for the $F = 7/2$ and $F = 9/2$ state respectively. With the frequency shifts on the order of the transition linewidth, excitation of the other hyperfine states is inevitable.

For alkali atoms, the Landé g-factor for ground state and excited state are usually comparable. As both ground and excited states experience similar Zeeman shifts, the resonance frequency of a σ^-, π or σ^+ transition is nearly independent of the Zeeman sublevel of the ground state occupied by the atom. As a result, the trap dynamics are similar to a simple $J = 0 \rightarrow J = 1$ as considered for ^{88}Sr thus far. This is illustrated in Fig. 20 a) and b). For atoms such as rubidium, the atom dynamics in a MOT thus have sufficient resemblance with a $J = 0 \rightarrow J = 1$ MOT and can be modeled as such. For alkaline-earth-like atoms on the other hand, the Landé g-factor of the excited state is much larger than the g-factor of the ground state as the latter is only given by the nuclear momentum with $J = 0, F = I$. We can thus approximate the energy of the ground state as independent of the Zeeman sublevel m_F populated by the atom. The slope of the Zeeman shift of the excited state on the other hand depends strongly on the Zeeman sublevel m_F' such that $\Delta E(m_F, m_F') \approx \Delta E(m_F') = g_F' \mu_B m_F' B$. Consequently, the resonance frequencies for σ^- , π or σ^+ transitions depend strongly on the m_F Zeeman sublevel of the ground state with $\Delta m_F' = m_F - 1, m_F, m_F + 1$.

This situation is illustrated for ^{87}Sr in Fig. 20 c) and d). Indeed, we find that for some Zeeman sublevels trapping is not possible. Such a case is depicted in Fig. 20 e). Here, we consider an atom in the $m_F = -9/2$ state in the standard six-beam configuration with a pair of counter-propagating laser beams. For $z < 0$ we find that the beam pushing the atom back towards the center of the trap drives a σ^- transition to the $m_F' = -11/2$ state where the detuning corresponds to the sum of Zeeman shift and Doppler shift. On the other hand, the laser beam pushing the atom further away from the trap center drives a σ^+ transition to the $m_F' = -7/2$ state. Both beams are off-resonant for $z > 0$ leaving the atom free to escape the trap. The transition probabilities are given by the Clebsch-Gordan coefficients as depicted in Fig. 20 f). We find that the ratio between restoring and expulsive force is beneficial and as large as $55 : 1$ for the stretched state $m_F = -9/2$ providing a quasi-cycling transition once atoms are pumped to this state. Additionally, an argument can be made for a broad transition that atoms are optically pumped out of states that cannot be trapped into

states that can quickly due to the large number of scattering events [72]. As a result, averaging over many photon absorption processes yields an overall restoring force enabling magneto-optical trapping. Indeed, experimentally it was found that a fermionic strontium MOT on the $^1P_1 \rightarrow ^1 S_0$ transition can be realized with the same life time as the bosonic MOT in the standard six-beam configuration.
However, things change for the single-beam geometries discussed in this section. We have seen that the secondary beams forming an oblique angle with the symmetry axis of the quadrupole field couple to σ^-, σ^+ as well as π transitions with the latter being vital for a restoring total force. For π transitions driven by the secondary beams and σ^+ transitions driven by the incident beam, the ratio of the Clebsch-Gordan coefficients giving the transition strength is less beneficial for the outer Zeeman sublevels. For the Zeeman sublevel $m_F = \pm - 9/2$ of the ground state the ratio is given by $10:1$ instead of $55:1$ as previously for pure σ^-/σ^+ coupling. Additionally, upon excitation to the Zeeman sublevel $m_F' = \pm 9/2$ of the excited state via a π transition, the atom can decay to the Zeeman sublevel $m_F = \pm 7/2$ so that spin polarization is likely significantly worse. The consequences for the atom dynamics in the MOT are complex and require a complex Monte-Carlo simulation or experimental investigation. We will see later that fermionic strontium was successfully trapped in the Fresnel-MOT.

2.5.2 *Narrow-line MOT*

The $^3P_1$ state used for 2nd stage cooling again has three hyperfine states with $F = \{7/2, 9/2, 11/2\}$ where the $F = 11/2$ state is used for cooling and trapping. Unlike in the 1st stage MOT, the hyperfine structure is resolved: The $F = 9/2$ and $F = 7/2$ state are shifted by more than a GHz away from the $F = 11/2$ state. We also find that the photon recoil shift is on the same order of magnitude as the transition linewidth so that the atom will only stay in resonance with the red-detuned laser beams for a few scattering events. Thus, we can no longer rely on fast randomization through optical pumping to solve the issue of Zeeman sublevels that cannot be confined. Indeed, it was found that the lifetime of the fermionic narrow-line MOT is drastically reduced compared to the bosonic narrow-line MOT [72]. To overcome the limitation in lifetime, a second so-called stirring laser is used to drive the $F_g = 9/2 \rightarrow F_e = 9/2$ transitions. This scheme was first introduced by the Tokyo group [72]. The Zeeman shifts for this hyperfine level are significantly smaller so that the atoms stay in resonance longer. This stirring laser then provides additional optical pumping and resulting state randomization. This scheme allows for the same narrow-line MOT lifetime for fermionic strontium as for bosonic strontium.
However, the consequences for a single-beam geometry where the

secondary beams form an oblique angle with the symmetry axis of the magnetic field discussed for the strong transition also apply here. Again, a detailed Monte-Carlo simulation and experimental investigation is needed to understand how the atom dynamics in the trap are changed. A group at the University of Maryland has started this investigation and found that in principle, operation of a red ^{87}Sr MOT should be possible but so far has not been able to prove this experimentally [26]. As we will see later, narrow-line cooling in the Fresnel-MOT was not attempted in this work due to a poor signal in the first stage MOT. Trap dynamics in the narrow-line MOT for ^{87}Sr for complex geometries thus remain an open question.

3

THE TEST SET-UP FOR TRAP CHARACTERIZATION

In this chapter, we present the test set-up built for the experimental characterization and investigation of the GMOT and the Fresnel-MOT. The focus of the set-up lies on facilitating a fast exchange of test structures, ample optical access for thorough investigation, and providing an easy possibility to realize a standard six-beam geometry as well. As a result some compromises were made with respect to an ideal geometry for GMOT and Fresnel MOT operation. The test set-up is presented in the following section as is a more detailed description of the home-built 689 nm laser set-up for narrow line laser cooling.

3.1 EXPERIMENTAL SET-UP

The test structure is mounted in an ultra-high vacuum system consisting of a standard spherical octagon. We choose to mount the grating such that gravitational acceleration is anti-parallel to the incident beam due to practical reasons such as easier alignment of the incident beam (configuration "chip up", see Chapter 2.4.4). As a result of the anti-trapping force impacting the SF MOT in this case as outlined in Chapter 2.4, this constitutes the "worst case" scenario. By operating in this configuration, the general feasibility of trapping on a narrow-line transition in the GMOT/Fresnel MOT geometry can be shown independent of orientation. This further supports functionality in micrograviy applications where atoms will again move between both potential barriers created by the GMOT/Fresnel MOT (see Chapter 6). The MOT coils are mounted in vacuum so that the reduced distance lowers the power consumption to reach the targeted gradient of up to 6 mT/cm. The coils have a distance of 26 mm and a radius of 14 mm with 16 windings each. We use currents of up to 10 A. The maximum gradient achievable is limited by heating and successive out-gassing of the coils. Additional coils outside the vacuum on both the radial axis and the z-axis allow compensation of external magnetic fields. The axial coils in z-direction also allow the application of an external magnetic field to shift the magnetic field zero of the quadrupole field towards the geometric center of the trapping volume.
The atom source is an oven following [97] heated to typically 350 °C – 400 °C. The atomic beam is radially incident to the center of the vacuum chamber. This leaves the z-axis available for the realization of a six-beam MOT which proved useful throughout the experimental characterization of the Fresnel MOT and the two-color GMOT. How-

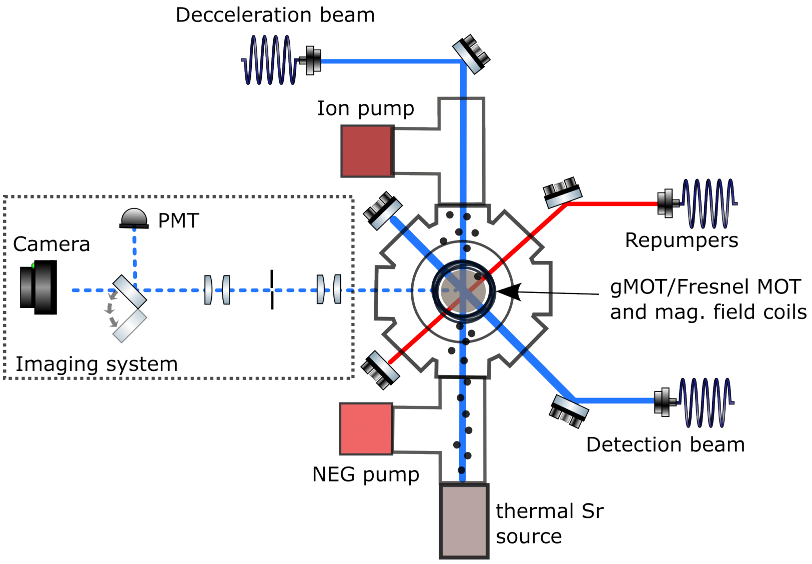

Figure 21: Experimental Set-Up of the test chamber with beam paths outlined. Details can be found in the text. NEG – nonevorable getter pump, PMT – photo-multiplier tube.

ever, the capture velocity in this direction is lower than in loading geometry along the z-axis (see Sec. 5.2.1) as realized by Sitaram et al. [100].

While most set-ups commonly use a Zeeman slower to initially slow higher velocity classes to velocities smaller than the capture velocity, we do not employ such a scheme. Instead, we use a deceleration beam counter-propagating the atom beam with a detuning of $-220\,\mathrm{MHz}$, a diameter of $3\,\mathrm{mm}$, and $20\,\mathrm{mW}$ power corresponding to a saturation of $s = 0.5$. The optimal detuning was found experimentally and depends on the intensity of the deceleration beam. The distance between the oven and the MOT center is $14\,\mathrm{cm}$, facilitating a high atom flux at the MOT position which partially compensates the lower portion of slow atoms.

The system utilizes two vacuum pumps, an $80\,\mathrm{l/s}$ nonevaporable getter (NEG) pump positioned directly at the oven and a $40\,\mathrm{l/s}$ ion pump positioned on the opposite side of the vacuum chamber. The NEG pump was added to the set-up to counter strong outgassing of the oven that led to a pressure increase to the $10^{-8}\,\mathrm{mbar}$ range as no differential pumping is employed. The base pressure of the system is $2 \cdot 10^{-10}\,\mathrm{mbar}$. Outgassing from the oven continued to limit the vacuum pressure to $5 \cdot 10^{-9}\,\mathrm{mbar}$ at an operational temperature of $390\,^{\circ}\mathrm{C}$.

Due to decay via the $^1D_2$ to the metastable $^3P_2$ state, the $^1S_0 \rightarrow {}^1P_1$ transition is not closed, and atoms can get trapped in this so-called dark state. This is solved by using a repumping scheme: Here, we use a first repumper that excites the atoms from the $^3P_2$ dark state to the $^3S_1$ state. As the atom may decay into the $^3P_0$ state from there, a second repumper is used on the $^3P_0$ to the $^3S_1$ transition (see Fig. 1) [29]. This way, atoms will eventually decay from the $^3S_1$ state to the $^3P_1$ state and from there to the ground state. For fermionic strontium, the hyperfine splitting affects the repumping scheme. The $^3P_2$ state has five hyperfine states with $F = \{5/2, ..., 13/2\}$. Similarly, the $^3S_1$ state has three hyperfine states with $F = \{7/2, 9/2, 11/2\}$. The hyperfine states of both the $^3P_2$ state and the $^3S_1$ state span a frequency range of a few GHz each. To be able to address all of these transitions, as repumping efficiency otherwise drastically decreases [17], the repumpers are modulated rapidly in frequency.

For the first cooling stage at 461 nm, as well as for the repumping at 679 nm and 707 nm light, commercially available extended cavity diode lasers (ECDL) are used. Two 461 nm lasers are used, one producing the light for the incident MOT beam while the other provides the deceleration beam and a detection beam. All diode lasers are locked to a wavelength meter with a resolution of 0.1 MHz. Laser light with a narrow linewidth for the second cooling stage at 689 nm is generated with a home-built laser system detailed in the following section.

A dichroic mirror combines the 461 nm and 689 nm light. A beam shaping unit consisting of a variable telescope followed by a flat-top beam shaper produces an 18 mm diameter bichromatic laser beam with flat-top intensity profile and circular polarization. The profile of the output beam can be adapted by changing the input diameter with the variable telescope, which allows fine-adjustment of the intensity profile.

The repumpers are radially incident on the atoms with a retro-reflected beam as depicted in Fig. 21. Another radial axis is used for the retro-reflected detection beam.

To optimize imaging, we use an imaging system consisting of a lens with a focal length $f = 125\,\text{mm}$ that initially collimates the fluorescence light from the detection beam. A pair of lenses with $f = 100\,\text{mm}$ produces an intermediate focus where an aperture is placed to filter out stray light. Finally, another lens with $f = 100\,\text{mm}$ focuses the light. A flip mirror allows to select between imaging onto a CCD camera or a photo-multiplier tube (PMT).

3.2 689 nm LASER

For excitaton of the narrow-line transition, locking of a diode laser on the wavelength meter does not suffice to fulfill requirements of a stable, narrow-line light source. Instead, an in-vacuum cavity is used as absolute frequency reference. As free running laser diodes typically have a spontaneous linewidth of MHz, the linewidth of the laser diode used is initially narrowed with a self-injection lock to ensure good coupling to the cavity mode and feasibility of a stable Pound-

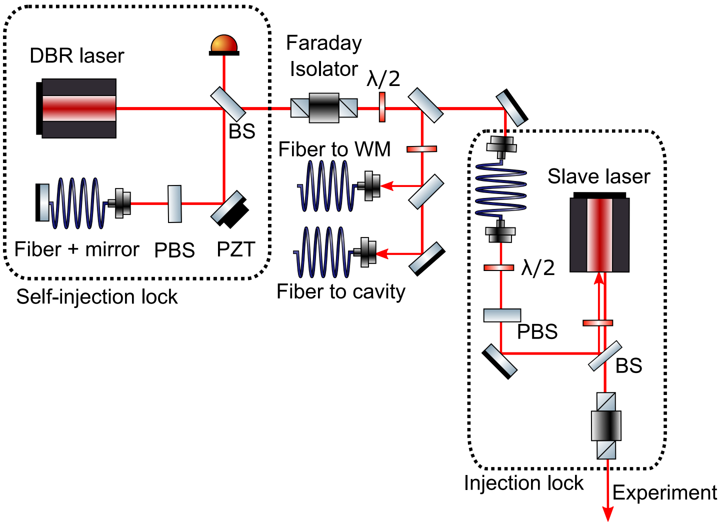

Figure 22: Home-built laser set-up for generation of narrow-line, single frequence laser light at 689 nm. A single-frequency laser diode is self-injection locked and employed as a master laser. A lock to an in-vacuum optical resonator ensures long-term frequency stability with feedback loops to a piezo in the self-injection path and the laser current. A high-power slave laser diode is injection locked to this master laser.

Drever-Hall (PDH) lock.

The laser system used for generation of 689 nm light is based conceptually on previous work by Lin et al. [55]. The set-up is depicted in Fig. 22. A single-frequency laser diode by Eblana photonics is used as master laser. The laser diode is temperature-stabilized to a temperature of 30.4°C to reach the wavelength of the $^1S_0 \rightarrow {}^3P_1$ intercombination line in ^{88}Sr and operated at a current of 94 mA. A pick-off reflects 5% into the self-injection locking arm consisting of a mirror mounted on a piezo, a polarizing beamsplitter (PBS) and a 1 m single-mode fibre with a mirror on its end for retro-reflection. The PBS in front of the fiber allows to control the fraction of the light that will be reflected back into the single-frequency laser diode. The light then passes through an optical isolator to avoid back reflection from other surfaces. A sequence of λ/2 waveplates and PBS controls the fraction of the light passed to the slave laser, wavelength meter, and an in-vacuum optical resonator serving as absolute frequency reference to achieve long-term frequency stability. A PDH locking scheme to a sideband with tunable offset-frequency from the carrier allows fine-tuning of the laser frequency. A slow feedback loop passes the error signal to the piezo in the self-injection path and a fast feedback loop passes the error signal to the laser current.

Different regimes are observed, depending on the feedback level chosen. For feedback around −43 dB, we observe line narrowing and single-mode operation. Reducing the feedback further leads to a regime where the linewidth is broadened significantly, while increasing the feedback leads to multi-mode operation. These observations correspond to the observations of Lin et al. [55]

The frequency reading on the wavelength meter with a resolution of 100 kHz was stable on relevant time scales (with an exposure time of few µs).

For more details on the underlying physics of the self-injection lock, the interested reader is pointed to Ref. [2, 42, 106]

To increase the laser power available at the experiment, we employ an injection lock to a high-power slave laser diode which then inherits its spectral properties from the self-injected locked single-frequency laser diode used as master laser. The feedback level used in the injection lock is controlled with a half-wave-plate and a PBS. The light from the master laser is reflected into the slave laser diode via a beam pick-off plate. The maximum power available at the experiment is 15 mW.

4

A PLANAR, ACHROMATIC FRESNEL MOT

This chapter presents the novel Fresnel MOT. In the first section, its design is presented followed by the experimental characterization in the test set-up.

4.1 DESIGN

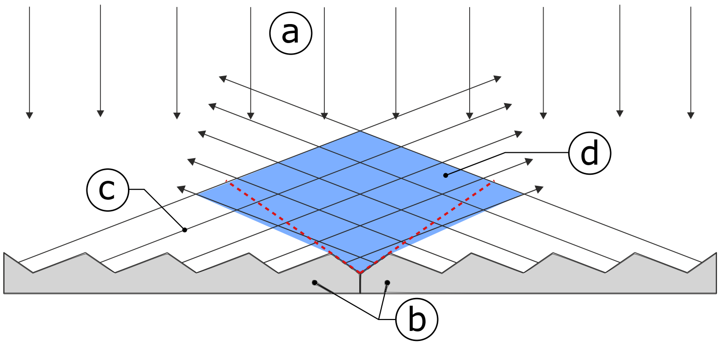

Figure 23: Schematic illustration of the beam propagation in the Fresnel MOT. The incident beam (a) is reflected by the Fresnel reflector (b), creating secondary beams (c). Adding a magnetic quadrupole field with its minimum within the beam overlap volume (d) leads to cooling and trapping of atoms. The red dashed lines show the equivalent mirror surfaces of a tetrahedral MOT (see Fig. 2) producing an equivalent beam geometry.

The basic idea of the Fresnel MOT is to combine the advantages of the tetraeder MOT and the gMOT (see Chapter 1.3) into one planar reflector that allows the formation of a magneto-optical trap from a single incident beam in combination with a quadropole field. Such a reflector combines the unrestricted radial access and the mechanical stability that the gMOT offers with the achromatic beam steering of reflective designs. To realize this, the bulky mirrors of the tetrahedral mirror MOT are replaced with surface-structured Fresnel reflectors. This structure is obtained by folding the surfaces of the tetrahedral mirror MOT in regular intervals onto a common plane. Surfaces reflecting towards the center of the trap that participate in cooling and trapping of the atoms then alternate with surfaces reflecting the incident light outwards. The latter are ideally parallel to the secondary MOT beams to avoid multiple reflections as this may cause intensity imbalance with additional reflected beams passing trough the trapping volume.

The period of the structure is in principle arbitrary as long as it is

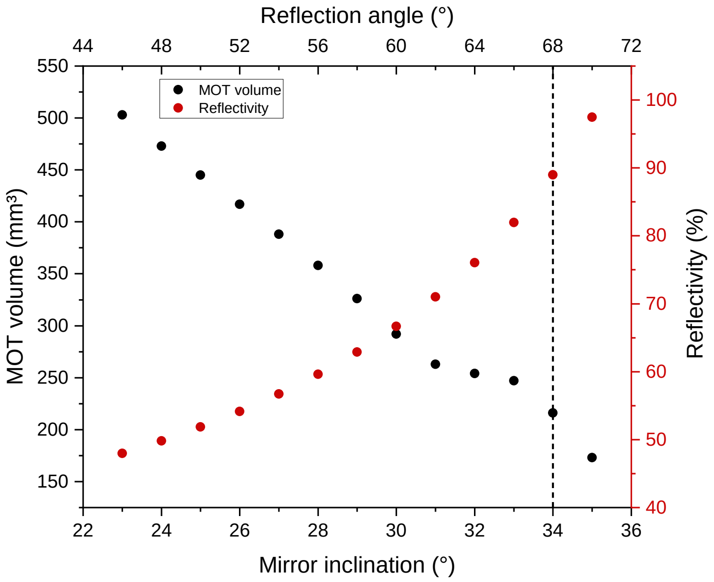

Figure 24: Reflectivity needed for balanced radiation pressure and MOT volume as a function of mirror inclination angle/reflection angle. The MOT volume has been determined numerically, while the reflectivity is calculated according to $R = \frac{1}{N\cos\theta}$. The black dashed line indicates the mirror inclination/reflection angle for the Fresnel structure.

large compared to the wavelength employed thus avoiding diffraction. It dictates the height of the structure. In the limit of very large periods, this yields the tetrahedral MOT. A schematic drawing of the Fresnel MOT design is depicted in Fig. 23

The idea has been patented with patent no. 10 2020 102 222 at the Deutsches Patent- und Markenamt (DPMA) [11].

A first-generation prototype has been designed and manufactured from oxygen-free copper by the scientific instrumentation department at PTB. This material is well-suited as a surface with optical quality can be achieved by high precision milling processes without additional polishing necessary. A surface root-mean-square roughness of the copper substrate of $\approx 7\,\mathrm{nm}$ was obtained this way. The copper substrate was sputter-coated with a $100\,\mathrm{nm}$ aluminum layer yielding a highly reflective surface for visible radiation. Both copper and aluminum are conductive. The use of dielectric materials may be prone to the accumulation of charges yielding an electric field which in turn results in a large, varying DC-Stark frequency shift for the clock transition [16] – a problem for high-accuracy quantum sensors using spectroscopy of the clock transition.

In principle, the inclination angle can be freely chosen for this type of structure. However, as we have seen previously, a tetrahedral configuration corresponding to a mirror inclination angle of $\gamma = \theta/2 = 35.26°$ is ideal and requires a reflection coefficient of 1 for intensity balance.

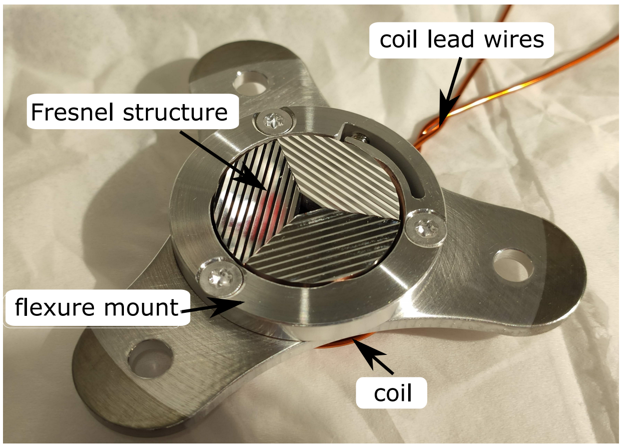

Figure 25: Photographic image of the Fresnel structure prototype. The prototype is manufactured from oxygen-free, high-conductivity copper and sputter-coated with a 100 nm aluminum layer. The inlination angle of the inward reflecting surfaces is 34 degrees.

The reflectivity necessary for intensity balance, $R = \frac{1}{3\cos\theta}$, is presented as a function of mirror inlination/reflection angle in Fig. 24. Aluminum has a reflection coefficient of ≈ 0.9 for visible radiation. To obtain balanced radiation pressure, this yields a mirror inclination angle of $\gamma = 34°$, close to the ideal tetrahedral configuration.

Figure 24 shows further how the MOT volume, i.e. the overlap volume of the incident beam and all secondary beams, scales with mirror inclination angle/reflection angle. The atom number N has been shown to scale with the trap volume in MOTs. However, realizing a configuration with (almost) ideal trapping and cooling coefficients takes precedence as their impact on atom number and final temperature dominates.

The Fresnel structure prototype is shown in Fig. 25. The structure has a diameter of 25.4 mm and consists of three distinct segments. A triangle-shaped hole is in the center of the sample structure to avoid parasitic reflection and allow for the formation of a standard six-beam MOT with the structure in the test chamber. The Fresnel MOT is placed in a flexure mount that also holds one of the in-vacuum magnetic field coils.

4.2 EXPERIMENTAL CHARACTERIZATION

The prototype of the Fresnel MOT was characterized in the test set-up described in the previous chapter. Aligning the incident beam proved challenging as no retro-reflection is available for easy alignment. Radial support beams were employed to obtain an initial signal. Their intensity was then slowly reduced under constant realignment and optimization of the fluorescence signal until stable trapping with the Fresnel MOT alone was achieved. The results of the experimental characterization of 1^{st} and 2^{nd} stage MOTs of ^{88}Sr as well as 1^{st} stage cooling of ^{87}Sr and ^{86}Sr are presented in the following.

4.2.1 1^{st} *Stage Cooling of* ^{88}Sr

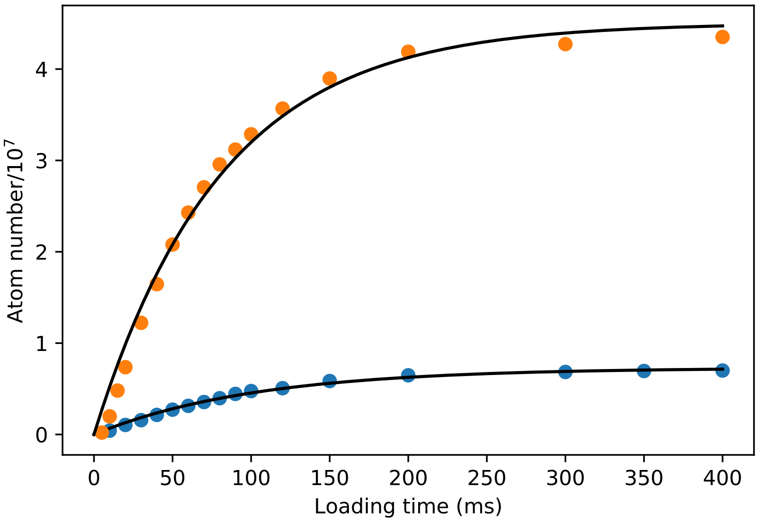

Figure 26: Typical loading curve of the 1^{st} cooling stage Fresnel MOT with (orange) and without (blue) deceleration beam. The magnetic field gradient is $dB/dz = 7.2\,\mathrm{mT/cm}$ and the laser intensity $s = 0.5$. Error bars are smaller than the size of data points and thus not visible.

We successfully trapped and cooled ^{88}Sr atoms on the 1^{st} cooling transition with the Fresnel structure. In order to characterize the Fresnel MOT, we measure the life time τ and the temperature T of the atoms as well as the atom number N and the loading rate R. All of these but the temperature can be extracted from loading curves, where the atom number is recorded as a function of time t while the MOT is loading. Each data point presents the average atom number after repeatedly loading the MOT for a time t and subsequent detection. The error corresponds to the uncertainty on the mean atom number. Here, we extract the atom number from fluorescence imaging.

Throughout experiments with the Fresnel MOT as well as the gMOT, we observe that the deceleration beam contributes a significant radiation pressure to the 1^{st} stage MOT resulting in intensity imbalance and a decreased lifetime. Thus, the loading curves for life time characterization are recorded with the deceleration beam turned off and the MOT being loaded directly from the hot atom beam. Where light-assisted collisions can be neglected, the atom number during loading then follows

$$N = \underbrace{R\tau}_{N_0}\left(1 - \exp\left(\frac{t}{\tau}\right)\right) \tag{34}$$

where N_0 denotes the steady-state atom number. In Fig. 26, a typical loading curve is presented, recorded with a magnetic field gradient of $dB/dz = 7.2\,\text{mT/cm}$ and an intensity of the incident beam of $s = 0.5$. As in Ref. [100], we conclude from the quality of the fit that the above assumption of negligible light-assisted collisions is valid. For comparison, a loading curve with deceleration beam turned on using the same parameters is also presented. Here, the loading rate is improved dramatically, and we further observe a reduction of life time. Overall, this still results in a significantly higher equilibrium atom number $N_0 = R\tau$.

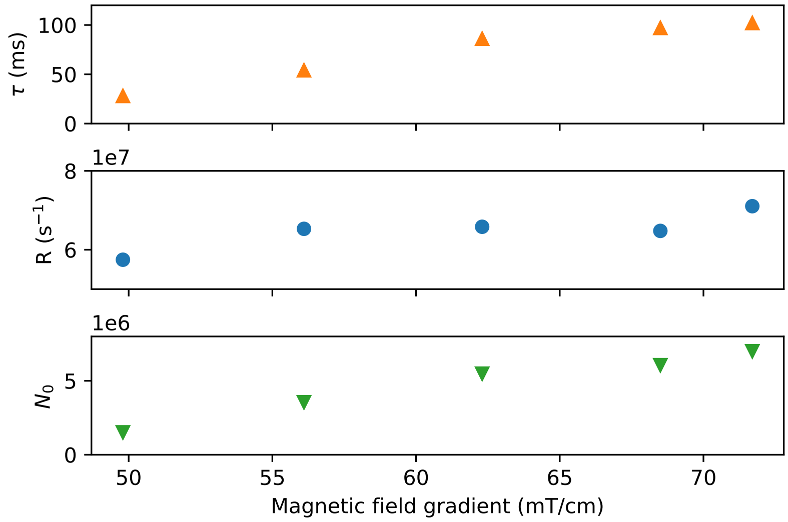

Figure 27: Life time, loading rate and atom number as a function of magnetic field gradient. The intensity of the incident MOT beam is $s = 0.5$ and the vacuum pressure is $5 \cdot 10^{-9}$ mbar. The uncertainty is taken from the fit and corresponding error bars are smaller than the size of data points and thus not visible.

Figure 27 shows the parameters life time, atom loading rate and atom number as functions of the magnetic field gradient. They all increase with increasing magnetic field gradient. The life time increases from 28 ms to 102 ms. The vacuum pressure during these measurements was measured as $5 \cdot 10^{-9}$ mbar corresponding to a background-gas-collision limited lifetime of 200 ms [73]. Assuming $\frac{1}{\tau_{vacuum}} + \frac{1}{\tau_{FMOT}} = \frac{1}{\tau_{total}}$, a lifetime of up to $\tau_{FMOT} = 208$ ms is obtained. The loading rate shows a much weaker dependency on magnetic field gradient than the life time and is nearly constant from 5.5 mT/cm to 6.9 mT/cm. This is in agreement with expectations of a weak dependency on magnetic field gradient from simulations. The behavior of the equilibrium atom number is dominated by the effect of the increasing life time.

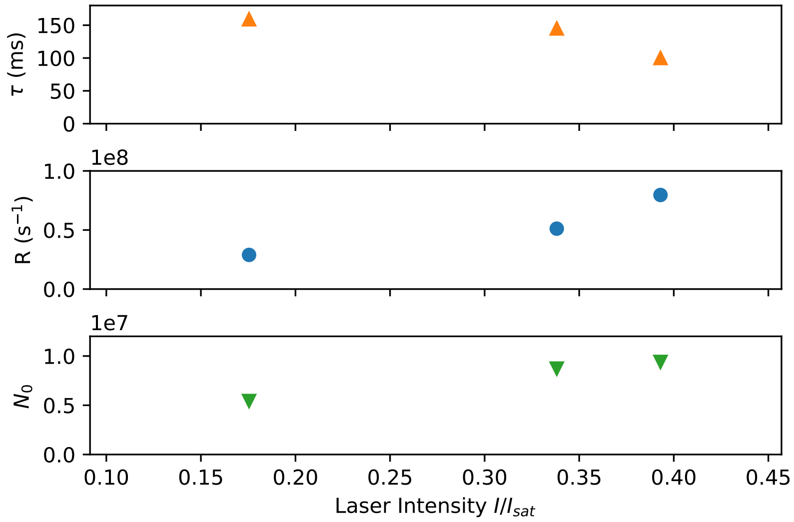

Figure 28: Life time, loading rate and atom number as a function of laser intensity. The magnetic field gradient is $dB/dz = 7.2$ mT/cm and the vacuum pressure is $5 \cdot 10^{-9}$ mbar. The uncertainty is taken from the fit and corresponding error bars are smaller than the size of data points and thus not visible.

Figure 28 shows the parameters life time, atom loading rate and atom number as a function of laser intensity of the incident MOT beam during loading. Loading rate and atom number both increase with increasing intensity, while the life time decreases. An increase in loading rate is readily understood and also observed in standard geometries [116]. The decrease in life time from 160 ms to 100 ms however is surprising. Assuming again $\frac{1}{\tau_{vacuum}} + \frac{1}{\tau_{FMOT}} = \frac{1}{\tau_{total}}$, a lifetime of up to $\tau_{FMOT} = 800$ ms is obtained at $s \approx 0.18$ so that the dependency of lifetime on laser intensity is even stronger than apparent at first glance. Closer investigation reveals that the atoms are significantly hotter for increasing laser intensities. With atoms moving faster, they are more likely to be able to escape the MOT between entering a dark state and being repumped and returned to the cooling cycle.

To measure the temperature of the atom cloud, we use the time of flight (TOF) technique. Here, the width of the freely expanding atom cloud is recorded as a function of time with fluorescence imaging. The width σ of the atom cloud is

$$\sigma^2(t) = \sigma_0^2 + (k_B T/M) \times t^2 \tag{35}$$

where σ_0 is the initial size of the atom cloud at $t = 0\,\mathrm{s}$. Recording the size of the atom cloud as a function of expansion time t then allows to extract the temperature from a fit following the equation above.

The temperature is measured as a function of intensity where the MOT is initially loaded with the MOT beams at full intensity and the deceleration beam on. The intensity is then quickly ramped to the target intensity and the deceleration beam turned off. After the atom cloud is thermalized, the MOT beam is then also turned off and the atom cloud expands for a time interval t before detection on the camera where the atoms are illuminated with the retro-reflected detection beam. Its exposure time is chosen as small as possible while still yielding a good signal. Longer exposure times were observed to cause artifacts as a systematic error on the temperature results from the atom cloud continuing to expand during exposure. The atom cloud width is extracted from the fluorescence images with a Gaussian fit. To improve the SNR, pixels are binned in vertical/horizontal direction to extract horizontal/vertical cloud size.

Figure 29 a) shows an exemplary plot of the extracted atom cloud widths as a function of time for axial and radial direction corresponding to the lowest point in Fig. 29 b) with an intensity $s = 0.057$. This yields a temperature of $(3.87 \pm 0.10)\,\mathrm{mK}$ in the axial direction and $(4.28 \pm 0.12)\,\mathrm{mK}$ in radial direction where the error corresponds to one standard deviation. The ratio of radial to axial temperature agrees with the theoretical ratio obtained from Eq. 31 of 1.09 within one standard deviation. However, it is four times the theoretical Doppler cooling limit for this configuration. The temperature increases further with increasing intensity for both radial and axial direction. In axial direction, the temperature increases to $7\,\mathrm{mK}$ at $I = 0.4\,I_{sat}$ with a steeper increase in radial direction to $12\,\mathrm{mK}$. According to Doppler theory, the temperature increase expected with intensity should be much weaker.

Similar behavior is also observed in the standard six-beam geometry for alkaline-earth atoms [57, 76, 116, 117]. The underlying cause was identified by Chanelière et al. as intensity fluctuations transverse to the propagation direction of the laser beams leading to an additional heating mechanism [19]. They found that an additional, constant force results from intensity fluctuations, adding to the friction

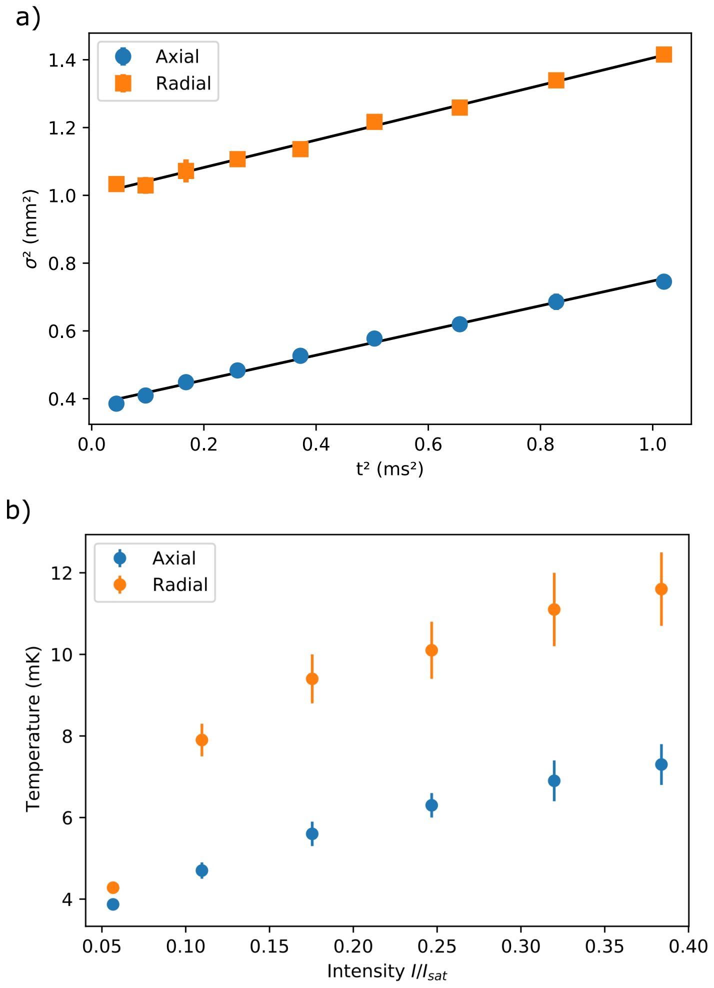

Figure 29: a) Atom cloud size squared as a function of time squared for a laser intensity of $I = 0.06\,I_{sat}$. This measurement corresponds to the lowest intensity point in the graph below. b) Temperature in the 1st stage Fresnel MOT as a function of laser intensity. The magnetic field gradient is $dB/dz = 0.72\,mT/cm$ and the laser detuning $\Delta = -\Gamma$.

force from Doppler theory. Intensity fluctuations in the Fresnel MOT in particular can result from imperfection in the top-hat intensity profile of the incident beam, misalignment, as well as manufacturing imperfections e.g. in the form of varying reflectivity of the surfaces and at the edges between the adjacent surfaces that can result in wavefront errors and parasitic reflection. In the absence of sub-Doppler cooling processes as it is the case for ground states with zero angular momentum, the additional force resulting from intensity fluctuations dominates for small velocities. The final velocity distribution of the atom cloud then depends on the ratio of the time scales of the intensity fluctuations and cooling to steady-state. This effect scales with intensity and temperatures closer to the theoretical Doppler limit can be obtained by reducing the intensity of the cooling beams accordingly.

For alkaline atoms with sub-Doppler cooling mechanisms present, the friction force becomes intensity independent and the effect of the intensity-dependent, constant force resulting from intensity fluctuations thus becomes negligible.

These considerations are further supported by the positive impact of a high magnetic field gradient on the trapping characteristics as this compresses the atom cloud further, limiting the number of segments of the periodic Fresnel structure needed for trapping and cooling.

While intensity fluctuations are likely to limit the temperature, atoms are cooled sufficiently to be transferred to a BB MOT with good efficiency when the intensity of the cooling beams is lowered, yielding colder temperatures so that the first stage Fresnel MOT fulfills its purpose. However, this does reduce the loading rate and atom number as well.

Suggested improvements for the Fresnel MOT are 1) the addition of a plane ring around the Fresnel structure for easier alignment of the incident beam, 2) choosing a period as large as conveniently possible so that the volume of cold atom cloud obtained after first stage cooling can be illuminated with a minimal number of segments and 3) an improved milling and coating process yielding a higher surface quality and improved reflective properties. Figure 30 depicts the atom number signal as a function of detuning. The maximum number of atoms is trapped with the incident beam red-detuned by one linewidth. This is in agreement with the typical detuning in the standard six beam configuration. The full width at half maximum (FWHM) of the atom number peak is $0.4\,\Gamma$.

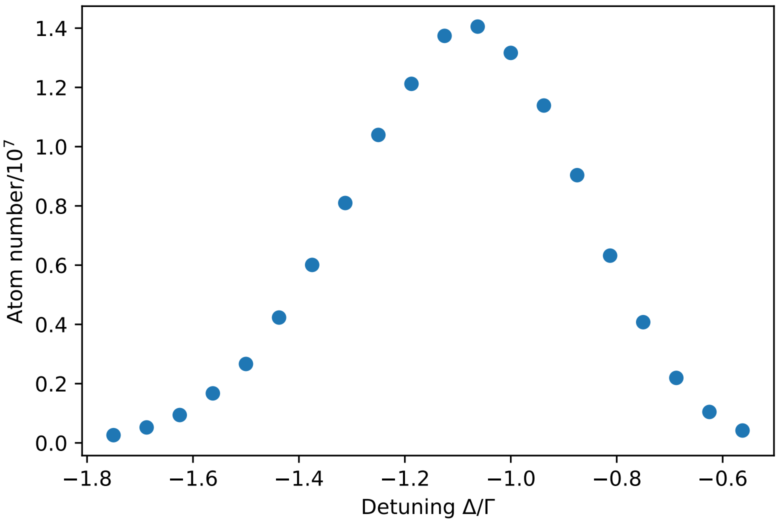

Figure 30: Number of ^{88}Sr atoms in the 1^{st} stage MOT as a function of detuning. The magnetic field gradient is 7.2 mT/cm and the laser intensity is $s = 0.5$. Error bars correspond to the size of the data points.

4.2.2 2^{nd} *Stage Cooling of* ^{88}Sr

After loading and cooling in the first stage MOT, the 689 nm laser is turned on at full power. The laser linewidth is broadened to 1.6 MHz using a modulation frequency of 50 kHz. The intensity of the 1^{st} stage cooling laser is then ramped down linearly to $s = 0$ and the magnetic field gradient switched to 0.3 mT/cm. In this BB MOT, the atoms are cooled for an additional 60 ms. The transfer to the BB MOT is improved by reducing the intensity of the first stage cooling laser already during initial loading to $s = 0.3$, yielding a transfer efficiency of 50%.

The temperature of the atom cloud after cooling in the BB MOT is again determined with the TOF method. The atom cloud size in radial and axial direction as a function of wait time t before detection is presented in Fig. 31, where data is averaged over several subsequent measurements. The error bar for each data point corresponds to one standard deviation on the mean value. Evaluation yields an axial temperature of (25 ± 3) µK and a radial temperature of (43 ± 4) µK.

It can be expected that atoms could be cooled further as demonstrated in the gMOT in the following chapter by applying a SF phase where the modulation is switched off and intensity reduced linearly.

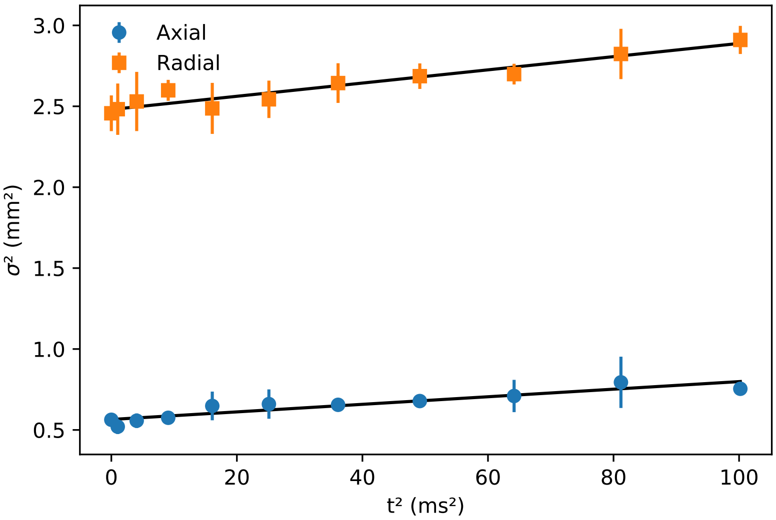

Figure 31: Temperature measurement of the atom sample after cooling in the BB MOT. The laser intensity is $s = 1000$ and the laser linewidth is broadened to 1.6 MHz. The magnetic field gradient is 0.3 mT/cm. The linear fit yields an axial temperature of (25 ± 3) µK and a radial temperature of (43 ± 4) µK.

4.2.3 1^{st} *Stage Cooling of* ^{87}*Sr and* ^{86}*Sr*

Besides ^{88}Sr, we have also captured the fermionic isotope ^{87}Sr as well as ^{86}Sr. The abundances and isotope shifts of the four stable isotopes of strontium are listed in Tab. 2. No attempt was made to capture ^{84}Sr due to the low abundance. In Fig. 32, the atom number is depicted as a function of frequency of the MOT beams. Here, we have used the frequency with the maximal atom number for ^{88}Sr as reference. The data for ^{88}Sr corresponds to the data from Fig. 30. Data for ^{87}Sr and ^{86}Sr was recorded at an oven temperature of 390°C and a vacuum pressure of $8 \cdot 10^{-9}$ mbar. The fluorescence image for ^{88}Sr is recorded with an exposure time of 100 µs. For ^{87}Sr and ^{86}Sr, the images were recorded with an exposure time of 300 µs to improve the signal to noise ratio (SNR). Additionally, the images are averaged over a recorded sequence of fluorescence images and an averaged background sequence is subtracted for all isotopes.

The frequency shift between the ^{87}Sr and ^{86}Sr isotope to the ^{88}Sr isotope is in agreement with the isotope shifts of −46.5 MHz and −124.8 MHz, respectively. We further observe that, while ^{86}Sr and ^{87}Sr have a similar abundance, the ^{87}Sr peak in the spectrum is much weaker. One possible reason is insufficient power in the repumping beams as the laser needs to be scanned over several GHz to cover all hyperfine states. While this is a challenge that also presents itself in the standard six-beam geometry, additional problems might arise from nature of the geometry as outlined in Sec. 2.5. Additionally, it was previously observed that collisions with ^{88}Sr atoms from the hot atom beam can limit the ^{87}Sr MOT [17] which might also be a problem here.

ISOTOPE	ABUNDANCE	NUCLEAR SPIN	ISOTOPE SHIFT
^{84}Sr	0.56%	0	−270 MHz
^{86}Sr	9.9%	0	−124.8 MHz
^{87}Sr	7.0%	9/2	−46.5 MHz
^{88}Sr	82.6%	0	(reference)

Table 2: Natural occurring isotopes of strontium. The isotope shift is given for the $^1S_0 \rightarrow ^1P_1$ transition with respect to ^{88}Sr.

Furthermore, the ^{87}Sr MOT required a shift of the magnetic field zero away from the Fresnel structure with respect to ^{86}Sr and ^{88}Sr which was realized by reoptimzing the current in the compensation coils. This is possibly a consequence of the non-trivial trap dynamics discussed previously. This phenomenon has also been observed by the Maryland group [27].

2^{nd} stage cooling for fermionic Strontium was not attempted due to the poor signal to background ratio obtained for 1^{st} stage cooling.

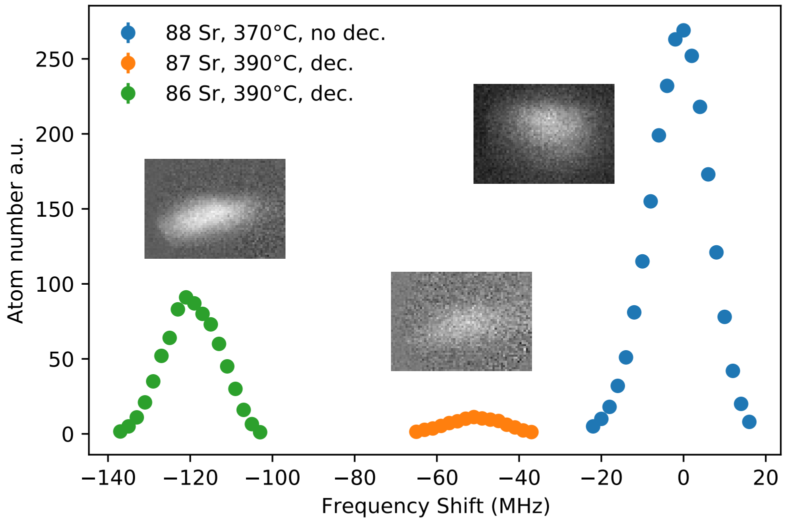

Figure 32: Atom number as a function of laser detuning for ^{88}Sr, ^{87}Sr, and ^{86}Sr. The frequency detuning is given relativ to the laser frequency yielding the maximum number of ^{88}Sr. Data for ^{88}Sr are recorded at an oven temperature of 370°C with the deceleration beam turned off. Data for ^{87}Sr and ^{86}Sr are recorded at an oven temperature of 390°C with the deceleration beam turned on. Fluorescence images of the atom cloud for each isotope at optimal detuning are shown as insets where the atom cloud is illuminated with the retro-reflected detection beam. The exposure time is 100 µs for ^{88}Sr and 300 µs for ^{87}Sr and ^{86}Sr. Error bars are smaller than the data point markers and thus not visibe.

5

A TWO-COLOR GRATING MOT

While the design of a grating for the trapping of ^{88}Sr is discussed here in particular, a majority of the considerations can be transferred to grating designs for other elements. We will first look at the design process, then move on to present the final design followed by simulations of capture velocity as well as temperature and conclude with its experimental characterization.

5.1 DESIGN PROCESS

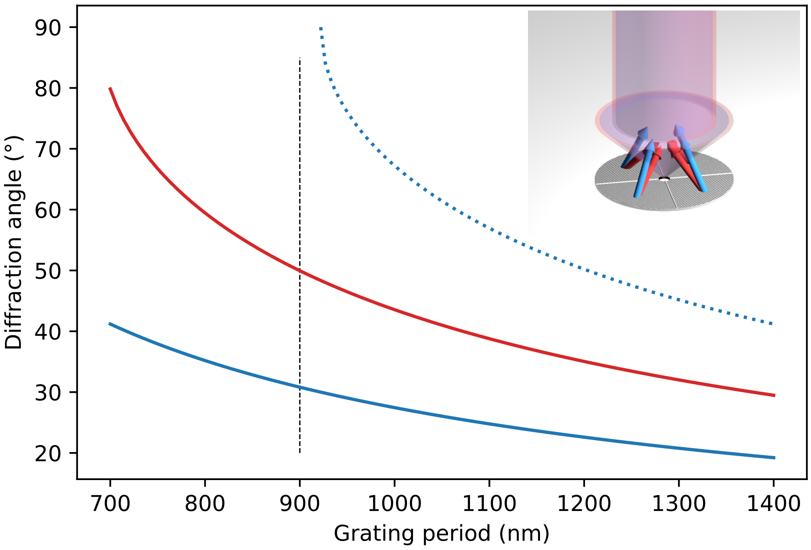

Figure 33: Diffraction angle as a function of grating period for 1st order diffraction of 461 nm (blue) and 689 nm (red) as well as 2nd order diffraction of 461 nm (blue dashed). The black vertical line indicates the grating period of the final design used in this work.

A diffracting grating with grating period d diffracts light with wavelength λ which is normally incident according to $\lambda = d \cdot \sin(\theta)$. Figure 33 shows the diffraction angle as a function of grating period for 1st order diffraction of 461 nm (blue) and 689 nm (red) as well as 2nd order diffraction of 461 nm (blue dashed). The inset again illustrates the angle dispersion of the diffraction grating.
This wavelength dispersion of the angle of diffraction in combination with the wavelength dispersion of the diffraction efficiency constitutes a number of design challenges: Firstly, the trapping volume

formed by the incident beams and the diffracted beams, in which the intensity-weighted k-vectors add to zero, will be axially shifted for different wavelengths. A small overlap of trapping volumes for first and second stage cooling challenges transfer from the first to the second cooling stage in the magneto-optical trap. Secondly, an ideal diffraction efficiency is difficult to achieve simultaneously for two transitions with a large wavelength ratio. Thirdly, the optimal diffraction angle cannot be chosen for both wavelengths. And lastly, we would like to suppress 0^{th} order diffraction as it results in an anti-trapping force and an unbalanced radiation pressure, which again is not trivial for two wavelengths as this is commonly achieved by choosing the grating height as $\lambda/4$. How these challenges can be overcome will be the focus of this section.

With the grating period determining the diffraction angle, it is a key parameter in the design with influence on the sizes of the trap volumes, overlap of the trap volumes, radial and axial trapping as well as temperature, and finally the degree to which the desired diffraction efficiencies can be achieved. We will first look at angle dispersion and its consequences in detail and then at diffraction efficiency dispersion and infer the choice of grating period for this work.

5.1.1 *Wavelength Dispersion of the Diffraction Angle*

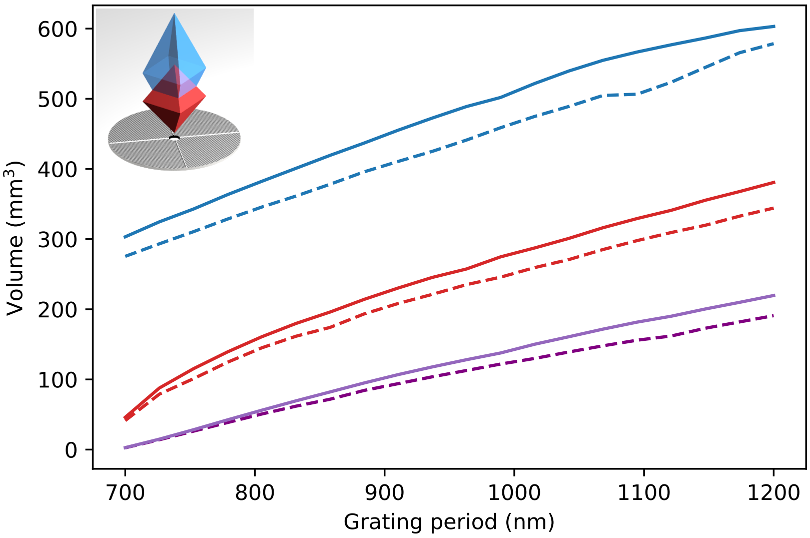

Figure 34: Trapping volume for the first (blue) and second (red) cooling stage transitions as well as overlap volume of both trapping volumes (purple) as a function of grating period. All trapping volumes are plotted for a three-part grating (solid) and a four-part grating (dashed) and a beam diameter of 18 mm as produced by the beam shaping unit of the test set-up.

Trap Volume

In Fig. 34, one can see that the trapping volumes, as well as their overlap, depend on the grating period and increase roughly linearly with increasing grating period. The inset illustrates the problem of a limited overlap of the trapping volumes resulting from the axial shift, with the trap volume of the blue first cooling stage further away from the chip than the trap volume of the second cooling stage. Typically, the atom number increases with trap volume so that large trap volumes are beneficial. An increase in the overlap of the trap volumes of first and second cooling stage should further improve the transfer efficiency. However, as the trap volumes also become increasingly elongated, the scaling of the atom number with trap volume is likely worse than for the standard six-beam geometry or the pyramid MOT. Changing the number of secondary beams from three to four leads to a minor decrease in trap volume and overlap volume.

Confinement and Trapping Characteristics

We have previously analyzed the angle dependency of the trapping constant κ_z and κ_{rad} for the first cooling stage yielding Eq. 24, where both benefit from larger diffraction angles as the anti-trapping contribution decreases. We have also analyzed the dependency of axial and radial restoring force on intensity imbalance, which is particularly relevant in this case due to the aforementioned wavelength dispersion of diffraction efficiency and resulting challenges regarding the optimization of diffraction efficiency to a target value for two wavelengths. Figure 35 shows the trapping coefficients κ_z and κ_{rad} as a function of diffraction angle/ grating period and intensity imbalance for an intensity of the incident laser beam of $s = 0.5$, magnetic field gradient of 5 mT/cm, and detuning $\Delta = -\Gamma$. We observe that for larger diffraction angles intensity balance becomes less critical for axial trapping. For small angles, intensity imbalance $\eta \neq 1$ rapidly results in a decreased trapping coefficient, especially for an increased diffraction efficiency ($\eta > 1$). Here, η denotes the previously introduced intensity imbalance parameter (see Sec. 2.3.2) where the intensity in the secondary beams I_j is given as $I_j = \eta \underbrace{\frac{1}{N\cos(\theta)}I_0}_{\substack{\text{“ideal”}\\ \text{Diffraction Efficiency}}}$.

The grating period needs to be larger than the wavelength for the second cooling stage in order to generate diffraction for this wavelength, too. As a result, grating periods that would produce an ideal angle for the first cooling stage and are relatively insensitive to intensity balance are not available. The diffraction angle for the first cooling stage is limited to $\theta < 42°$.

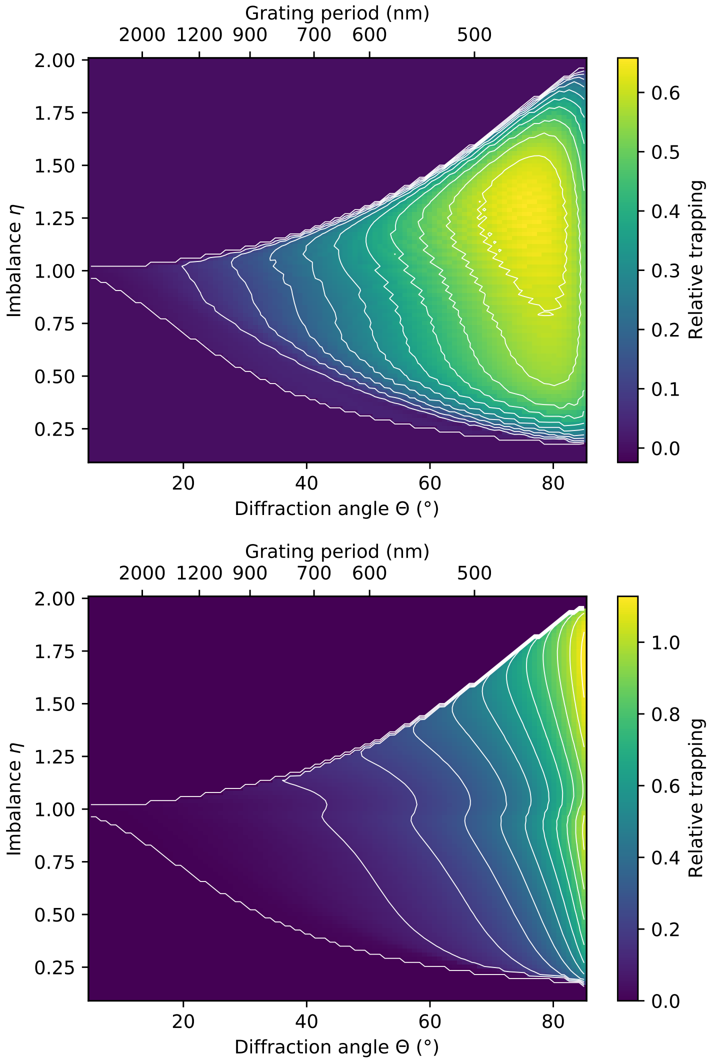

Figure 35: Axial (top) and Radial (bottom) trapping constant as a function of the intensity imbalance parameter η and the diffraction angle θ. The values for the trapping constant are given relative to the trapping constant in the standard, intensity-balanced six-beam geometry.

Temperature and Cooling Characteristics

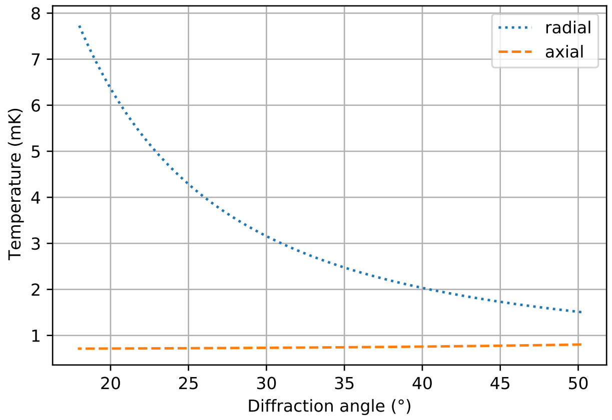

Figure 36: Axial (orange) and radial (blue) temperature in the 1^{st} cooling stage MOT as a function of diffraction angle/ grating period.

As we have seen in the previous theoretical discussion, the temperature in the Doppler cooling limit depends on the angle of the secondary beams with respect to the quantization axis. For the first cooling stage, the radial temperature decreases with increasing diffraction angle (and thus decreasing grating period) while the axial temperature increases with increasing diffraction angle (and decreasing grating period). The axial and radial Doppler temperatures as resulting from Eq. 31 are plotted as a function of grating period and diffraction angle in Fig. 36. While the axial Doppler temperature still remains below 1 mK for diffraction angles ranging between 20° and 50°, the radial Doppler temperature increases from ca. 1.5 mK at 50° diffraction angle and a grating period of 600 nm to ca. 6.5 mK at a diffraction angle of 18° corresponding to a grating period of 1400 nm. As hotter atoms are more challenging to transfer to the second cooling stage, a minimal temperature in both dimensions is desirable which in turn requires small grating periods.
For the second cooling stage, angles with $\theta < 40°$ result in unstable trapping at $s = 200$ and temperatures decrease with decreasing diffraction angle for both orientations in axial as well as radial direction (see Sec. 2.4.4). The angle dependency is however generally weaker for the second cooling stage than for the first cooling stage.

Summary

To summarize up to this point, trapping and cooling for the first cooling stage benefit from large diffraction angles while the overlap volume increases with decreasing diffraction angle. For the second cooling stage, a diffraction angle $\theta > 40°$ is beneficial to ensure stable trapping at low intensities. With trapping and cooling being more crucial than the size of the overlap volume, this results in a desired grating period of $800-900\,\mathrm{nm}$. This choice of grating period then also avoids second order diffraction of the 461 nm light.

5.1.2 *Wavelength Dispersion of the Diffraction Efficiency*

We now shift our attention from the angle dispersion of the grating to the diffraction efficiency dispersion. As we have seen, intensity balance is crucial for broad transitions, especially for small diffraction angles, while narrow transitions can benefit to an extent from a reduced diffraction efficiency (see Sec. 2.4. In order to achieve intensity balance, a diffraction efficiency of $1/N$ is needed where N is the number of secondary beams produced by the grating structure. Additionally, equal diffraction efficiencies of both TE and TM modes are necessary in order to conserve the incident circular polarization. Polarization impurity results in a reduced radial trapping force for both cooling stages. TE polarization corresponds to p polarization with the oscillation direction of the electric field parallel to the grating grooves and TM polarization corresponds to s polarization with the oscillation direction of the electric field perpendicular to the grating grooves. Both waves must have equal amplitudes and maintain a phase shift of $\pi/2$ to yield circular polarization. The ratio of TE and TM polarization can be adjusted by variation of the filling factor [21, 67].

To determine the quality of the diffraction properties for a given grating structure we devise a cost-function that allows its quantization in a single number. The cost function is a sum over relative deviations of all diffraction efficiencies from their target value multiplied with a weighing factor chosen according to their importance. In this cost function, we also include 0^{th} order diffraction for the first cooling stage. As 0^{th} order diffraction solely leads to an anti-trapping contribution for axial trapping and no contribution to radial trapping [21], it is desirable to suppress it. For first-stage cooling, this is mainly achieved by adjusting the grating height. As typically a grating height of $\approx \lambda/4$ is necessary to minimize 0^{th} order diffraction efficiently, it cannot easily be suppressed for second stage cooling in the same way. Instead, we cut a 3 mm hole in the wafer to prevent back-reflection to the relevant volume for second stage cooling and trapping as atoms will already be confined in a volume close to the trap axis. The cost function can take values from zero to five where zero indicates ideal diffraction properties and five corresponds to maximal deviations from the target value for all parameters.

We use rigorous wave coupling analysis (RWCA) [71] to analyze diffraction properties of gratings with aluminum or silver substrate for

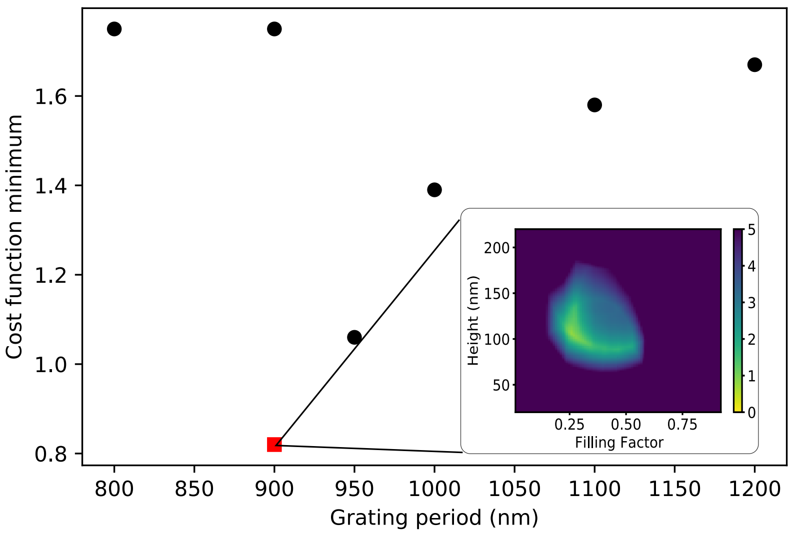

Figure 37: Cost function minimum describing how well target efficiencies are met for different grating periods. A cost function of 0 corresponds to ideal diffraction efficiencies. Cost function minima of a three-part aluminum grating are indicated with black circles as markers. The cost function minimum for a four-part grating with a thin gold layer is marked with a red square as marker. The inset shows the cost function as function of grating height and filling factor for the latter.

different grating periods, scan height, and filling factor. We found that for our wavelengths, an aluminum substrate yields better results. The minimum of the cost function of aluminum gratings for grating periods between 800 and 1200 nm is depicted in Fig. 37 (black markers) for a three-part grating with a clear minimum at 950 nm and very high cost function indicating poor diffraction properties for 800 – 900 nm – our targeted grating period.

In particular, we observe that the diffraction efficiency for 689 nm is too low. To overcome this issue, we employ a 4-part geometry lowering the target diffraction efficiency for first order diffraction to 25 %. We further use a thin gold layer to balance the diffraction efficiency of blue and red light. Gold has an absorption spectrum that peaks for short wavelengths so that the diffraction efficiency for 461 nm is lowered with a neglectable impact on 689 nm.

Careful optimization regarding the thickness of the gold layer finally yields a cost function minimum of 0.82 at a grating period of 900 nm, a clear improvement to a three part geometry at a grating period within the desired range. The inset of Fig. 37 shows the cost function value as function of grating height and filling factor for this design.

Reflectivity of a thin gold layer for the visible spectrum [91]

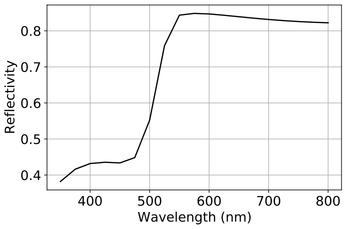

5.2 FINAL DESIGN

A 900 nm grating period corresponds to diffraction angles of $\Theta_{461} = 31°$ and $\Theta_{689} = 50°$ for 461 nm and 689 nm, respectively. The grating is further characterized by filling factor, grating height and gold layer thickness.

The cost function minimum is found for a grating height of 109 nm and a filling factor of 0.283. The latter corresponds to a groove width of 645.3 nm.

PARAMETER	GRADIENT FOR 1^{st} ORDER DIFF. EFF. 461 nm		GRADIENT FOR 1^{st} ORDER DIFF. EFF. 689 nm	
	TE	TM	TE	TM
Duty cycle	0.07%/nm	0.02%/nm	0.03%/nm	0.2%/nm
Grating height	0.3%/nm	0.1%/nm	0.6%/nm	0.2%/nm
Gold layer thickness	−0.3%/nm	−0.8%/nm	0.3%/nm	0.1%/nm

Table 3: Parameter Sensitivity of the diffraction properties for the designed grating

In order to estimate the accuracy with which the grating must be manufactured, we calculate the gradient of the first order diffraction efficiency at the design value of filling factor (duty cycle) and gradient height. An overview of these values is given in Table 3.

The grating chip has been manufactured in the clean room facilities of the Physikalisch-Technische Bundesanstalt. In a first step, a silicon wafer is coated with a 100 nm aluminum layer that serves as the base layer. The grating lines are then produced with electron-beam lithography and a lift-off process. A titanium layer is used as bonding layer. The grating structure is then subsequently coated with a thin gold layer using an evaporation process. As for the Fresnel MOT, all materials used are conductive to circumvent the collection of surface charges.

After initial manufacturing runs, a 8 nm oxide layer was identified under the gold layer through scatterometry originating due to the nature of the manufacturing process. As a consequence, the first order diffraction efficency at 461 nm and 689 nm was reduced by 3 % and 2 % respectively. To compensate this deviation from the designed geometry, we reduce the gold layer thickness from 20 nm to 10 nm in the final design used for experimental investigation in this work. This grating chip as well as a schematic representation of the unit cell are depicted in Fig. 38. Again, the gradient of the first order diffraction efficiency at the target gold layer thickness was calculated and is also listed in Table 3.

The grating geometry was evaluated with atomic force microscopy

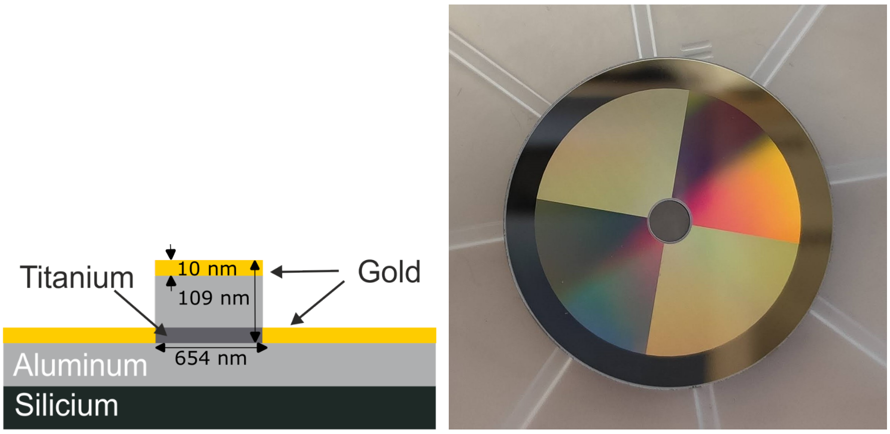

Figure 38: Left: Unit cell of the designed grating magneto-optical trap with a grating height of 109 nm, a duty cycle of 0.283 corresponding to a groove width of 654.3 nm. The gold layer has a thickness of 10 nm. Due to the nature of the manufacturing process, a 8 nm oxide layer formed under the gold layer. Right: Photograph of manufactured grating chip.

and electron microscopy in addition to scatterometry and, in general, good agreement between design and manufactured geometry was found. The diffracting properties of the grating were measured and compared to the simulated values. A good agreement between both was found as presented in Tab. 4. The ratio of TE and TM polarization mode is 1 for 461 nm and 0.89 for 689 nm. The measured intensity imbalance factor η is 1 for the first cooling stage and 0.72 for the second cooling stage. Deviations between measurement and simulations are likely a result of uncertainties in the material dispersion properties of thin-film layer as well as measurement uncertainties on the gold and oxide layer thicknesses.

	0^{th} ORDER		1^{st} ORDER	
	SIMULATED	MEASURED	SIMULATED	MEASURED
461 nm	8.4	7(1)	26.6	25(1)
689 nm	46.6	50(2)	21.4	18(1)

Table 4: Diffraction efficiencies for 0^{th} and 1^{st} order of the grating as designed and as measured. Diffraction efficiencies are averaged over TE and TM modes.

5.2.1 *Simulation of Properties for the Designed Grating*

Key characteristics of a MOT are achievable temperatures in laser cooling as well as loading rates indicated by the capture velocity. For the final design of the two-color GMOT, a theoretical study of these parameters is thus presented in the following.

Capture Velocity

The capture velocity was analyzed with the rate equation model using pyLCP [25]. It is given by the maximal intensity an atom can have and still be captured in the GMOT.
The parameters used correspond to experimental parameters used and are a laser intensity of $s = 0.5$, a magnetic field gradient of $5\,\mathrm{mT/cm}$, a beam diameter of the incident beam on the grating of $18\,\mathrm{mm}$, and a detuning $\Delta = -\Gamma$. In Fig. 39, the acceleration generated by the 1^{st} stage MOT beams is depicted in phase space for the axial and radial directions as well as the trajectories of atoms with different initial velocities in the radial and axial direction. The capture velocity for axial direction is around $50\,\mathrm{m/s}$ with a peak acceleration of $300\,\mathrm{m/s^2}$ from the incident MOT beam. In radial direction, the capture velocity is around $35\,\mathrm{m/s}$ with a peak acceleration of $70\,\mathrm{m/s^2}$. It depends strongly on the beam diameter as well. Deceleration for atoms incident along the z-axis is a lot stronger providing better loading characteristics. As mentioned previously, atoms are loaded in radial direction in this work for practical reasons.
Typical capture velocities in the six-beam MOT are $50 - 100\,\mathrm{m/s}$.

Temperature

For the first cooling transition, Eq. 31 yields a Doppler cooling limit of $T_{axial} = 0.6\,\mathrm{mK}$ and $T_{rad} = 2.7\,\mathrm{mK}$ for axial and radial direction, respectively.
For the second cooling stage, we again deploy our pyLCP rate equation model to look at the light-atom dynamics and determine the Doppler cooling limit for different intensities this way (see Fig. 40).
The temperature in radial direction is approximately twice as large as the temperature in axial direction for high intensities. In radial direction, a minimum is reached at an intensity of $s = 10 - 20$. The temperature then increases from around $1.5\,\mu\mathrm{K}$ to just under $2\,\mu\mathrm{K}$. The minimal temperature in axial direction is reached for $s = 10$ corresponding to the Doppler temperature $T_D = \frac{\hbar\Gamma}{2k_B}$. The curve then flattens out and stays at this temperature for lower intensities.
The increase in radial temperature is not readily understood but also observed experimentally as we will see in the following section.

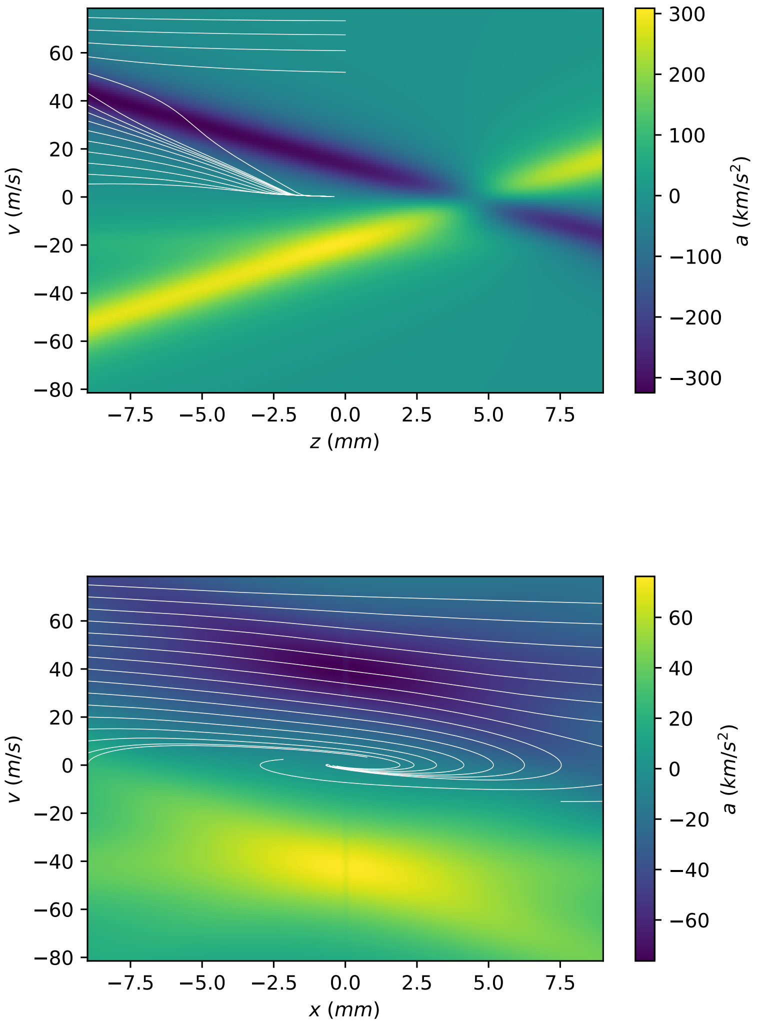

Figure 39: Capture trajectories of atoms with the first cooling stage MOT beams of the designed GMOT. Top: Acceleration given by the MOT beams and capture trajectories for the axial direction. Bottom: Acceleration given by the MOT beams and capture trajectories for the radial direction.

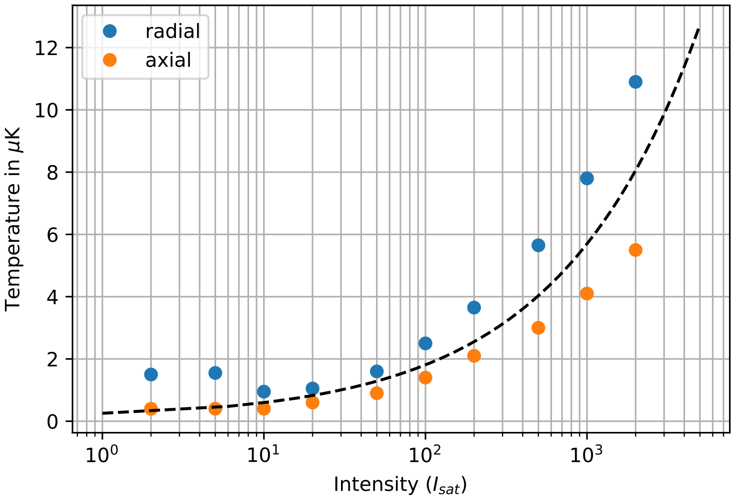

Figure 40: Simulated axial (orange) and radial (blue) temperatures in the 2^{nd} cooling stage MOT for different intensities of the incident MOT beam for the designed grating with $\theta_{689} = 51°$. The black dashed line indicates the doppler cooling limit for the standard six-beam MOT for reference.

5.3 EXPERIMENTAL CHARACTERIZATION

As the axial shift of the overlap volumes complicates the transfer between the cooling stages, a vital achievement lies in the experimental sequence achieving and optimizing this transfer. As such, we will first discuss the experimental sequence used for the generation of ultracold ^{88}Sr atoms with a two-color GMOT. We will then look at the experimental results of 1^{st} and 2^{nd} cooling stage in detail. The grating MOT was mounted in the vacuum chamber so that the magnetic field zero of the quadropole field lies in the overlap region of both trapping volumes. Specifically, the 18 mm flat-top laser beam results in an overlap volume with its center, i.e. the height with maximal radial expansion of the overlap volume, 7.5 mm above the laser chip. The chip is mounted in a way such that this corresponds to 1.5 mm above the geometric center of the in-vacuum magnetic field coils. This is compensated by applying an offset field in axial direction using an additional pair of coils.

0^{th} order reflection allowed an easy alignment of the angle of the incident beam and (contrary to the Fresnel MOT) no radial support beams were needed for initial alignment.

5.3.1 *Experimental Sequence*

The experimental sequence optimizing transfer efficiency from the 1^{st} to the 2^{nd} cooling stage is depicted in Fig. 41. Initially, approximately 10^6 atoms are loaded into the 1^{st} stage MOT using a quadropole field with a magnetic field gradient of 5 mT/cm. During the loading sequence, the deceleration beam is on (not depicted). When the deceleration beam is switched off during the loading phase, the loading rate is reduced by a factor >100.

After a loading time of 300 ms, the deceleration beam used to initially slow the atoms from the oven beam is switched off, slightly modifying the position of the atom cloud as its radiation pressure is removed. To load into the BB MOT, the 689 nm laser used for second-stage cooling is then turned on at maximum power and its frequency is modulated at 50 kHz broadening the laser linewidth to 1.6 MHz. The magnetic offset is then ramped down moving the magnetic field minimum towards the grating chip and thus towards the overlap volume of the second cooling stage. Simultaneously, the intensity of the first stage cooling laser is also ramped down to zero. This combination of ramping the magnetic field offset and the laser intensity of the first stage cooling laser with the second-stage cooling laser already on at full power proved to be vital to maximize transfer efficiency between the MOT stages. After this transition, the magnetic field gradient is reduced to 0.3 mT/cm. Following further cooling in this broadband phase for 20 ms, the magnetic field gradient is then steadily increased

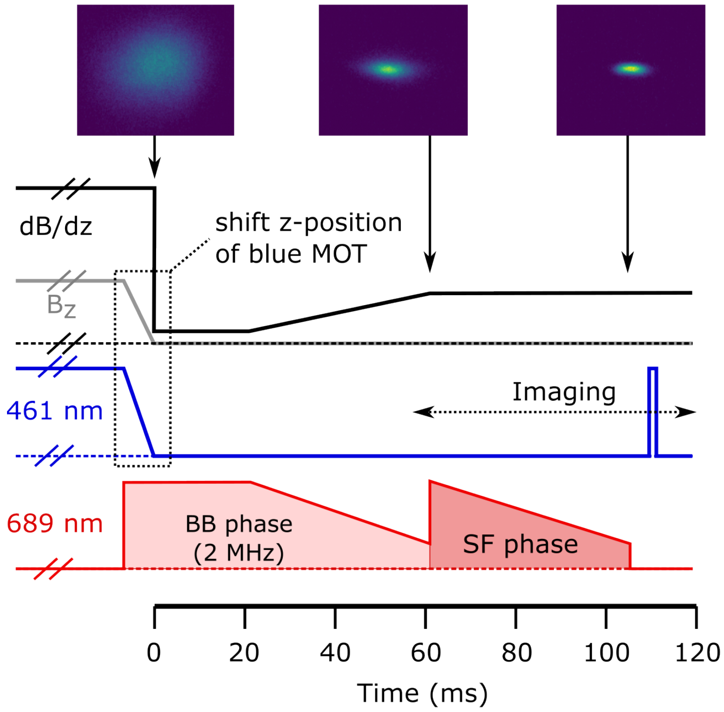

Figure 41: Timing diagram showing the experimental sequence. Black: Magnetic field gradient of the applied quadropole field, Grey: Strength of the axial offset field, Blue: Intensity of the first stage cooling laser, Red: Intensity of the second-stage cooling laser. Fluorescence images of the atom cloud after initial loading and cooling on the first cooling stage, after the broadband phase of the second cooling stage, and after the subsequent single-frequency phase are shown at the top. This figure has been previously published in Ref. [12].

over a period of 40 ms to a value of 1 mT/cm, and the laser intensity steadily decreased, further cooling and compressing the atom cloud. The laser modulation is then turned off and the power in the 689 nm beam increased to maximum, initiating the single frequency phase. As the Doppler limit for the temperature scales with the saturation broadened linewidth, the intensity is then again steadily decreased over a period of several tens of ms, continuously cooling the atoms to lower temperatures.

5.3.2 1^{st} *Stage Cooling of* ^{88}Sr

Lifetime

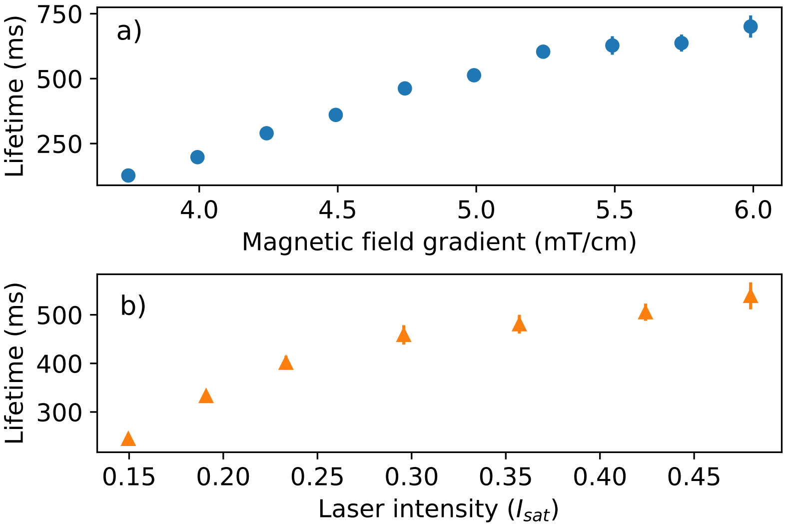

Figure 42: Life time in the first-stage MOT as function of a) magnetic field gradient at a laser intensity of the incident beam of $I = 0.48\, I_{sat}$ and b) as a function of laser intensity of the incident MOT beam with a magnetic field gradient of $dB/dz = 5\,\text{mT/cm}$. Error bars are approximately the size of the data points. This figure was previously published in Ref. [12].

Unlike in the Fresnel MOT, a neglectable amount of atoms is trapped when the deceleration beam is turned off. We thus perform lifetime measurements by loading the MOT, subsequently switching off the deceleration beam, and observing the atom number decay in the MOT by variation of the wait time before detection. Lifetimes of up to 700 ms are measured. During these measurements, vacuum pressure is measured to be $3 \cdot 10^{-9}$ mbar. This upper limit is in agreement with a vacuum-limited lifetime [73]. However, we observe that the lifetime depends on the laser intensity and magnetic field gradient and lower lifetimes are achieved when the magnetic field gradient and/or laser intensity is decreased (see Fig. 42). These observations are in agreement with the results published by Sitaram et al. [100]. This behavior is linked to the reduced trap depth and reduced trapping coefficient in the given GMOT configuration with $\theta_{461} = 31°$. The axial trapping coefficient κ_z is reduced to $\approx 10\,\%$ of the trapping coefficient in a six-beam configuration with the same beam intensity and magnetic field gradient as seen in Fig. 35 a). From Eq. 24, we expect an increase in trap depth with magnetic field gradient as long as the laser detuning remains larger than the Zeeman shift within the trapping volume [118]. The trapping coefficient increases further with $s/(1+s)$ for laser intensity. As a result, both a high magnetic field gradient or high laser intensity strengthens confinement and closes the loss channel. The fact that loading effectively stops with the deceleration beam turned off can also be traced back to the strongly reduced trapping coefficient and trap depth as well as a reduced capture velocity in comparison to the Fresnel MOT. The latter results from the larger angle with the radial axis in the GMOT yielding a reduced cooling effect on the atoms in the thermal atom beam originating from the oven.

Atom number

The atom number reached in the 1^{st} stage MOT depends on a number of experimental parameters including magnetic field gradient, the intensity of the incident MOT beam, the intensity of the deceleration beam as well as the oven temperature. The relation between atom number and these experimental parameters has been measured. Results are presented in Fig. 43. We observe a strong increase of the atom number with oven temperature (see Fig. 43 a)) explained by an improved loading rate as the evaporation rate of strontium in the thermal atom source increases exponentially. We also observe an increase in atom number with increasing intensity in the deceleration beam that eventually saturates around $I = 0.2 I_{sat}$ (see Fig. 43 b)). This is explained by a higher scattering rate and more efficient slowing of the atom. The increase in atom number with increasing intensity in the MOT beams (see Fig. 43 c)) and increasing magnetic field gradient (see Fig. 43 d)) and is due to the increase in lifetime discussed in the previous section. At typical operation parameters, 10^6 atoms are trapped in the first-cooling stage.

Temperature

Temperature measurements are again performed with TOF measurements as for the Fresnel MOT. Again, the laser intensity is kept constant after loading long enough for the atom cloud to thermalize. For a diffraction angle of 31°, we obtain a theoretical ratio of $\frac{T_{rad}}{T_{ax}} \overset{!}{=} 4.08$ of radial to axial temperature. Experimentally, we again observe a strong dependency of the temperature on the laser intensity although

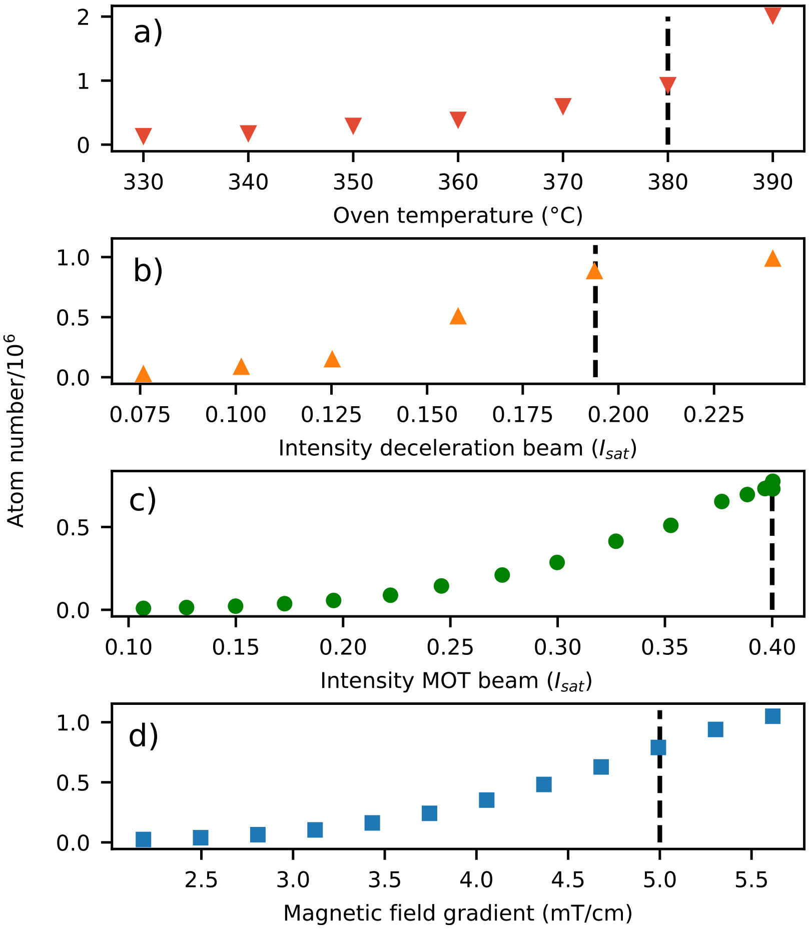

Figure 43: Atom number as a function of a) oven temperature, b) intensity of the deceleration beam, c) intensity of the incident MOT beam and d) magnetic field gradient. Where the individual parameter is not varied, the laser intensity of the incident MOT beam is $I = 0.4\,I_{sat}$, the magnetic field graient is $dB/dz = 5\,mT/cm$, the oven temperature is $T = 380°C$ and the intensity of the deceleration beam is $I = 0.2\,I_{sat}$. Typical parameters are indicated with vertical dashed lines.

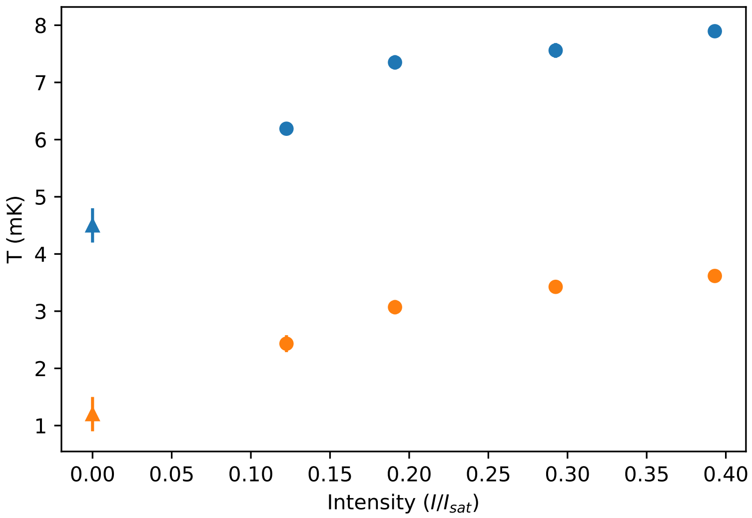

Figure 44: Temperature in radial and axial direction in the first stage MOT as a function of laser intensity of the incident MOT beam. Laser intensity is kept constant after loading for an extended period of time to allow the atoms to thermalize (circulsr marker) or the intensity is linearly ramped to 0 (triangular marker).

the intensity stays below $s = 0.5$ as depicted in Fig. 44. This behavior is similar to the observations for the Fresnel MOT where we have discussed the underlying cause of intensity fluctuations in detail. The temperature increase is however less severe, indicating that intensity fluctuations play a lesser role in the GMOT.
Minimal temperatures are reached when the intensity of the blue MOT beams is linearly ramped to 0. Here, we achieve an axial temperature of (1.2 ± 0.3) mK and a radial temperature of (4.5 ± 0.3) mK corresponding to the expected ratio of 4.08 within one standard deviation. The temperatures exceed the theoretical Doppler limit factor of 2.

5.3.3 2^{nd} *Stage Cooling of* ^{88}Sr

With the experimental sequence described above, we typically reach a transfer efficiency of 25% from the first cooling stage to the SF phase of the second cooling stage resulting in a sample of 2.5×10^5 atoms being cooled to µK temperatures. A phenomenon typical for SF narrow-line MOTs of bosonic strontium is the formation of so-called shells. As the atom cloud forms where the gravitational acceleration is balanced by the acceleration resulting from scattering from the MOT beams and their resonance position depends on detuning (see Sec. 2.4), so does the position of the atom cloud. A fluorescence image of the atom cloud for different detunings was recorded and is depicted

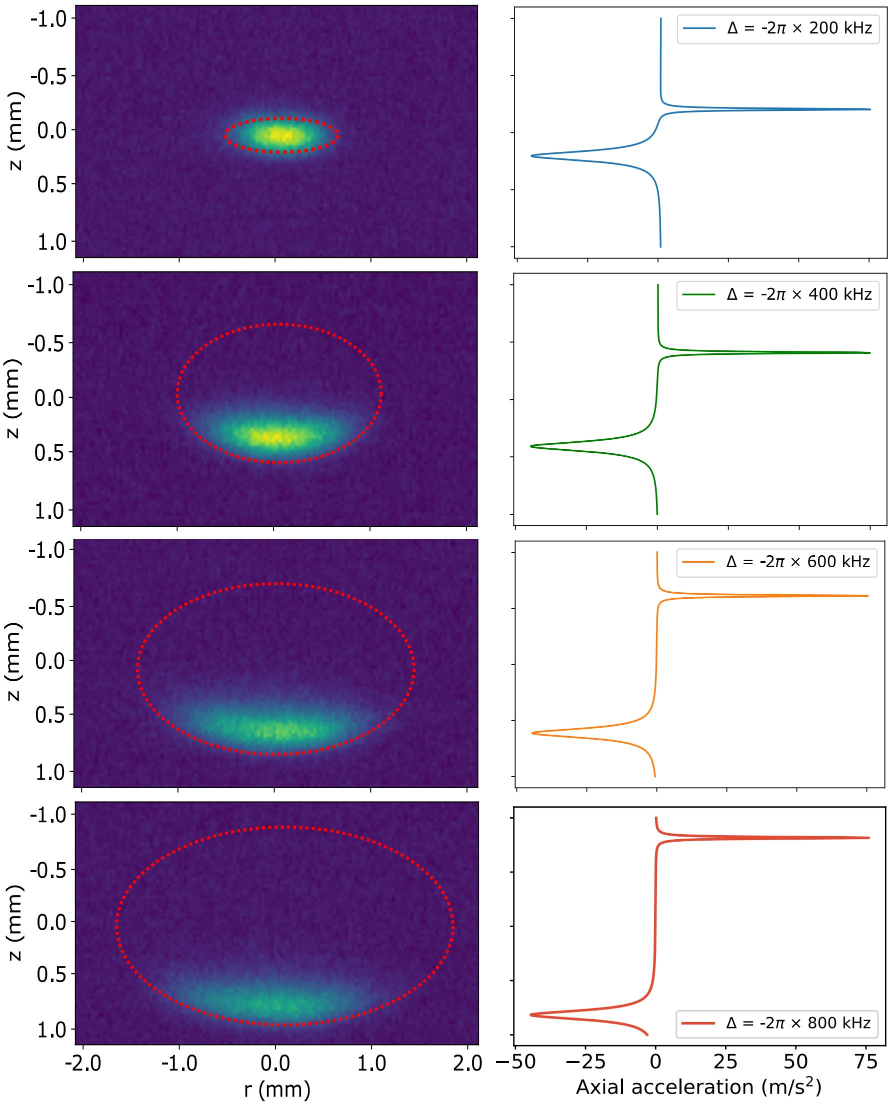

Figure 45: Detuning dynamics in the GMOT. Fluorescence images are shown on the left wth corresponding acceleration profiles on the right for detunings of 200 kHz, 400 kHz, 600 kHz and 800 kHz. For large detunings, the atoms accumulate at the lower boundary of the ellipsoid indicating resonance. The brightness decreases with increasing detuning due to a decreasing (number) density.

in Fig. 45. Alongside the fluorescence images for different detunings the simulated axial acceleration on an atom at rest with the corresponding detuning and parameters as in the experiment is shown. The dashed ellipsoids indicate the resonance boundary. The detuning at which the SF MOT is typically operated is chosen as approximately $-220\,\mathrm{kHz}$. This leads to a compressed atom cloud whose width is well described by a Gaussian functions in axial and radial direction. For smaller detunings, a decrease in atom number was observed.

Further, a cold atom cloud with temperature in the μK range is recorded expanding for 10 ms illustrating the TOF method (see Fig. 46) The low velocity and expansion rate of the atom cloud allows observation of the free fall of the atom cloud. The calibration of the imaging system was tested by fitting a parabola with $z(t) = a + 0.5 \cdot b \cdot t^2$ to the position over time of the falling atoms. The fit parameter b was found to agree with the gravitational acceleration $g = 9.81\,\mathrm{m/s^2}$ within its uncertainty.

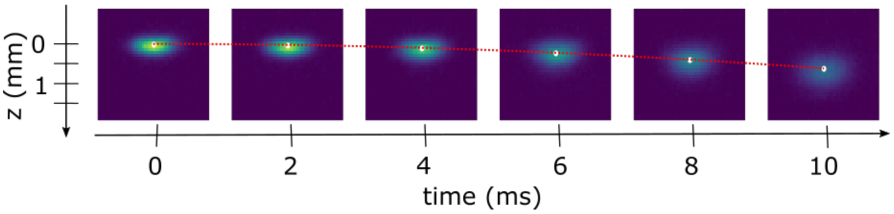

Figure 46: Time-of-flight measurement of the expanding cold atom cloud in free fall. The white points mark the center of the atom cloud, the red dashed line indicates the free fall parabola with $z = 0.5 \cdot g \cdot t^2$ with $g = 9.81\,\mathrm{m/s^2}$

With the TOF method, temperatures in the BB MOT and the SF MOT were again analyzed in detail. The temperatures in the BB phase and the SF phase for different intensities are depicted in Fig. 47. In the BB MOT atoms are cooled down to a temperature of around 10 μK. This result is comparable to results reached in the conventional six-beam configuration [84]. The atoms continue to be cooled in the SF MOT, reaching minimal temperatures $< 5\,\mu\mathrm{K}$ in both axial and radial direction. Axial and radial temperature initially decreases with intensity as expected with the minimal temperature being reached at around $20\,I_{sat} - 30\,I_{sat}$. In this section, the experimental data qualitatively agrees with the theoretical values obtained from the pyLCP simulation. For intensities lower than $s = 20$, we observe an increase in temperature in both axial and radial temperature. The increase is particularly pronounced for the radial direction. While we observe a slight increase in the simulated date for the radial direction as well and in the axial direction temperature flattens, the strong increase in the experimental data is a deviation from the simulated data. The rea-

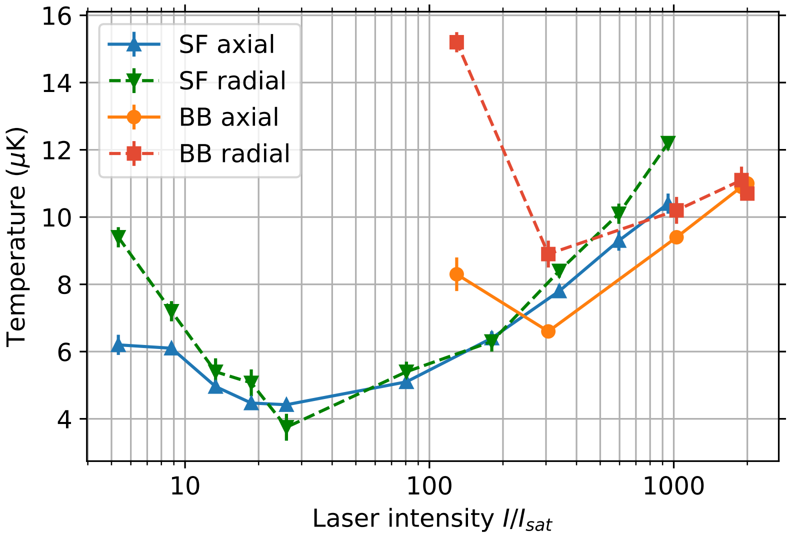

Figure 47: Temperature in axial and radial direction as function of laser intensity in the BB MOT and the SF MOT. This figure was previously published in Ref. [12]

son behind this could not be identified through analysis of the atom dynamics in simulations. Possibly, this effect is linked to the home-built laser, which was not fully characterized and has a linewidth broader than the transition linewidth. Furthermore, we have seen in the simulations that for intensities smaller than $s = 20$ the confinement becomes so weak that atoms start to be lost from the trap which potentially leads to measurement artifacts.

With a temperature of $< 5\,\mu\mathrm{K}$, the atoms are cold enough to be loaded into an optical lattice with a typical trap depth of $10\,\mu\mathrm{K}$. We have further seen that mounting the grating such that the secondary beams counteract gravity and thus eliminating the anti-trapping force for the SF MOT and additional scattering, should allow cooling to even lower temperatures (see Section 2.4.4). A GMOT in this configuration was realized by the Maryland group where temperatures of $4.5(6)\,\mu\mathrm{K}$ and $2.9(1)\,\mu\mathrm{K}$ for radial and axial direction respectively were measured [26].

FERMIONIC STRONTIUM

Attempts to capture fermionic strontium in the GMOT where unsuccessful. One possible explanation lies in the fact that the position where the ^{87}Sr MOT forms is further away from the grating as also observed for the Fresnel MOT where the difference in position depends on the exact geometry [27]. In combination with a high background and small trapping coefficient, alignment as well as detection of small signals becomes challenging.

6

MAGNETO–OPTICAL TRAPPING IN MICRO–GRAVITY

As we have seen previously, the forces on the narrow-line transition are on the same order of magnitude as gravitational acceleration resulting in the formation of so-called shells for bosonic strontium depending on the detuning and magnetic field gradient chosen. We have emphasized the different trapping characteristics of the incident beam aligned and anti-aligned with gravity. As the Fresnel MOT and the two-color gMOT was designed with the use in transportable and also space-born applications in mind, we now revisit this topic and shift our attention to key aspects of a narrow-line MOT operation in micro-gravity.

In the absence of a constant acceleration, atoms can move freely within the ellipsoid limited by the resonance boundary where the detuning of the laser beams corresponds to the sum of Zeeman shift and Doppler shift. Atoms will thus spend a significant amount of time near the center of the ellipsoid and fill the ellipsoid entirely instead of forming shells. For MOT operation in Regime II with $s >> 1$ and $|\Delta| < \Gamma_E$ coupling to the π transition results in a constant acceleration. For parameters corresponding to Regime I with $s >> 1$ and $|\Delta| >> \Gamma_E$, a neglectable amount of photons are scattered between the resonance peaks. In both cases, no cooling takes place. With this change in trap dynamic for the narrow-line MOT, the important question arises what the consequences are for number density and temperature – both important quantities for further cooling to a Bose–Einstein condensate or transfer to an optical lattice.

For fermionic strontium, each $m_F \rightarrow m_F'$ transition has a different resonance frequency resulting in a number of shells that all overlap with one another so that ultimately, the whole ellipsoid is filled even in the presence of gravitational acceleration and light-atom interaction takes place for all atom positions within the trap [101]. Here, the transition to micro-gravity thus likely has a smaller impact on the SF MOT dynamics.

6.1 TEMPERATURE AND NUMBER DENSITY

Temperature and number density in the SF MOT both scale with detuning. For the SF MOT in micro-gravity, we find that temperature increases faster with increasing detuning than in the presence of gravitational acceleration. For MOT operation in regime I, the number density decreases significantly faster than with gravitational acceleration present. Consequently, it is desirable to operate the SF MOT at low detuning. Transfer from the BB MOT is than facilitated by a compression phase where the magnetic field gradient is already ramped up during the BB MOT phase as also realized in the experimental sequence used in this thesis.

Here, we operated the SF GMOT at a detuning of $\Delta \approx -220\,\mathrm{kHz}$ and a magnetic field gradient of $\mathrm{d}B/\mathrm{d}z = 0.5\,\mathrm{mT/cm}$. For smaller detunings, the atom number rapidly decreased. This is readily understood as the detuning than corresponds to the saturation broadened linewidth Γ_E at $s = 1000$ and strong coupling to the π transition drastically reduces the trap depth. Further reducing the detuning also leads to the resonance peaks starting to overlap. Eventually, the zero-crossing vanishes.

In order to compare MOT dynamics in micro-gravity with MOT dynamics in the presence of gravitational acceleration for both gravity parallel (chip down) and anti-parallel (chip up) to the incident beam and develop a first intuition, we return to our pyLCP rate equation model and choose parameters as in our GMOT experiment. As the GMOT offers the highest level of miniaturization, it would be an ideal candidate for space-borne quantum sensing missions.

Figure 48 shows position, velocity and temperature for the different configurations in axial direction. In the first row the position as a function of time for all three configurations is depicted. The second row shows a histogram of the position. The third row shows the z-component of the velocity as a function of time while the fourth row shows the evolving axial temperature. Initial velocity and position are randomly distributed within the capture range. As expected, while atoms occupy a small region inside the ellipsoid given by the resonance boundary, the volume is fully occupied in the micro-gravity case with the majority of the atoms near the magnetic field minimum. The distribution is slightly asymmetric, which is explained by the asymmetry of the trapping potential we have observed earlier (see Section 2.4). The temperature in axial direction is slightly higher than in the presence of gravitational acceleration. This difference was found to be increasing with increasing detuning as also observed by Ren et al. [89].

Figure 49 shows position, velocity, and temperature for the different configurations in radial direction. For radial direction, all configurations show a distribution in position around the magnetic field minimum. In the case of micro-gravity, the width of the distribution is increased yielding again a decreased number density. Again, we observe slightly higher temperatures for the micro-gravity case as well. As quantum sensors like optical lattice clocks require transfer of the atoms from the SF MOT to an optical lattice, let us now look at how transfer efficiency is impacted by the change in trap dynamics.

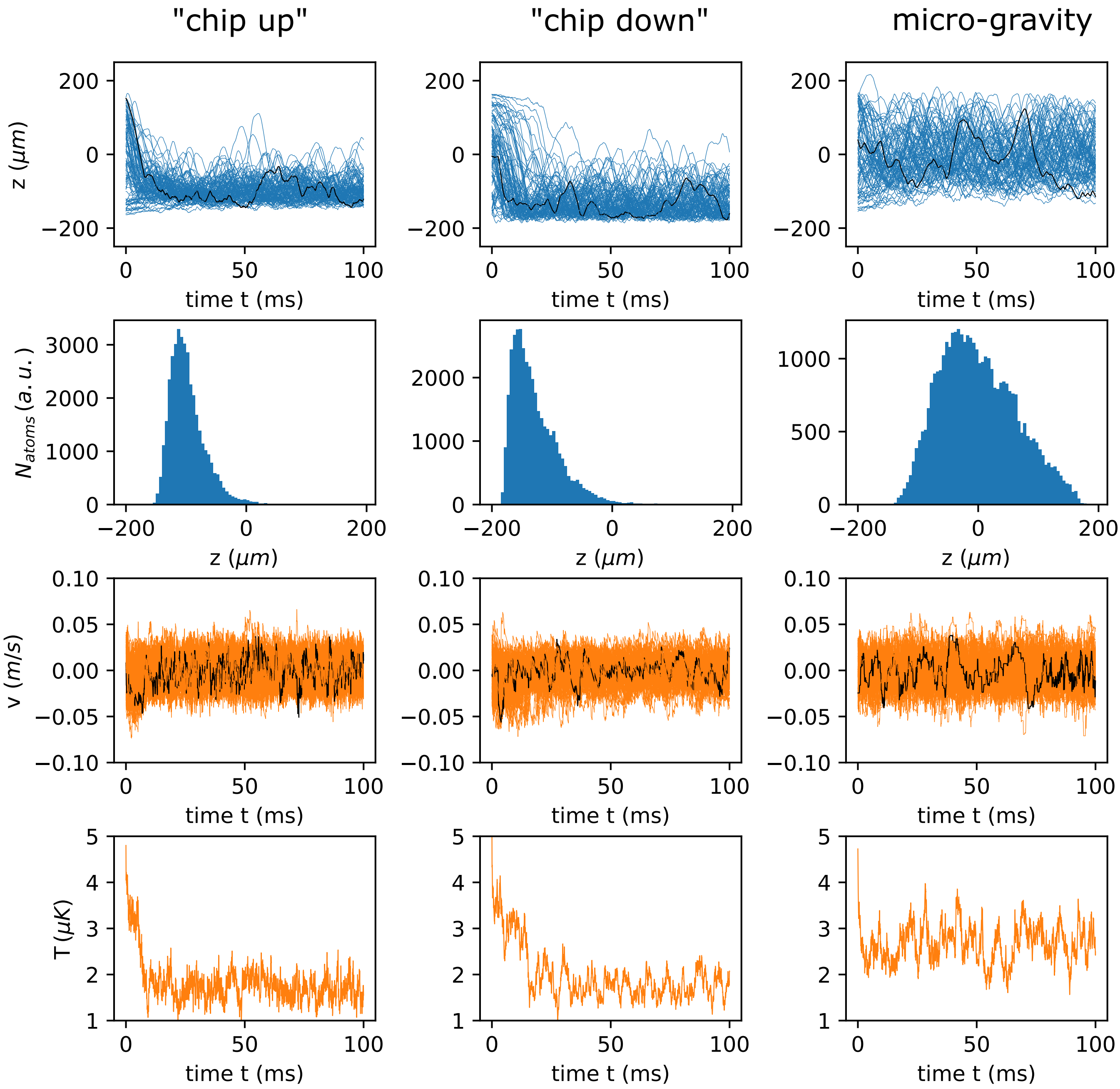

Figure 48: Atom dynamics in axial direction in all gravity cases. The first column corresponds to gravitational accleration anti-prallel to the wavevector of the incident beam (chip up), the second column to gravitational accleration prallel to the wavevector of the incident beam (chip down) and the third column corresponds to the case of a gMOT in microgravity. The first row shows the z-position of a sample of atoms as a function of time. The initial position is randomly distributed within the MOT volume. The trajectory of a single atom is illustrated in black and serves as examplary trajectory. The second row shows the position of the atoms of the last 50 ms as histogram. The third row shows the z-component of velocity of the atoms as function of time where the initial velocity is again randomly chosen within the capture range. Lastly, the fourth row shows the average axial temperature of the atom ensemble as a function of time spent in the SF MOT. Parameters are given in the text.

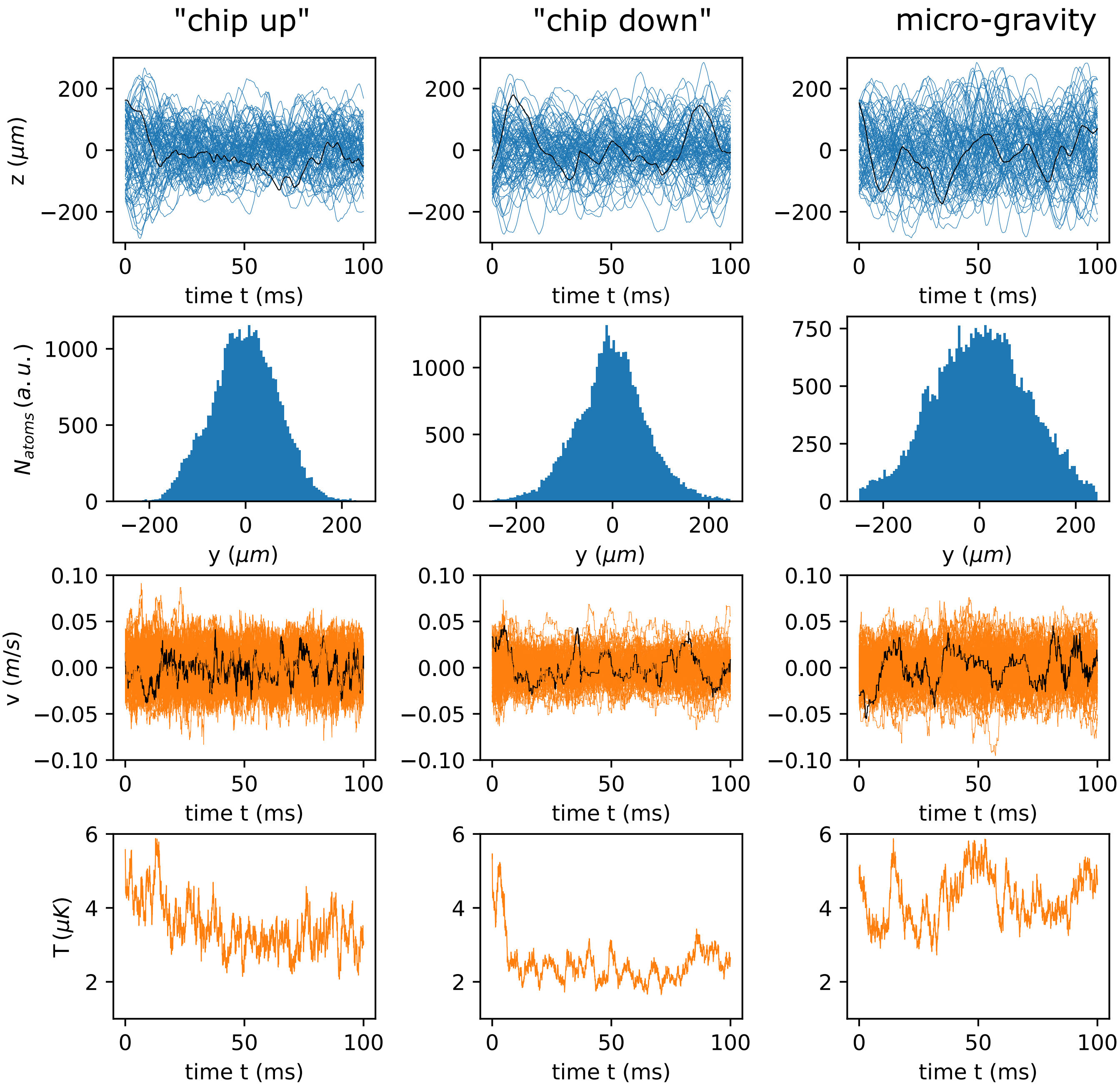

Figure 49: Atom dynamics in radial direction in all gravity cases. The first column corresponds to gravitational accleration anti-prallel to the wavevector of the incident beam (chip up), the second column to gravitational accleration prallel to the wavevector of the incident beam (chip down) and the third column corresponds to the case of a gMOT in microgravity. The first row shows the y-position of a sample of atoms as a function of time. The initial position is randomly distributed within the MOT volume. The trajectory of a single atom is illustrated in black and serves as examplary trajectory. The second row shows the position of the atoms of the last 50 ms as histogram. The third row shows the y-component of velocity of the atoms as function of time where the initial velocity is again randomly chosen within the capture range. Lastly, the fourth row shows the average radial temperature of the atom ensemble as a function of time spent in the SF MOT. Parameters are given in the text.

6.1.1 *Transfer Efficiency to an Optical Lattice*

We look at a simple model to investigate transfer efficiency to an optical lattice with lattice depth U_0 where the optical lattice is given by a cylindrical volume with radius $\omega_0 = 65\,\mu\text{m}$. The magic wavelength for strontium is 813 nm resulting in a Rayleigh range of 2 cm so that the atom cloud is much smaller than the Rayleigh range. A cylinder is thus a reasonable approximation. With a given lattice depth U_0, we will consider an atom as captured, if it is within the lattice volume with a velocity $v < v_{cap}$ where v_{cap} denotes the capture velocity given as

$$v_{cap} = \sqrt{\frac{2 \cdot U_0}{M}} \tag{36}$$

This is of course an oversimplification and results should be interpreted more qualitatively than quantitatively. The purpose of this approach is to develop a first intuition.

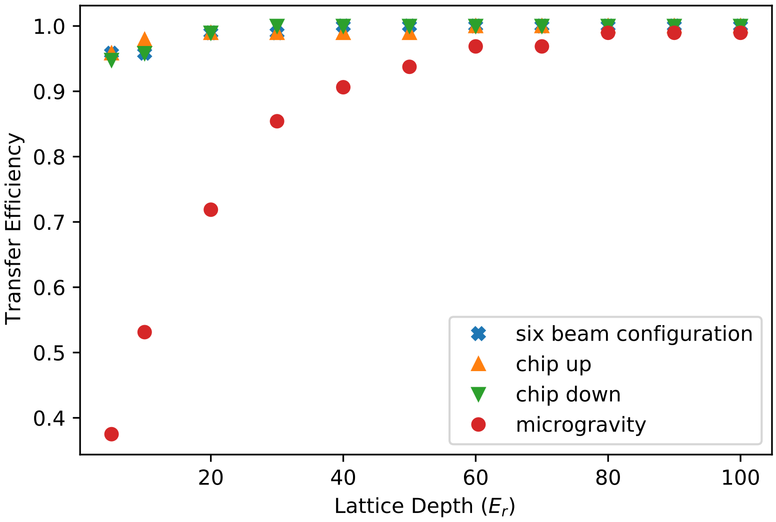

Figure 50: Simulated transfer efficiency to an optical lattice from the SF MOT with $\Delta = -200\,\text{kHz}$, $s = 200$ and $dB/dz = 0.5\,\text{mT/cm}$ for the grating MOT with gravity and in microgravity. For comparison, results for a six-beam configuration with gravity are also shown. "Chip up" corresponds to a geometry as used in this work with the incident beam counteracting gravity and "chip down" corresponds to a geometry where the diffracted beams counteract gravity. Due to the simplicity of the model, the figure should be understood as a qualitative comparison.

The transfer efficiency as a function of lattice depth for both grating orientations with gravity as well as the micro-gravity case is given in Fig. 50. For comparison, transfer efficiency as simulated for the six-beam geometry in the presence of gravitational acceleration is also shown. We observe that comparable transfer is reached in this model for lattice depth of $U_0 > 60\,E_r$.

Typically, the optical lattice where spectroscopy of the clock transition takes place is operated at low intensities in order to suppress the lattice light shift that increases with increasing lattice depth [52]. However, at trap depth of around $100\,E_r$ the lattice light shift can still be determined at a mid 10^{-19} uncertainty thus currently not limiting clock performance [46]. Furthermore, a deep lattice results in increased power demands on the laser system.

To improve number density and temperature and thus transfer efficiency, one can continuously decrease detuning while simultaneously decreasing intensity yielding a higher number density and lower temperature. The limit here is likely given by the anti-trapping force producing a loss channel whose effect becomes stronger for low intensities as well as acceleration resulting from coupling to the π transition accelerating atoms and allowing them to escape.

While this might allow to relax the requirements on lattice depth during initial loading into the lattice, the question arises if a deep lattice is needed during interrogation for space-borne optical clocks either way as the tunnel shift is no longer suppressed by gravitational acceleration. We will explore this in the next section.

6.1.2 *Tunneling*

The approximation that atoms are localized to their lattice site only holds for deep lattices. For shallow lattices, the wave function of the atom extends to the neighboring lattice sites and tunneling takes place [52]. To gain an understanding of the resulting dynamics and effects on transition fequency, let us take a closer look at the energy eigenstates of a shallow lattice. The external Hamiltonian in the presence of an optical lattice becomes

$$H_{ext} = \frac{\hbar^2 k^2}{2M} + \frac{U_0}{2}\left(1 - \cos(2k_l x)\right) \tag{37}$$

where $\vec{k_l}$ is the wave vector of the optical lattice. The eigenstates $|n, q\rangle$ are given by the two quantum numbers n and q where n denotes the energy band and q the quasi-momentum along the x-axis. Solutions will be periodic in q as stated by Bloch's theorem so that we can limit ourselves to the first Brillouin zone $q \in [-k_l, k_l]$. With plane wave representation we then obtain:

A detailed derivation can be found in [52] or, for the French-speaking readers, in [48]

$$H_{ext}|k\rangle = \left(\frac{\hbar^2 k^2}{2M} + \frac{U_0}{2}\right)|k\rangle - \frac{U_0}{4}\left(|k + 2k_l\rangle + |k - 2k_l\rangle\right) \tag{38}$$

Solving this problem numerically [36] and finding the eigenvectors and eigenstates then allows to calculate the energy bands for different lattice depth [48, 52]. Figures 51 a) and b) compares the energy bands for two different lattice depths $U_0 = 10$ and $U_0 = 100$. For a shallow lattice, the energy bands have an increasing bandwidth with increasing quantum number n. For a deep lattice, the energy bands can be approximated as straight with a negligible bandwidth and closely resemble the eigenenergies of the harmonic oscillator [48]. The

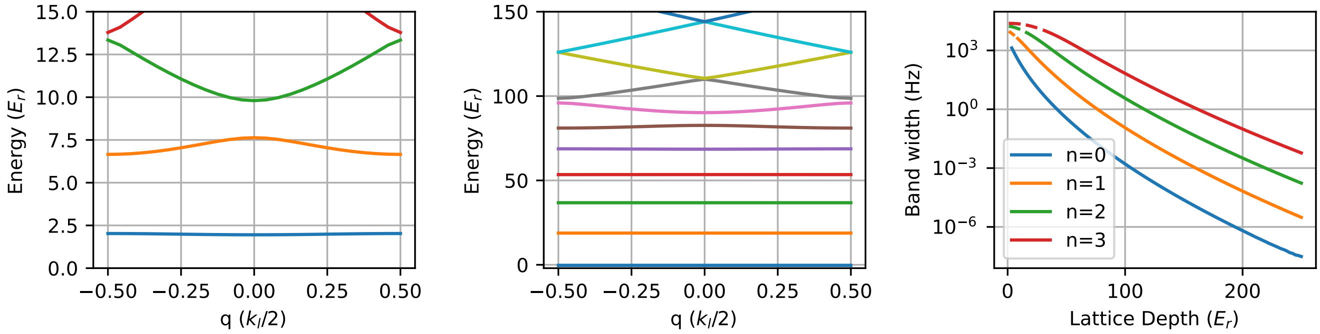

Figure 51: a) Energy bands of an optical lattice with $U_0 = 10\,E_r$ b) Energy bands of an optical lattice with $U_0 = 100\,E_r$ c) Band width of the first four energy bands as a function of lattice depth U_0. For lattice depth shallower than the energy band, the bandwidth is depicted as dashed line.

bandwidth of the energy bands populated by the atoms determines the severity of the effect on the clock transition line and can result in both a frequency shift as well as line broadening. Figure 51 c) shows the energy bandwidth as a function of lattice depth for the first four energy bands. Let us consider two cases to deepen our insight into the dynamics at hand. In the case of a pure state $|n, q\rangle$, the carrier frequency will be shifted from the atom frequency by $\hbar(\omega_{n.q} - \omega_{n.q+k_s})$ as atom will transition from the pure state $|n, q\rangle$ in the ground state to the state $|n, q+k_s\rangle$ in the excited state. Here, $\vec{k_s}$ is the wave-vector of the clock laser [48, 52]. In contrast, if atoms are populating the $n = 0$ band uniformly, they will also uniformly populate the energy band in the excited state. Thus, the different frequency shifts of the single atoms will average out and the carrier frequency is no longer shifted from resonance. Instead, this results in inhomogeneous line broadening [48, 52].

While tunneling is easily suppressed in the presence of gravitational acceleration as it lifts the degeneracy of the energy levels in the lattice sites and effectively suppresses tunneling entirely, tunneling is an on-resonance process in micro-gravity and not trivially suppressed.

Figure 52 shows a worst case estimate of the frequency shift from tunneling as a function of lattice depth and temperature of the atoms. In this simple model, we assume a pure state. Temperature yields the population distribution of the different energy bands and for each individual band the bandwidth is taken as frequency shift. Radial motion and its consequences are neglected.

In order to limit this shift to the mHz range corresponding to a relative frequency inaccuracy in the $10^{-18} - 10^{-18}$ range, lattice depths of $> 100E_r$ are necessary.

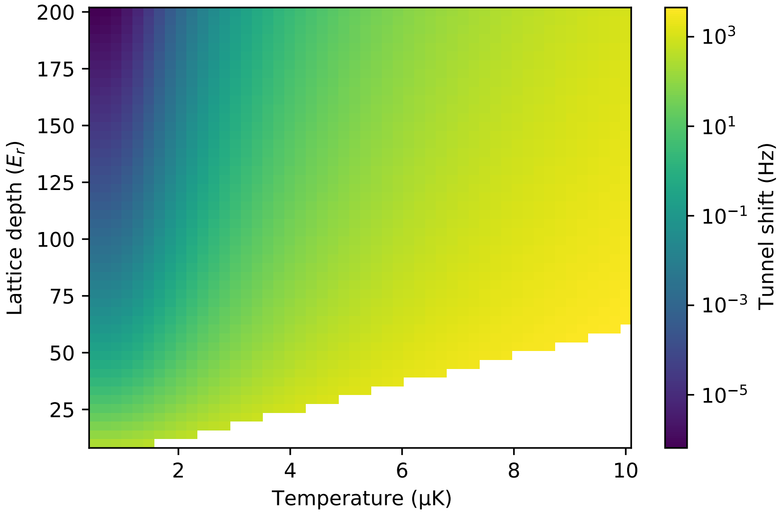

Figure 52: Tunnel shift as a function of optical latice depth and atom temperature.

An argument can thus be made that a probable reduced transfer efficiency for shallow lattices does not come into play if a high intensity lattice needs to be used to suppress the tunnel shift in the first place. However, due to the aforementioned lattice shift scaling with trap depth, it might be desirable to find an alternative method to suppress the tunnel shift. Indeed, some suggestions have been made utilizing a dynamic control of the lattice [114] or a geometry utilizing a 2D lattice where the Gaussian beam profile from the opposite lattice direction yields an energy offset [51].

To summarize, the atom dynamics in the SF MOT and an optical lattice in micro-gravity differ significantly from atom dynamics in the presence of gravitational acceleration. In micro-gravity, one has to handle higher temperatures and a reduced number density and experimental parameters optimized for experiments in the presence of gravitational acceleration will need to be re-optimized for micro-gravity. While a deeper lattice might be necessary to load atoms from the SF narrow-line MOT, a deeper lattice is also required to suppress the tunnel shift so that the change in MOT dynamics alone does not increase power consumption of space-borne quantum sensors.

7

SUMMARY AND OUTLOOK

7.1 SUMMARY

This work investigates the design and describes the successful operation of two planar structures for two-color magneto-optical trapping. The Fresnel MOT presents an achromatic design that is thus usable for all atom species where a suitable reflectivity at the cooling transition wavelengths can be obtained. The aluminum coating used here has a reflectivity of $\approx 90\%$ in a range from 150 nm to 800 nm covering i.e. all commonly used cooling transitions for strontium, ytterbium and rubidium. As such magneto-optical trapping of multiple atom species is also enabled. The advantage of achromaticity is combined with ample optical access known from the GMOT.
Here, two-color cooling of ^{88}Sr on the $^1P_1 \rightarrow {}^1S_0$ transition and in a BB MOT on the $^3P_1 \rightarrow {}^1S_0$ transition to a temperature of $(25 \pm 3)\mu K$ in the axial and $(43 \pm 4)\mu K$ in radial direction was demonstrated. Further cooling is possible by adding a SF phase on the narrow-line cooling transition. Loading directly from the hot atom beam produced by the thermal atom source was demonstrated, illustrating a good capture velocity.
A parameter-dependent lifetime was observed in the first stage MOT with the lifetime increasing with decreasing intensity and increasing magnetic field gradient. This was linked to a strong increase in temperature with increasing intensity reducing the efficiency of the repumping scheme attributed to an extra heating mechanism originating from intensity fluctuations [19]. For the Fresnel-MOT geometry, intensity fluctuations can result from a slight misalignment of the incident beam, an inhomogeneous intensity profile as well as manufacturing imperfections.
Furthermore, trapping and cooling of fermionic strontium in the first stage MOT was demonstrated where the MOT formed further away from the trap surface. The atom number ratio between fermionic and bosonic strontium was much smaller than expected from the isotope abundance. As possible reasons, the complex trap dynamics as well as technical difficulties were identified. A transfer to the second cooling stage was not attempted due to the poor signal to background ratio.
Furthermore, the design and operation of a two-color GMOT for strontium was also presented. The considerations outlined in the design of the two-color GMOT are largely transferable to other atom species with a strong and a narrow-line cooling transition and can

serve as a guideline. 2.5×10^5 ^{88}Sr atoms were trapped and cooled to a temperature of $< 5\,\mu$K. Atoms are thus sufficiently cold to be transferred to an optical lattice where a trap depth of $10\,\mu$K or more is typical. One can expect that the atom number can be greatly improved by loading from the vertical axis or with a higher flux of (slow) atoms.

The results obtained prove that GMOTs are compatible with multi-color magneto-optical trapping.

In the GMOT, a vacuum-limited lifetime was observed for high laser intensities and magnetic field gradients. Unlike in the Fresnel MOT, the lifetime was found to increase with increasing laser intensity. This was linked to the reduced trapping coefficient and trap depth due to a large anti-trapping contribution resulting from a less favorable angle between incident beam and secondary beams. This was likely also the underlying cause for no significant number of atoms being trapped with the deceleration beam turned off, i.e. only a small number of slow atoms, while atoms could be loaded directly from the thermal atom beam in the Fresnel MOT.

Confinement in the GMOT improves with increasing laser intensity and magnetic field gradient. Further, atoms were colder at high laser intensities than in the Fresnel MOT hinting that intensity fluctuations are less problematic here. In conclusion, it is suspected that significant intensity fluctuations in the Fresnel MOT result from the Fresnel structure. For low laser intensities, the temperature ratio of axial and radial temperature corresponds to theory for both the Fresnel MOT and the GMOT.

GMOTs present a monolithic chip-design and thus provide the highest level of miniaturization. However, a as we have seen, they require deviation from an ideal trapping geometry.

The work presented enables further miniaturization necessary for a transition of quantum sensors based on alkaline-earth-like atoms from the lab to field applications including space-borne set-ups.

As such, the changed trap dynamic in a narrow-line MOT in micro-gravity was also analyzed finding challenges in the form of a reduced number density and higher temperatures that, however, proved manageable.

7.2 OUTLOOK

Building on the research presented in this thesis, next steps include combination with a miniaturized atom source and vacuum chamber to take full advantage of the compact trapping geometry both the Fresnel MOT and in particular the GMOT provide. A micro-hotplate have for instance previously been demonstrated for ytterbium and a similar wafer-based atom source would be a good candidate [61]. Integration of the MOT coils on a chip has also been demonstrated for a rubidium experiment [20]. Further research and development thus provides the exciting perspective of a physics package with a volume of a few cm^3 for alkaline-earth-like atoms.

A new prototype of the Fresnel MOT is planned addressing some of the issues identified for an improved performance.

An open question that remains and lends itself for immediate further investigation is the search for a ^{87}Sr second stage MOT as this isotope is for instance primarily used in optical lattice clocks. Complications arising from the hyperfine structure for trapping in this geometry were outlined in Chapter 2.5 with simulations performed by the Maryland group indicating a ^{87}Sr second stage MOT is in principle possible [26].

An upgrade of the test set-up in the form of an aperture between the oven and the main chamber would allow for an increased oven temperature, improved vacuum pressure, and reduced background fluorescence. Consequently, a higher atom number and improved signal for the first stage ^{87}Sr MOT can be achieved enabling the search for a ^{87}Sr second stage MOT.

BIBLIOGRAPHY

[1] C. Adams and E. Riis. “Laser cooling and trapping of neutral atoms.” In: *Progress in Quantum Electronics* 21.1 (1997), pp. 1–79. ISSN: 0079-6727. DOI: https://doi.org/10.1016/S0079-6727(96)00006-7.

[2] G. Agrawal. “Line narrowing in a single-mode injection laser due to external optical feedback.” In: *IEEE Journal of Quantum Electronics* 20.5 (1984), pp. 468–471. DOI: 10.1109/JQE.1984.1072420.

[3] A. Ashkin. “Trapping of Atoms by Resonance Radiation Pressure.” In: *Phys. Rev. Lett.* 40 (1978), pp. 729–732. DOI: 10.1103/PhysRevLett.40.729.

[4] D. S. Barker, E. B. Norrgard, N. N. Klimov, J. A. Fedchak, J. Scherschligt, and S. Eckel. “Single-beam Zeeman slower and magneto-optical trap using a nanofabricated grating.” In: *Phys. Rev. Applied* 11.6 (2019), p. 064023. DOI: 10.1103/PhysRevApplied.11.064023.

[5] W. Bartosch. “The electronic and experimental setup of the MAIUS-2 and MAIUS-3 sounding rocket missions.” PhD thesis. QUEST Leibniz Forschungsschule, Universitaet Hannover, 2021. DOI: https://doi.org/10.15488/11345.

[6] B. Battelier, B. Barrett, L. Fouché, L. Chichet, L. Antoni-Micollier, H. Porte, F. Napolitano, J. Lautier, A. Landragin, and P. Bouyer. “Development of compact cold-atom sensors for inertial navigation.” In: *Quantum Optics*. Ed. by J. Stuhler and A. J. Shields. Vol. 9900. International Society for Optics and Photonics. SPIE, 2016, pp. 21 –37. DOI: 10.1117/12.2228351.

[7] D. Becker, K. Frye, C. Schubert, E. M. Rasel, and Beccal Collaboration. “BECCAL - Atom Optics with BECs on the ISS.” In: *APS Division of Atomic, Molecular and Optical Physics Meeting Abstracts*. Vol. 2018. APS Meeting Abstracts. May 2018, M01.145, p. M01.145.

[8] D. Becker et al. “Space-borne Bose-Einstein condensation for precision interferometry.” In: *Nature* 562 (2018), pp. 391–395. DOI: 10.1038/s41586-018-0605-1.

[9] S. Bize et al. “Cold atom clocks and applications.” In: *J. Phys. B: At. Mol. Phys.* 38 (2005), S449–S468. DOI: 10.1088/0953-4075/38/9/002.

[10] Q. Bodart, S. Merlet, N. Malossi, F. P. Dos Santos, P. Bouyer, and A. Landragin. "A cold atom pyramidal gravimeter with a single laser beam." In: *Appl. Phys. Lett.* 96.13 (2010), p. 134101. DOI: 10.1063/1.3373917.

[11] S. Bondza, T. Leopold, and C. Lisdat. "[DE] Atomfalle und Verfahren zum Kühlen oder Einfangen von Atomen." Pat. DE 102020102222B4. Bundesrepublik Deutschland, vertreten durch das Bundesministerium für Wirtschaft und Energie, dieses vertreten durch den Präsidenten der Physikalisch-Technischen Bundesanstalt, 38116 Braunschweig, DE. 2022.

[12] S. Bondza, C. Lisdat, S. Kroker, and T. Leopold. "Two-Color Grating Magneto-Optical Trap for Narrow-Line Laser Cooling." In: *Phys. Rev. Appl.* 17 (4 2022), p. 044002. DOI: 10.1103/PhysRevApplied.17.044002.

[13] K. Bongs et al. "Development of a strontium optical lattice clock for the SOC mission on the ISS." In: *C. R. Physique* 16 (2015). Special Issue: The measurement of time / La mesure du temps, pp. 553–564. DOI: 10.1016/j.crhy.2015.03.009.

[14] K. Bongs, M. Holynski, J. Vovrosh, P. Bouyer, G. Condon, E. Rasel, C. Schubert, W. Schleich, and A. Roura. "Taking atom interferometric quantum sensors from the labaratory to real-world applications." In: *Nat. Rev. Phys.* 1 (2019), pp. 731–739. DOI: https://doi.org/10.1038/s42254-019-0117-4.

[15] T. Bothwell, D. Kedar, E. Oelker, J. M. Robinson, S. L. Bromley, W. L. Tew, J. Ye, and C. J. Kennedy. "JILA SrI optical lattice clock with uncertainty of 2.0×10^{-18}." In: *Metrologia* 56.6 (2019), p. 065004. DOI: 10.1088/1681-7575/ab4089.

[16] W. Bowden, R. Hobson, I. R. Hill, A. Vianello, M. Schioppo, A. Silva, H. S. Margolis, P. E. G. Baird, and P. Gill. "A pyramid MOT with integrated optical cavities as a cold atom platform for an optical lattice clock." In: *Scient. Rep.* 9.10 (2019), p. 11704. DOI: https://doi.org/10.1038/s41598-019-48168-3.

[17] M. M. Boyd. "High Precision Spectroscopy of Strontium in an Optical Lattice: Towards a New Standard for Frequency and Time." PhD thesis. Graduate School of the University of Colorado, 2007.

[18] S. M. Brewer, J.-S. Chen, A. M. Hankin, E. R. Clements, C. W. Chou, D. J. Wineland, D. B. Hume, and D. R. Leibrandt. "$^{27}\mathrm{Al}^{+}$ quantum-logic clock with a systematic uncertainty below 10^{-18}." In: *Phys. Rev. Lett.* 123 (2019), p. 033201. DOI: 10.1103/PhysRevLett.123.033201.

[19] T. Chanelière, J.-L. Meunier, R. Kaiser, C. Miniatura, and D. Wilkowski. "Extra-heating mechanism in Doppler cooling experiments." In: *J. Opt. Soc. Am. B* 22 (2005), pp. 1819–1828. DOI: 10.1364/JOSAB.22.001819.

[20] L. Chen et al. "Planar-Integrated Magneto-Optical Trap." In: *Phys. Rev. Applied* 17 (3 2022), p. 034031. DOI: 10.1103/PhysRevApplied.17.034031.

[21] J. P. Cotter, J. P. McGilligan, P. F. Griffin, I. M. Rabey, K. Docherty, E. Riis, A. S. Arnold, and E. A. Hinds. "Design and fabrication of diffractive atom chips for laser cooling and trapping." In: *Appl. Phys. B* 122 (2016), p. 172. DOI: 10.1007/s00340-016-6415-y.

[22] C. L. Degen, F. Reinhard, and P. Cappellaro. "Quantum sensing." In: *Rev. Mod. Phys.* 89 (3 2017), p. 035002. DOI: 10.1103/RevModPhys.89.035002.

[23] *Developer of the Laser Calls It 'A Solution Seeking a Problem'; President of Korad Spends Spare Time Gardening and Fixing TV Sets*. New York Times, 1964.

[24] S. Eckel, D. S. Barker, J. A. Fedchak, N. N. Klimov, E. Norrgard, J. Scherschligt, C. Makrides, and E. Tiesinga. "Challenges to miniaturizing cold atom technology for deployable vacuum metrology." In: *Metrologia* 55.5 (2018), S182–S193. DOI: 10.1088/1681-7575/aadbe4.

[25] S. Eckel, D. S. Barker, E. B. Norrgard, and J. Scherschligt. "PyLCP: A Python package for computing laser cooling physics." In: *Computer Physics Communications* 270 (2022), p. 108166. ISSN: 0010-4655. DOI: https://doi.org/10.1016/j.cpc.2021.108166.

[26] P. K. Elgee. "Grating Magneto-optical Trap for Strontium." PhD thesis. University of Maryland, 2022.

[27] P. Elgee. *Private communication*. University of Maryland, 2022.

[28] R. Elvin, G. W. Hoth, M. Wright, B. Lewis, J. P. McGilligan, A. S. Arnold, P. F. Griffin, and E. Riis. "Cold-atom clock based on a diffractive optic." In: *Opt. Express* 27.26 (2019), pp. 38359–38366. DOI: 10.1364/OE.378632.

[29] S. Falke et al. "The ^{87}Sr optical frequency standard at PTB." In: *Metrologia* 48 (2011), pp. 399–407. DOI: doi:10.1088/0026-1394/48/5/022.

[30] B Fang et al. "Metrology with Atom Interferometry: Inertial Sensors from Laboratory to Field Applications." In: *Journal of Physics: Conference Series* 723 (2016), p. 012049. DOI: 10.1088/1742-6596/723/1/012049.

[31] R. Fasano. "A Transportable Ytterbium Optical Lattice Clock." PhD thesis. University of Colorado, 2021.

[32] R. Folman, P. Krüger, D. Cassettari, B. Hessmo, T. Maier, and J. Schmiedmayer. "Controlling Cold Atoms using Nanofabricated Surfaces: Atom Chips." In: *Phys. Rev. Lett.* 84 (20 2000), pp. 4749–4752. DOI: 10.1103/PhysRevLett.84.4749.

[33] C. Foot. *Atomic Physics*. Oxford Master Series in Physics. OUP Oxford, 2005. ISBN: 9780198506959.

[34] C. L. Garrido Alzar. "Compact chip-scale guided cold atom gyrometers for inertial navigation: Enabling technologies and design study." In: *AVS Quantum Science* 1.1 (2019), p. 014702. DOI: 10.1116/1.5120348.

[35] A. A. Geraci and A. Derevianko. "Sensitivity of Atom Interferometry to Ultralight Scalar Field Dark Matter." In: *Phys. Rev. Lett.* 117 (26 2016), p. 261301. DOI: 10.1103/PhysRevLett.117.261301.

[36] M. Glück, A. R. Kolovsky, H. J. Korsch, and N. Moiseyev. "Calculation of Wannier-Bloch and Wannier-Stark states." In: *Eur. Phys. J. D* 4 (1998), p. 239. DOI: 10.1007/s100530050205.

[37] P. W. Graham, J. M. Hogan, M. A. Kasevich, and S. Rajendran. "New Method for Gravitational Wave Detection with Atomic Sensors." In: *Phys. Rev. Lett.* 110 (2013), p. 171102. DOI: 10.1103/PhysRevLett.110.171102.

[38] J. Grotti. "A transportable optical lattice clock for metrology and geodesy." Phd Thesis. Hannover : Gottfried Wilhelm Leibniz Universität, 2018.

[39] J. Grotti et al. "Geodesy and metrology with a transportable optical clock." In: *Nature Physics* 14 (2018), pp. 437–441. DOI: 10.1038/s41567-017-0042-3.

[40] T. W. Hänsch and A. L. Schawlow. "Cooling of gases by laser radiation." In: *Opt. Commun.* 13 (1975), pp. 68–69. DOI: 10.1016/0030-4018(75)90159-5.

[41] L. Henriet, L. Beguin, A. Signoles, T. Lahaye, A. Browaeys, G.-O. Reymond, and C. Jurczak. "Quantum computing with neutral atoms." In: *Quantum* 4 (2020), p. 327.

[42] C. Henry. "Phase noise in semiconductor lasers." In: *J. Lightwave Technol.* 4.3 (1986), pp. 298–311. ISSN: 0733-8724. DOI: 10.1109/JLT.1986.1074721.

[43] L. Hu, N. Poli, L. Salvi, and G. M. Tino. "Atom Interferometry with the Sr Optical Clock Transition." In: *Phys. Rev. Lett.* 119 (26 2017), p. 263601. DOI: 10.1103/PhysRevLett.119.263601.

[44] M. Kasevich and S. Chu. “Measurement of the Gravitational Acceleration of an Atom with a Light-Pulse Atom Interferometer.” In: *Appl. Phys. B* 54 (1992), pp. 321–332. DOI: `https://doi.org/10.1007/BF00325375`.

[45] A. Kaufman, B. Lester, M. Foss-Feig, M. L. Wall, A. M. Rey, and C. Regal. “Entangling two transportable neutral atoms via local.” In: *Nature* (527 2015), pp. 208–211. DOI: `https://doi.org/10.1038/nature16073`.

[46] K. Kim, A. Aeppli, T. Bothwell, and J. Ye. *Evaluation of lattice light shift at mid 10^{-19} uncertainty for a shallow lattice Sr optical clock*. 2022. DOI: `10.48550/ARXIV.2210.16374`.

[47] M. Lachmann, H. Ahlers, D. Becker, A. Dinkelaker, J. Grosse, O. Hellmig, H. Muentinga, and E. Rasel. “Ultracold atom interferometry in space.” In: *Nature Communications* 12 (2021), p. 1317. DOI: `https://doi.org/10.1038/s41467-021-21628-z`.

[48] R. Le Targat. “Horloge à réseau optique au Strontium : une 2ème génération d’horloges à atomes froids.” PhD thesis. École nationale supérieure des télécommunications - ENST (13/07/2007), 2007.

[49] J. Lee et al. *A Compact Cold-Atom Interferometer with a High Data-Rate Grating Magneto-Optical Trap and a Photonic-Integrated-Circuit-Compatible Laser System*. 2021. DOI: `10.48550/ARXIV.2107.04792`.

[50] K. I. Lee, J. A. Kim, H. R. Noh, and W. Jhe. “Single-beam atom trap in a pyramidal and conical hollow mirror.” In: *Opt. Lett.* 21 (1996), pp. 1177–1179. DOI: `10.1364/OL.21.001177`.

[51] N. D. Lemke. “An Optical Lattice Clock with Spin-1/2 Atoms.” PhD thesis. University of Colorado at Boulder, 2012.

[52] P. Lemonde and P. Wolf. “Optical lattice clock with atoms confined in a shallow trap.” In: *Phys. Rev. A* 72 (2005), p. 033409. DOI: `10.1103/PhysRevA.72.033409`.

[53] P. D. Lett, W. D. Phillips, S. L. Rolston, C. E. Tanner, R. N. Watts, and C. I. Westbrook. “Optical Molasses.” In: *J. Opt. Soc. Am. B* 6 (1989), pp. 2084–2107. DOI: `10.1364/JOSAB.6.002084`.

[54] M. Lin, H. Denker, and J. Müller. “A comparison of fixed- and free-positioned point mass methods for regional gravity field modeling.” In: *Journal of Geodynamics* 125 (2019), pp. 32–47. ISSN: 0264-3707. DOI: `https://doi.org/10.1016/j.jog.2019.01.001`.

[55] Q. Lin, M. A. V. Camp, H. Zhang, B. Jelenković, and V. Vuletić. “Long-external-cavity distributed Bragg reflector laser with sub-kilohertz intrinsic linewidth.” In: *Opt. Lett.* 37.11 (2012), pp. 1989–1991. DOI: `10.1364/OL.37.001989`.

[56] T. H. Loftus, T. Ido, M. M. Boyd, A. D. Ludlow, and J. Ye. "Narrow line cooling and momentum-space crystals." In: *Phys. Rev. A* 70 (2004), p. 063413. DOI: `https://doi.org/10.1103/PhysRevA.70.063413`.

[57] F. Y. Loo, A. Brusch, S. Sauge, M. Allegrini, E. Arimondo, N. Andersen, and J. W. Thomsen. "Investigations of a two-level atom in a magneto-optical trap using magnesium." In: *J. Opt. B: Quantum Semiclass. Opt.* 681–85 (2004). DOI: `10.1088/1464-4266/6/1/013`.

[58] A. D. Ludlow. "The Strontium Optical Lattice Clock: Optical Spectroscopy with Sub-Hertz Accuracy." PhD thesis. University of Colorado, Boulder, 2008.

[59] A. D. Ludlow, M. M. Boyd, J. Ye, E. Peik, and P. O. Schmidt. "Optical atomic clocks." In: *Rev. Mod. Phys.* 87 (2 2015), pp. 637–701. DOI: `10.1103/RevModPhys.87.637`.

[60] T. H. Maiman. "Stimulated Optical Radiation in Ruby." In: *Nature* 187 (1960), pp. 493–494. DOI: `10.1038/187493a0Letter`.

[61] R. P. Manginell, M. W. Moorman, J. M. Anderson, G. R. Burns, K. E. Achyuthan, D. R. Wheeler, and P. D. D. Schwindt. "In situ dissolution or deposition of Ytterbium (Yb) metal in microhotplate wells for a miniaturized atomic clock." In: *Opt. Express* 20.22 (2012), pp. 24650–24663. DOI: `10.1364/OE.20.024650`.

[62] Y. Margalit, Z. Zhou, S. Machluf, D. Rohrlich, Y. Japha, and R. Folman. "A self-interfering clock as a "which path" witness." In: *Science* 349.6253 (2015), pp. 1205–1208. DOI: `10.1126/science.aac6498`.

[63] K. W. Martin, G. Phelps, N. D. Lemke, M. S. Bigelow, B. Stuhl, M. Wojcik, M. Holt, I. Coddington, M. W. Bishop, and J. H. Burke. "Compact Optical Atomic Clock Based on a Two-Photon Transition in Rubidium." In: *Phys. Rev. Applied* 9 (1 2018), p. 014019. DOI: `10.1103/PhysRevApplied.9.014019`.

[64] J. P. McGilligan, K. Gallacher, P. F. Griffin, D. J. Paul, A. S. Arnold, and E. Riis. "Invited Review: Micro-fabricated components for cold atom sensors." In: (2022). DOI: `10.48550/ARXIV.2208.00680`.

[65] J. P. McGilligan, P. F. Griffin, E. Riis, and A. S. Arnold. "Phase-space properties of magneto-optical traps utilising micro-fabricated gratings." In: *J. Opt. Soc. Am. B* 23.7 (2015), pp. 1271–1277. DOI: `0.1364/OE.23.008948`.

[66] J. P. McGilligan, P. F. Griffin, E. Riis, and A. S. Arnold. "Diffraction-grating characterization for cold-atom experiments." In: *J. Opt. Soc. Am. B* 33.6 (2016), pp. 1271–1277. DOI: `10.1364/JOSAB.33.001271`.

[67] J. P. McGilligan, P. F. Griffin, R. Elvin, S. J. Ingleby, E. Riis, and A. S. Arnold. "Grating chips for quantum technologies." In: *Scientific Reports* 7.7 (2017), p. 384. DOI: `10.1038/s41598-017-00254-0`.

[68] W. F. McGrew et al. "Atomic clock performance beyond the geodetic limit." In: *Nature* 564 (2018), pp. 87–90. DOI: `10.1038/s41586-018-0738-2`.

[69] W. F. McGrew et al. "Towards the optical second: verifying optical clocks at the SI limit." In: *Optica* 6.4 (2019), pp. 448–454. DOI: `10.1364/OPTICA.6.000448`.

[70] V. Menoret, P. Vermeulen, N. L. Moigne, S. Bonvalot, P. Bouyer, A. Landragin, and B. Desruelle. "Gravity measurements below 10^{-9} g with a transportable absolute quantum gravimeter." In: *Scientific Reports* 8 (2018), p. 104207. DOI: `10.1038/s41598-018-30608-1`.

[71] M. G. Moharam and T. K. Gaylord. "Rigorous coupled-wave analysis of grating diffraction— E-mode polarization and losses." In: *J. Opt. Soc. Am.* 73.4 (1983), pp. 451–455. DOI: `10.1364/JOSA.73.000451`.

[72] T. Mukaiyama, H. Katori, T. Ido, Y. Li, and M. Kuwata-Gonokami. "Recoil-Limited Laser Cooling of Sr Atoms near the Fermi Temperature." In: *Phys. Rev. Lett.* 90.11 (2003), p. 113002. DOI: `10.1103/PhysRevLett.90.113002`.

[73] S. B. Nagel, C. E. Simien, S. Laha, P. Gupta, V. S. Ashoka, and T. C. Killian. "Magnetic trapping of metastable $^3P_2$ atomic strontium." In: *Phys. Rev. A* 67.1 (2003), p. 011401. DOI: `10.1103/PhysRevA.67.011401`.

[74] T. L. Nicholson et al. "Systematic evaluation of an atomic clock at 2×10^{-18} total uncertainty." In: *Nature Commun.* 6 (2015), p. 6896. DOI: `10.1038/ncomms7896`.

[75] C. C. Nshii, M. Vangeleyn, J. P. Cotter, P. F. Griffin, E. A. Hinds, C. N. Ironside, P. See, A. G. Sinclair, E. Riis, and A. S. Arnold. "A surface-patterned chip as a strong source of ultracold atoms for quantum technologies." In: *Nature Nanotechnologies* 8 (2013), pp. 321–324. DOI: `10.1038/nnano.2013.47`.

[76] C. W. Oates, F. Bondu, R. W. Fox, and L. Hollberg. "A Diode-Laser Optical Frequency Standard Based On Laser-Cooled Ca Atoms: Sub-kilohertz Spectroscopy by Optical Shelving Detection." In: *Eur. Phys. J. D* 7 (1999), pp. 449–460. DOI: `10.1007/s100530050589`.

[77] C. F. Ockeloen, R. Schmied, M. F. Riedel, and P. Treutlein. "Quantum metrology with a scanning probe atom interferometer." In: *Phys. Rev. Lett.* 111 (2013), p. 143001. DOI: `10.1103/PhysRevLett.111.143001`.

[78] E. Oelker et al. “Demonstration of 4.8×10^{-17} stability at 1 s for two independent optical clocks.” In: *Nature Photonics* 13 (2019), pp. 714–719. DOI: 10.1038/s41566-019-0493-4.

[79] N. Ohmae et al. “Transportable Strontium Optical Lattice Clocks Operated Outside Laboratory at the Level of 10^{-18} Uncertainty.” In: *Adv. Quantum Technol.* 4.n/a (2021), p. 2100015. DOI: 10.1002/qute.202100015.

[80] S. Origlia et al. “Development of a strontium optical lattice clock for the SOC mission on the ISS.” In: *Proc. SPIE* 9900 (2016), pp. 990003–990003–12. DOI: 10.1117/12.2229473.

[81] S. Origlia. “A high-performance bosonic optical lattice clock.” PhD thesis. Faculty of Mathematics and Natural Sciences at the Heinrich-Heine-Universität Düsseldorf, 2018.

[82] A. Peters, K. Y. Chung, and S. Chu. “Measurement of gravitational acceleration by dropping atoms.” In: *Nature* 400 (1999), pp. 849–852. DOI: 10.1038/23655.

[83] C. J. Picken, R Legaie, K McDonnell, and J. D. Pritchard. “Entanglement of neutral-atom qubits with long ground-Rydberg coherence times.” In: *Quantum Science and Technology* 4.1 (2018), p. 015011. DOI: 10.1088/2058-9565/aaf019.

[84] N. Poli, M. Schioppo, S. Vogt, S. Falke, U. Sterr, C. Lisdat, and G. M. Tino. “A transportable strontium optical lattice clock.” In: *Appl. Phys. B* 117 (2014), pp. 1107–1116. DOI: 10.1007/s00340-014-5932-9.

[85] S Pollock, J. P. Cotter, A Laliotis, F Ramirez-Martinez, and E. A. Hinds. “Characteristics of integrated magneto-optical traps for atom chips.” In: *New Journal of Physics* 13.4 (2011), p. 043029. DOI: 10.1088/1367-2630/13/4/043029.

[86] E. L. Raab, M. Prentiss, A. Cable, S. Chu, and D. E. Pritchard. “Trapping of Neutral Sodium Atoms with Radiation Pressure.” In: *Phys. Rev. Lett.* 59 (1987), pp. 2631–2634. DOI: 10.1103/PhysRevLett.59.2631.

[87] S. Ravenhall, B. Yuen, and C. Foot. “High-flux, adjustable, compact cold-atom source.” In: *Opt. Express* 29.14 (2021), pp. 21143–21159. DOI: 10.1364/OE.423662.

[88] J. Reichel, W. Hänsel, and T. W. Hänsch. “Atomic Micromanipulation with Magnetic Surface Traps.” In: *Phys. Rev. Lett.* 83 (17 1999), pp. 3398–3401. DOI: 10.1103/PhysRevLett.83.3398.

[89] J. Ren, H. Liu, X. Lu, and H. Chang. “Analysis of Narrow-Line Laser Cooling and Trapping of Sr Atoms in Microgravity Environments.” In: *Applied Sciences* 10.14 (2020). ISSN: 2076-3417. DOI: 10.3390/app10144928.

[90] F. Riehle. “Towards a redefinition of the second based on optical atomic clocks.” In: *C. R. Physique* 16.5 (2015). Special issue: The measurement of time / La mesure du temps, pp. 506–515. DOI: `10.1016/j.crhy.2015.03.012`.

[91] G. Rosenblatt, B. Simkhovich, G. Bartal, and M. Orenstein. “Nonmodal Plasmonics: Controlling the Forced Optical Response of Nanostructures.” In: *Phys. Rev. X* 10 (1 2020), p. 011071. DOI: `10.1103/PhysRevX.10.011071`.

[92] G. Rosi, G. D’Amico, L. Cacciapuoti, F. Sorrentino, M. Prevedelli, M. Zych, C. Brukner, and G. Tino. “Quantum test of the equivalence principle for atoms in coherent superposition of internal energy states.” In: *Nature Commun.* 8 (2017), p. 15529. DOI: `10.1038/ncomms15529`.

[93] J. A. Rushton, M. Aldous, and M. D. Himsworth. “Contributed Review: The feasibility of a fully miniaturized magneto-optical trap for portable ultracold quantum technology.” In: *Rev. Sci. Instrum.* 85.12 (2014), p. 121501. DOI: `10.1063/1.4904066`.

[94] M. Saffman. “Quantum computing with atomic qubits and Rydberg interactions: progress and challenges.” In: *Journal of Physics B: Atomic, Molecular and Optical Physics* 49.20 (2016), p. 202001. DOI: `10.1088/0953-4075/49/20/202001`.

[95] R. Santra, K. V. Christ, and C. H. Greene. “Properties of metastable alkaline-earth-metal atoms calculated using an accurate effective core potential.” In: *Phys. Rev. A* 69 (2004), p. 042510. DOI: `10.1103/PhysRevA.69.042510`.

[96] J. Scherschligt et al. “Review Article: Quantum-based vacuum metrology at the National Institute of Standards and Technology.” In: *Journal of Vacuum Science & Technology A* 36.4 (2018), p. 040801. DOI: `10.1116/1.5033568`.

[97] M. Schioppo, N. Poli, M. Prevedelli, S. Falke, C. Lisdat, U. Sterr, and G. M. Tino. “A compact and efficient strontium oven for laser-cooling experiments.” In: *Rev. Sci. Instrum.* 83.10 (2012), p. 103101. DOI: `10.1063/1.4756936`.

[98] M. Schioppo et al. “Ultra-stable optical clock with two cold-atom ensembles.” In: *Nature Photonics* 11 (2017), pp. 48–52. DOI: `10.1038/nphoton.2016.231`.

[99] R. Schwarz, S. Dörscher, A. Al-Masoudi, E. Benkler, T. Legero, U. Sterr, S. Weyers, J. Rahm, B. Lipphardt, and C. Lisdat. “Long term measurement of the ^{87}Sr clock frequency at the limit of primary Cs clocks.” In: *Phys. Rev. Research* 2 (3 2020), p. 033242. DOI: `10.1103/PhysRevResearch.2.033242`.

[100] A. Sitaram, P. K. Elgee, G. K. Campbell, N. N. Klimov, S. Eckel, and D. S. Barker. “Confinement of an alkaline-earth element in a grating magneto-optical trap.” In: *Review of Scientific Instruments* 91.10 (2020), p. 103202. DOI: `10.1063/5.0019551`.

[101] S. Stellmer. “Degenerate quantum gases of strontium.” PhD thesis. University of Innsbruck, 2013.

[102] A. V. Taichenachev, V. I. Yudin, C. W. Oates, C. W. Hoyt, Z. W. Barber, and L. Hollberg. “Magnetic Field-Induced Spectroscopy of Forbidden Optical Transitions with Application to Lattice-Based Optical Atomic Clocks.” In: *Phys. Rev. Lett.* 96 (2006), p. 083001. DOI: `10.1103/PhysRevLett.96.083001`.

[103] M. Takamoto, Y. Tanaka, and H. Katori. “A perspective on the future of transportable optical lattice clocks.” In: *Applied Physics Letters* 120.14 (2022), p. 140502. DOI: `10.1063/5.0087894`.

[104] T. Takano, M. Takamoto, I. Ushijima, N. Ohmae, T. Akatsuka, A. Yamaguchi, Y. Kuroishi, H. Munekane, B. Miyahara, and H. Katori. “Geopotential measurements with synchronously linked optical lattice clocks.” In: *Nature Photonics* 10 (2016), pp. 662–666. DOI: `10.1038/nphoton.2016.159`.

[105] G. M. Tino. “Testing gravity with cold atom interferometry: results and prospects.” In: *Quantum Science and Technology* 6.2 (2021), p. 024014. DOI: `10.1088/2058-9565/abd83e`.

[106] R. W. Tkach and A. R. Chraplyvy. “Regimes of feedback effects in 1.5-µm distributed feedback lasers.” In: *Journal of Lightwave Technology* 4 (Jan. 1986), p. 1655. DOI: `10.1109/JLT.1986.1074666`.

[107] M. Trupke et al. “Pyramidal micromirrors for microsystems and atom chips.” In: *Applied Physics Letters* 88.7 (2006), p. 071116. DOI: `10.1063/1.2172412`.

[108] M. Vangeleyn. “Atom trapping in non-trivial geometries for micro-fabrication applications.” PhD thesis. University of Strathclyde, 2011.

[109] M. Vangeleyn, P. F. Griffin, E. Riis, and A. S. Arnold. “Single-laser, one beam, tetrahedral magneto-optical trap.” In: *Opt. Express* 17.16 (2009), pp. 13601–13608. DOI: `10.1364/OE.17.013601`.

[110] M. Vangeleyn, P. F. Griffin, E. Riis, and A. S. Arnold. “Laser cooling with a single laser beam and a planar diffractor.” In: *Opt. Lett.* 35.20 (2010), pp. 3453–3455. DOI: `10.1364/OL.35.003453`.

[111] M. Vengalattore, J. M. Higbie, S. R. Leslie, J. Guzman, L. E. Sadler, and D. M. Stamper-Kurn. “High-Resolution Magnetometry with a Spinor Bose-Einstein Condensate.” In: *Phys. Rev. Lett.* 98 (2007), p. 200801. DOI: `10.1103/PhysRevLett.98.200801`.

[112] S. Wildermuth, P. Krüger, C. Becker, M. Brajdic, S. Haupt, A. Kasper, R. Folman, and J. Schmiedmayer. “Optimized magneto-optical trap for experiments with ultracold atoms near surfaces.” In: *Phys. Rev. A* 69 (3 2004), p. 030901. DOI: `10.1103/PhysRevA.69.030901`.

[113] S. Wildermuth, S. Hofferberth, I. Lesanovsky, E. Haller, L. M. Andersson, S. Groth, I. Bar-Joseph, P. Krüger, and J. Schmiedmayer. “Bose-Einstein condensates: Microscopic magnetic-field imaging.” In: *Nature* 435 (2005), p. 440.

[114] S. R. Wilkinson, C. F. Bharucha, K. W. Madison, Q. Niu, and M. G. Raizen. “Observation of Atomic Wannier-Stark Ladders in an Accelerating Optical Potential.” In: *Phys. Rev. Lett.* 76 (1996), pp. 4512–4515. DOI: `10.1103/PhysRevLett.76.4512`.

[115] X. Xu, T. H. Loftus, J. W. Dunn, C. H. Greene, J. L. Hall, A. Gallagher, and J. Ye. “Single-Stage Sub-Doppler Cooling of Alkaline Earth Atoms.” In: *Phys. Rev. Lett.* 90.19, 193002 (2003), p. 193002. DOI: `https://doi.org/10.1103/PhysRevLett.90.193002`.

[116] X. Xu, T. H. Loftus, J. L. Hall, A. Gallagher, and J. Ye. “Cooling and trapping of atomic strontium.” In: *J. Opt. Soc. Am. B* 20 (2003), pp. 968–976. DOI: `10.1364/JOSAB.20.000968`.

[117] X. Xu, T. Loftus, M. J. Smith, J. L. Hall, A. Gallagher, and J. Ye. “Dynamics in a two-level atom magneto-optical trap.” In: *Phys. Rev. A* 66 (2002), 011401(R)–1–4. DOI: `https://doi.org/10.1103/PhysRevA.66.011401`.

[118] S. Yoon, Y. Choi, S. Park, W. Ji, J.-H. Lee, and K. An. “Characteristics of single-atom trapping in a magneto-optical trap with a high magnetic-field gradient.” In: *Journal of Physics: Conference Series* 80 (2007), p. 012046. DOI: `10.1088/1742-6596/80/1/012046`.

[119] N. Yu and M. Tinto. “Gravitational wave detection with single-laser atom interferometers.” In: *Gen. Relativ. Gravit.* 43 (2011), p. 1943. DOI: `https://doi.org/10.1007/s10714-010-1055-8`.

CURRICULUM VITAE

ACADEMIC EDUCATION

Master of Science (Physics, Photonics) *September 2017 - June 2019*

Lund University

Bachelor of Science (Physics) *October 2013 - August 2017*

University of Freiburg

Exchange and research stays at the University of New South Wales, Sydney, Australia in 2015 and 2017

Allgemeine Hochschulreife (Abitur) *2005 - 2013*

Helmholtz-Gymnasium Heidelberg

RESEARCH

PhD Candidate *since August 2019*

Physikalisch-Technische Bundesanstalt/Leibniz University Hannover

Working Group 4.32, Optical Lattice Clocks

LIST OF PUBLICATIONS

PUBLICATIONS

2023 Bondza, Saskia, Leopold, Tobias, Schwarz, Roman, and Lisdat, Christian (2023). "An achromatic, planar Fresnel MOT". In: in preparation.

2022 Bondza, Saskia, Lisdat, Christian, Kroker, Stefanie, and Leopold, Tobias (2022). "Two-Color Grating Magneto-Optical Trap for Narrow-Line Laser Cooling". In: Phys. Rev. Appl. 17, p. 044002. doi: 10.1103/PhysRevApplied.17.044002.

2020 Bondza, Saskia, Bengtsson, Alexander, Horvath, Sebastian P., Walther, Andreas, Kröll, Stefan, and Rippe, Lars (2020). "A simple experimental method for measuring the thermal sensitivity of single-mode fibers". In: Review of Scientific Instruments 91.10, p. 105114. doi: 10.1063/5.0020913.

PATENTS

2022 Bondza, Saskia, Leopold, Tobias, and Lisdat, Christian (July 2022). "[DE] Atomfalle und Verfahren zum Kühlen oder Einfangen von Atomen". DE102020102222B4. Bun- desrepublik Deutschland, vertreten durch das Bundesmin- isterium für Wirtschaft und Energie, dieses vertreten durch den Präsidenten der Physikalisch-Technischen Bundesanstalt, 38116 Braunschweig, DE.

COLOPHON

This document was typeset using the typographical look-and-feel `classicthesis` developed by André Miede. The style was inspired by Robert Bringhurst's seminal book on typography "*The Elements of Typographic Style*". `classicthesis` is available for both LaTeX and LyX:

`https://bitbucket.org/amiede/classicthesis/`